

## The CLEO II detector

Y. Kubota <sup>a</sup>, J.K. Nelson <sup>a</sup>, D. Peticone <sup>a</sup>, R. Poling <sup>a</sup>, S. Schrenk <sup>a</sup>, M.S. Alam <sup>b</sup>, Z.H. Bian <sup>b</sup>,  
D. Chen <sup>b</sup>, I.J. Kim <sup>b</sup>, W.C. Li <sup>b</sup>, X.C. Lou <sup>b</sup>, B. Nemati <sup>b</sup>, C.R. Sun <sup>b</sup>, P.-N. Wang <sup>b</sup>,  
M.M. Zoeller <sup>b</sup>, G. Crawford <sup>c</sup>, R. Fulton <sup>c</sup>, K.K. Gan <sup>c</sup>, T. Jensen <sup>c</sup>, H. Kagan <sup>c</sup>,  
R. Kass <sup>c</sup>, R. Malchow <sup>c</sup>, F. Morrow <sup>c</sup>, M.K. Sung <sup>c</sup>, J. Whitmore <sup>c</sup>, P. Wilson <sup>c</sup>,  
F. Butler <sup>d</sup>, X. Fu <sup>d</sup>, G. Kalbfleisch <sup>d</sup>, M. Lambrecht <sup>d</sup>, P. Skubic <sup>d</sup>, J. Snow <sup>d</sup>,  
P.-L. Wang <sup>d</sup>, D. Bortoletto <sup>e</sup>, D.N. Brown <sup>e</sup>, W.Y. Chen <sup>e</sup>, J. Dominick <sup>e</sup>, R.L. McIlwain <sup>e</sup>,  
D.H. Miller <sup>e</sup>, M. Modesitt <sup>e</sup>, E.I. Shibata <sup>e</sup>, S.F. Schaffner <sup>e</sup>, I.P.J. Shipsey <sup>e</sup>, W.M. Yao <sup>e</sup>,  
M. Battle <sup>f</sup>, H. Kroha <sup>f</sup>, K. Sparks <sup>f</sup>, E.H. Thorndike <sup>f</sup>, C.-H. Wang <sup>f</sup>, R. Stroynowski <sup>g</sup>,  
M. Artuso <sup>h</sup>, M. Goldberg <sup>h</sup>, T. Haupt <sup>h</sup>, R. Holmes <sup>h</sup>, N. Horwitz <sup>h</sup>, A. Jawahery <sup>h</sup>,  
P. Lubrano <sup>h</sup>, G.C. Moneti <sup>h</sup>, Y. Rozen <sup>h</sup>, P. Rubin <sup>h</sup>, V. Sharma <sup>h</sup>, T. Skwarnicki <sup>h</sup>, S. Stone <sup>h</sup>,  
M. Thulasidas <sup>h</sup>, G. Zhu <sup>h</sup>, S.E. Csorna <sup>i</sup>, V. Jain <sup>i</sup>, T. Letson <sup>i</sup>, D.S. Akerib <sup>j</sup>, B. Barish <sup>j</sup>,  
M. Chadha <sup>j</sup>, D.F. Cowen <sup>j</sup>, G. Eigen <sup>j</sup>, J.S. Miller <sup>j</sup>, J. Urheim <sup>j</sup>, A.J. Weinstein <sup>j</sup>,  
R.J. Morrison <sup>k</sup>, H. Nelson <sup>k</sup>, J. Richman <sup>k</sup>, H. Tajima <sup>k</sup>, D. Schmidt <sup>k</sup>, M. Witherell <sup>k</sup>,  
A. Bean <sup>l</sup>, I. Brock <sup>l</sup>, M. Procaro <sup>l</sup>, M. Daoudi <sup>m</sup>, W.T. Ford <sup>m</sup>, D.R. Johnson <sup>m</sup>,  
K. Lingel <sup>m</sup>, M. Lohner <sup>m</sup>, P. Rankin <sup>m</sup>, J.G. Smith <sup>m</sup>, J. Alexander <sup>n</sup>, C. Bebek <sup>n</sup>,  
K. Berkelman <sup>n</sup>, D. Besson <sup>n</sup>, E. Blucher <sup>n</sup>, T.E. Browder <sup>n</sup>, D.G. Cassel <sup>n</sup>, E. Cheu <sup>n</sup>,  
D.M. Coffman <sup>n</sup>, R. DeSalvo <sup>n</sup>, P.S. Drell <sup>n</sup>, R. Ehrlich <sup>n</sup>, R.S. Galik <sup>n</sup>,  
M. Garcia-Sciveres <sup>n</sup>, B. Geiser <sup>n</sup>, M.G.D. Gilchriese <sup>n</sup>, B. Gittelman <sup>n</sup>, S.W. Gray <sup>n</sup>,  
D.L. Hartill <sup>n</sup>, B.K. Heltsley <sup>n</sup>, K. Honscheid <sup>n</sup>, C. Jones <sup>n</sup>, J. Kandaswamy <sup>n</sup>, N. Katayama <sup>n</sup>,  
P.C. Kim <sup>n</sup>, R. Kowalewski <sup>n</sup>, D.L. Kreinick <sup>n</sup>, G.S. Ludwig <sup>n</sup>, J. Masui <sup>n</sup>, J. Mevissen <sup>n</sup>,  
N.B. Mistry <sup>n</sup>, J. Mueller <sup>n</sup>, R. Namjoshi <sup>n</sup>, S. Nandi <sup>n</sup>, C.R. Ng <sup>n</sup>, E. Nordberg <sup>n</sup>,  
C. O'Grady <sup>n</sup>, J.R. Patterson <sup>n</sup>, D. Peterson <sup>n</sup>, M. Pisharody <sup>n</sup>, D. Riley <sup>n</sup>, M. Sapper <sup>n</sup>,  
M. Selen <sup>n</sup>, H. Worden <sup>n</sup>, M. Worriss <sup>n</sup>, F. Würthwein <sup>n</sup>, P. Avery <sup>o</sup>, A. Freyberger <sup>o</sup>,  
J. Rodriguez <sup>o</sup>, J. Yelton <sup>o</sup>, T. Bowcock <sup>p</sup>, R. Giles <sup>p</sup>, S. Henderson <sup>p</sup>, K. Kinoshita <sup>p</sup>,  
F. Pipkin <sup>p</sup>, M. Saulnier <sup>p</sup>, R. Wilson <sup>p</sup>, J. Wolinski <sup>p</sup>, D. Xiao <sup>p</sup>, H. Yamamoto <sup>p</sup>,  
A.J. Sadoff <sup>q</sup>, R. Ammar <sup>r</sup>, P. Baringer <sup>r</sup>, D. Coppage <sup>r</sup>, R. Davis <sup>r</sup>, P. Haas <sup>r</sup>, M. Kelly <sup>r</sup>,  
N. Kwak <sup>r</sup>, H. Lam <sup>r</sup> and S. Ro <sup>r</sup>

<sup>a</sup> University of Minnesota, Minneapolis, MN 55455, USA

<sup>b</sup> State University of New York at Albany, Albany, NY 12222, USA

<sup>c</sup> Ohio State University, Columbus, OH 43210, USA

<sup>d</sup> University of Oklahoma, Norman, OK 73019, USA

<sup>e</sup> Purdue University, West Lafayette, IN 47907, USA

<sup>f</sup> University of Rochester, Rochester, NY 14627, USA

<sup>g</sup> Southern Methodist University, Dallas, TX 75275, USA

<sup>h</sup> Syracuse University, Syracuse, NY 13244, USA

<sup>i</sup> Vanderbilt University, Nashville, TN 37235, USA

<sup>j</sup> California Institute of Technology, Pasadena, CA 91125, USA

<sup>k</sup> University of California at Santa Barbara, Santa Barbara, CA 93106, USA

<sup>l</sup> Carnegie-Mellon University, Pittsburgh, PA 15213, USA

<sup>m</sup> University of Colorado, Boulder, CO 80309-0390, USA

<sup>n</sup> Cornell University, Ithaca, NY 14853, USA

<sup>o</sup> University of Florida, Gainesville, FL 32611, USA

<sup>p</sup> Harvard University, Cambridge, MA 02138, USA

<sup>q</sup> Ithaca College, Ithaca, NY 14850, USA

<sup>r</sup> University of Kansas, Lawrence, KS 66045, USA

Received 16 January 1992

The new detector for data recording by the CLEO collaboration at the Cornell Electron Storage Ring is described. This detector has been designed to optimize studying  $e^+e^-$  annihilation into hadronic matter at a total energy of 10 GeV. It consists of high precision charged particle tracking chambers and an electromagnetic calorimeter together with systems for particle identification. The design of the detector and its performance over the first year and a half of operation are presented.

## 1. Introduction

The Cornell Electron Storage Ring (CESR) was constructed in 1977–79, and started operating in 1979. The storage ring provides electron–positron collisions in the energy range of the  $\Upsilon$  states, 9 to 11 GeV. The physics program is concentrated on the decay of the  $\Upsilon$  resonances and heavy quark flavoured mesons [1]. In September 1979, two experimental groups, CLEO and CUSB, began recording and analyzing data. The first several years of study led to the discovery of the  $\Upsilon(3S)$  and  $\Upsilon(4S)$  resonances [2] and the reconstruction of B mesons [3] coming from  $\Upsilon(4S)$  decay. The overall data indicated that these new particle states are compatible with the Standard Model but not describable by the other proposed symmetry models [4] of that time. By 1983 it was realized that accurate tabulation of the properties of B meson decay would provide important parameters for the Standard Model and allow evalua-

tion of the ability of the Standard Model to describe the weak decay of heavy quark matter. However, to carry out this program we needed a major upgrade in the CLEO detector. The original CLEO detector [5], designed before the discovery of the  $\Upsilon$  consisted of a 17 layer drift chamber in a 0.4 T solenoid magnetic field of 1 m radius. In 1981, the magnet coil was replaced with a superconducting coil and the field raised to 1.0 T [6].

At that time the outer detector, which provided particle identification and magnetic flux return, was finalized to eight identical octants. Each octant contained a layer of drift chamber to measure the track Z coordinate, a 20 layer proportional chamber to measure specific ionization, time-of-flight counters, a lead layered proportional chamber electromagnetic calorimeter, and a set of drift chambers outside of the magnet iron for muon identification. We began data recording with this upgraded detector in March 1982.

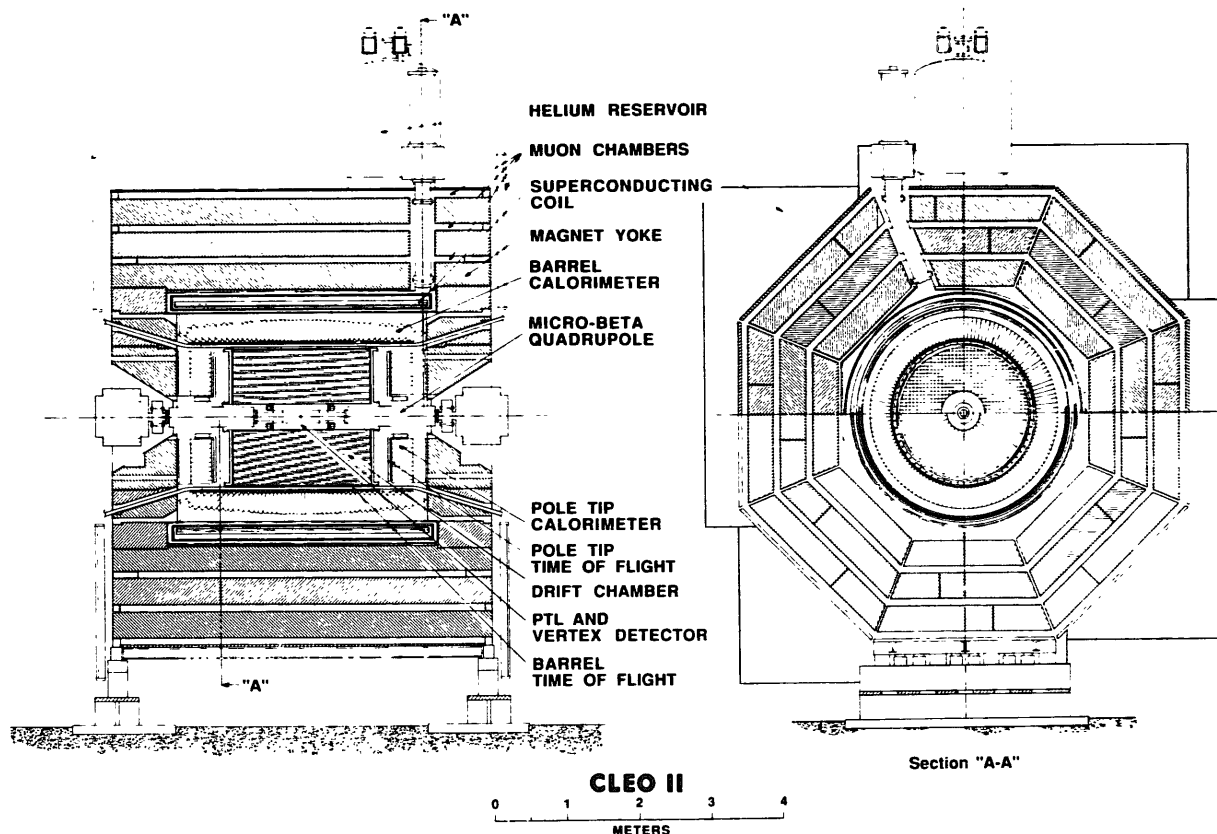


Fig. 1. The CLEO II detector (side view and end view).

By 1983, it was clear we needed a better drift chamber and photon detector, and that the particle identification system had to be located inside of the coil.

A program was initiated to build a new vertex detector and drift chamber. The new vertex chamber (VD), a 10 layer hexagonal-cell drift chamber was completed and installed in the existing detector during summer 1984. While we continued data recording with the new vertex detector, a 51 layer drift chamber was built. It was installed in the CLEO magnet [7] to replace the original drift chamber in the summer of 1986. In 1984, we requested funds to rebuild the rest of the CLEO detector [8], which we named CLEO II. A diagram illustrating the CLEO II detector is shown in fig. 1. The major new elements are a Superconducting Magnet with a coil radius of 1.5 m and 1.5 T maximum field, a time-of-flight system which covers 95% of the solid angle, a CsI electromagnetic calorimeter, and a muon identification system. The CLEO II detector was installed in the CESR south interaction region in 1988–1989, and data recording began in October 1989.

In this paper the design properties of the CLEO II detector are described together with the current status of calibration and resolution of the various subsystems. An expanded view of the detector inside of the magnet coil is shown in fig. 2. The magnetic field is parallel to the beam line and extends 1.75 m from the centre of the interaction region to the magnet pole. We define

the  $Z$  axis to point along the direction of the positron beam; the  $X$  axis points horizontal (south), and the  $Y$  axis points upward. We have been recording data with the magnetic field at 1.5 T, pointing in the  $-Z$  direction. The electron and positron bunches at the interaction region are typically (FWHM) 1.1 mm wide, 0.1 mm high, and have a length of 4.2 cm. Each bunch passes through the interaction region 390 000 times per second. The machine currently operates with seven bunches of electrons and seven bunches of positrons. The electrons and positrons have separated orbits that pass through each other at the centre of the interaction region.

When an  $e^+e^-$  annihilation occurs, most final state particles created in the collision pass through the beam pipe and enter the detector. Particles moving at an angle between  $25^\circ$  and  $155^\circ$  with respect to the beam pass through a 3.5 cm radius beryllium beam pipe, 0.5 mm thick, and the precision tracking layer (PTL) which extends from the beam pipe to the vertex detector. The PTL is a cell–strawtube–drift-chamber, which was designed and built in the Spring of 1989, after a decision was made to reduce the CESR beam pipe radius at the interaction region from 5.5 to 3.5 cm. The vertex detector (VD), which operated in the CLEO I detector, covers the radial region from 7.5 to 17.5 cm. Beyond the VD is the 51 layer drift chamber (DR). To measure the momentum vector of charged particles,

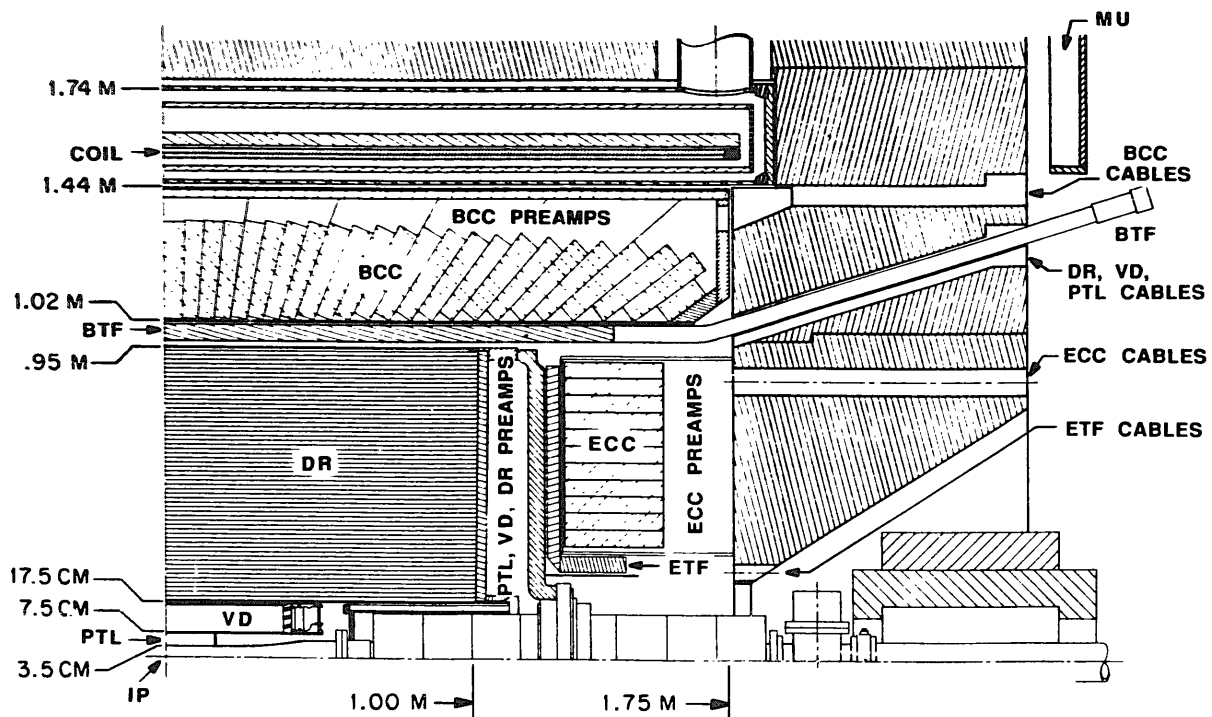


Fig. 2. Schematic Drawing of one quadrant of the CLEO II detector. The following acronyms are used – DR, VD, PTL: The outer, intermediate and inner drift chambers. TF, CC, MU: The time-of-flight counters, crystal calorimeter and muon identification system. Prefixes: B = barrel, E = endcap.

the data from all three chambers are combined. Charged particles created with a transverse momentum greater than 225 MeV/c and a polar angle greater than  $45^\circ$  will reach the outer radius of the DR and pass through the barrel time-of-flight counters (BTF) and the barrel crystal calorimeter (BCC). These tracks are the best measured in the CLEO II detector. Charged tracks with polar angles between  $25^\circ$  and  $45^\circ$  are measured in the PTL, the VD, and part of the DR. The tracking resolution in this small polar angle region is significantly reduced, but is adequate for many purposes. The endcap time-of-flight counters (ETF) and endcap crystal calorimeter (ECC) cover the polar angle range from  $15^\circ$  to  $37^\circ$  and are mounted on the magnet pole. The barrel and endcap time-of-flight and

calorimeter systems overlap in polar angle range between  $35^\circ$  and  $37^\circ$ . The barrel time-of-flight counters and the calorimeter cover the range from the  $35^\circ$  to  $145^\circ$ . However, there is a reduction in their resolutions in the region  $35^\circ$ – $45^\circ$  (and  $135^\circ$ – $145^\circ$ ) arising from the materials associated with the support structures for the drift chamber and beam pipe, and the electrical cables. The barrel calorimeter fills the radial region from 1.02 to 1.44 m. It weighs approximately 30 tons and is mounted on the superconducting coil cryostat, which extends radially to 1.74 m.

The magnet return yoke and muon identification system (MU) are shown in fig. 1. The iron of the return yoke is octagonally divided. The first two 36 cm thick layers are the main elements for the magnetic field flux

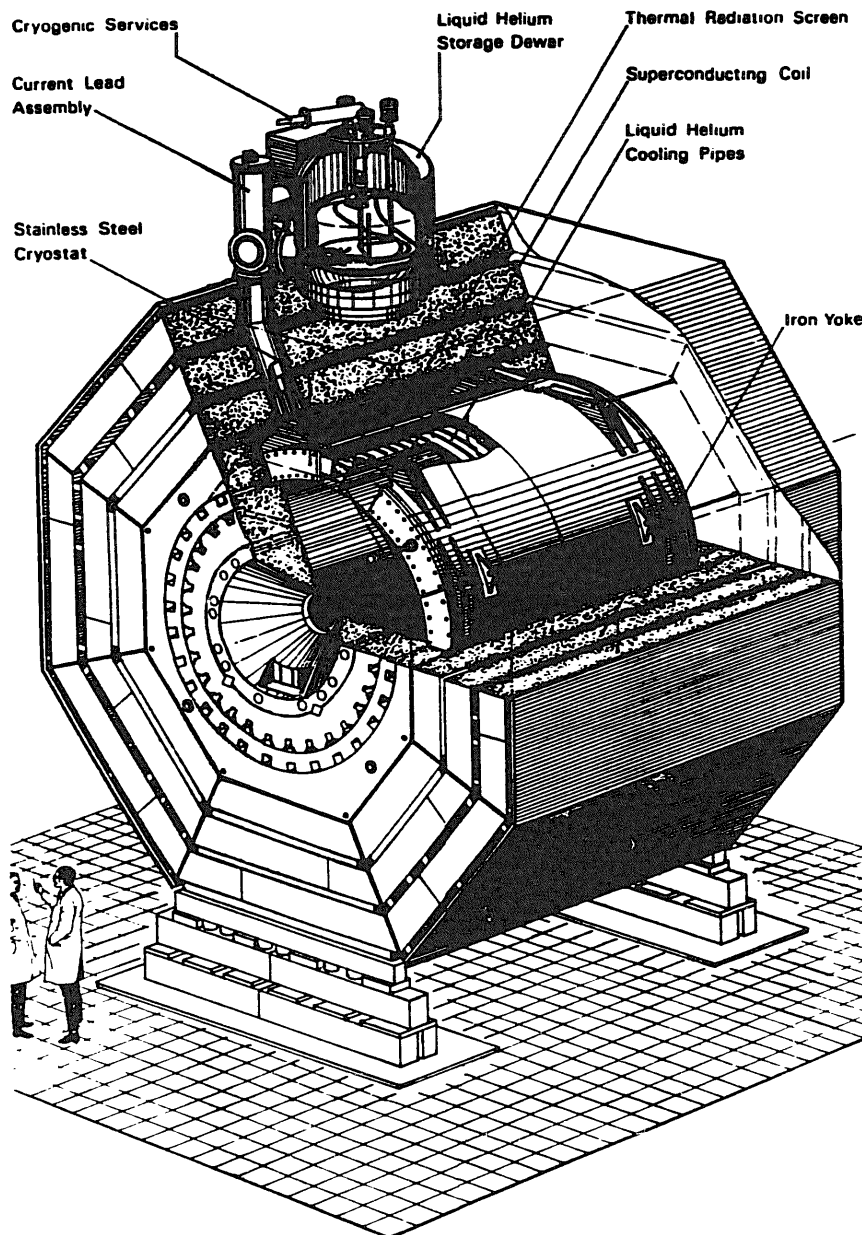


Fig. 3. Arrangement of the CLEO II superconducting coil and steel magnet yoke.

return. The third layer is primarily for the muon identification system. Outside of each return yoke layer there is a set of gas wire chambers used for muon identification. These three sets of chambers cover the angular range  $45^\circ$ – $135^\circ$ . There is also one set of muon chambers outside each endcap which covers the polar angle range  $30^\circ$ – $48^\circ$ . Beyond the outermost muon chambers, there is a 2.5 cm thick piece of iron which is mounted to mechanically protect the chambers and shield them from radiation.

## 2. The CLEO II magnet

### 2.1. Design goals and development

The primary requirements of the CLEO II magnet are a uniform, high magnetic field strength and sufficient size to contain the calorimeter inside the coil [8]. Both a new superconducting coil and new yoke were required. The design of the new magnet is intended to keep the good features of the smaller CLEO I solenoid [6] such as low cryogenic load, while eliminating its weaknesses such as poor insulating vacuum, sensitivity to refrigerator performance, susceptibility to utility outages and dependence on active quench protection. The design goals are thus: increased stability, low cryogenic load, passive cooling and passive protection.

Oxford Instruments, Ltd. and G.A. Technologies, Inc. each performed design studies with these requirements in mind in late 1984. G.A. Technologies explored a modern pool-boiling design using copper stabilized superconductor and Oxford Instruments used the novel thermosyphon approach to the cooling of aluminum stabilized superconductor. Both designs met our criteria. These design studies were sent to a number of potential coil fabricators who were asked to submit proposals based either on one of these studies or on their own scheme. Oxford Instruments was selected on the basis of cost and design features and was awarded the contract in June, 1985. Construction was completed in July, 1987 at which time the coil was successfully tested at 40% of full current at Oxford,

without its steel yoke. The coil arrived at Cornell in October, 1987 and passed full current acceptance tests in the steel yoke in February, 1988. Dismantling of the CLEO I detector began in the summer of 1988 and assembly of CLEO II was completed in the fall of 1989.

The design of the steel yoke for CLEO II underwent several revisions as the requirements were clarified. The CLEO I yoke was not adaptable as a unit to the CLEO II requirements and the steel pieces could not easily be reworked. The availability of the old steel yoke of the Space Radiation Effects Laboratory synchro-cyclotron that was stored at Brookhaven National Laboratory, and a use at Brookhaven for our old CLEO I yoke and coil led to a natural trade. This steel was machined by Dominion Bridge-Sulzer Inc. into the outer return yoke slabs. New, forged steel was purchased and machined into the pole pieces. Our schedule allowed interaction with Oxford Instruments on those design features of the yoke that interfaced with the superconducting coil. Fig. 3 shows a general view of the magnet and table 1 provides its general parameters.

### 2.2. Magnet yoke and poles

The availability of the steel from Brookhaven National Laboratory determined the return yoke thickness to be 36 cm and led to octagonal symmetry as the most convenient geometry to incorporate these pieces. There are three layers of steel, separated by gaps of 9 cm for muon detectors, with the inner two layers providing almost all the magnetic flux return. A 2.5 cm thick sheet of steel outside the outermost muon chambers is added for protection and radiation shielding. The cut in the steel yoke for access to the superconducting coil is made at a joint in the octagonal outer return layers. Thus the cryogenic utilities are at an angle of  $22.5^\circ$  from vertical.

The pole pieces of the magnet are formed of nesting rings on each end in order to satisfy the functions of magnetic flux return, support structure, access and assembly. The outer collar with an octagonal outside and circular inside supports the return yoke slabs of

Table 1  
Parameters of the CLEO II magnet

Manufacturer	Oxford Instruments, Ltd.
Magnetic field	1.5 T, uniform to $\pm 0.2\%$ over 95% of the solid angle in the drift chamber volume
Diameter	2.9 m clear bore, 3.1 m coil
Length	3.5 m coil, 3.8 m cryostat
Coil, electrical	3300 A, 4.6 H, 25 MJ
Weight	7000 kg cold mass; 20000 kg cryostat; 800000 kg steel
Stability	Intrinsically stable, quenchback from high purity Al secondary
Cooling	Indirect, thermosyphon

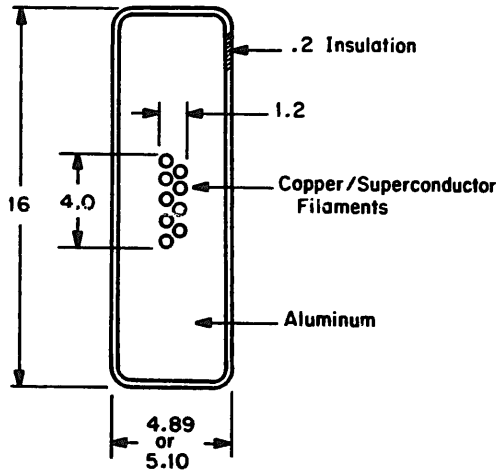


Fig. 4. Schematic cross section of the superconducting wire. All dimensions are in millimetres.

steel and the cryostat. Penetrations provide access to the adjustable radial and axial supports for the coil. Two more nesting rings and the inner pole are assembled in a way that allows the installation of the detector elements. Holes and grooves are cut in them for the passage of cables and lightpipes. The inner pole pieces of 2 m diameter and the nearby CESR quadrupoles rest on rails so that they may be withdrawn to provide access to the ends of the drift chamber and other components near the interaction point.

### 2.3. Superconducting coil

The design of the coil was driven by the primary goals listed above. The choice of operating current, 3300 A, is a compromise between low heat generation in the leads and large conductor size with its simpler construction and ease of protection. The choice of a  $5 \times 16 \text{ mm}^2$  aluminum stabilized superconductor increased the point source energy necessary to cause a quench from less than 10 mJ in the CLEO I coil to 6 J in the final CLEO II design. The high purity aluminum with resistivity ratio,  $\text{RRR} = R(300 \text{ K})/R(4 \text{ K}) = 1000$ , was coextruded by Vacuumschmelze over Cu-NbTi flat cable with a helical wind. Fig. 4 illustrates this wire. An eleven-strand cable was used for the inner layer and a nine-strand cable for the outer layer of the two layer coil. Eight pieces of conductor were used altogether in the coil. To improve the field uniformity, the current density over the end sections was increased by 4% by reducing the width of the conductor from 5.1 to 4.9 mm.

To support the magnetic hoop stress, Oxford Instruments chose to wind the coil on the inside of a structural aluminum shell. For self-protection a single turn secondary in the form of a 1.5 mm thick, high purity ( $\text{RRR} > 2000$ ) aluminum sheet is first fastened to the inside of the shell. This sheet is an excellent thermal and electrical conductor and magnetically closely coupled to the primary winding. Its resistance is adjusted

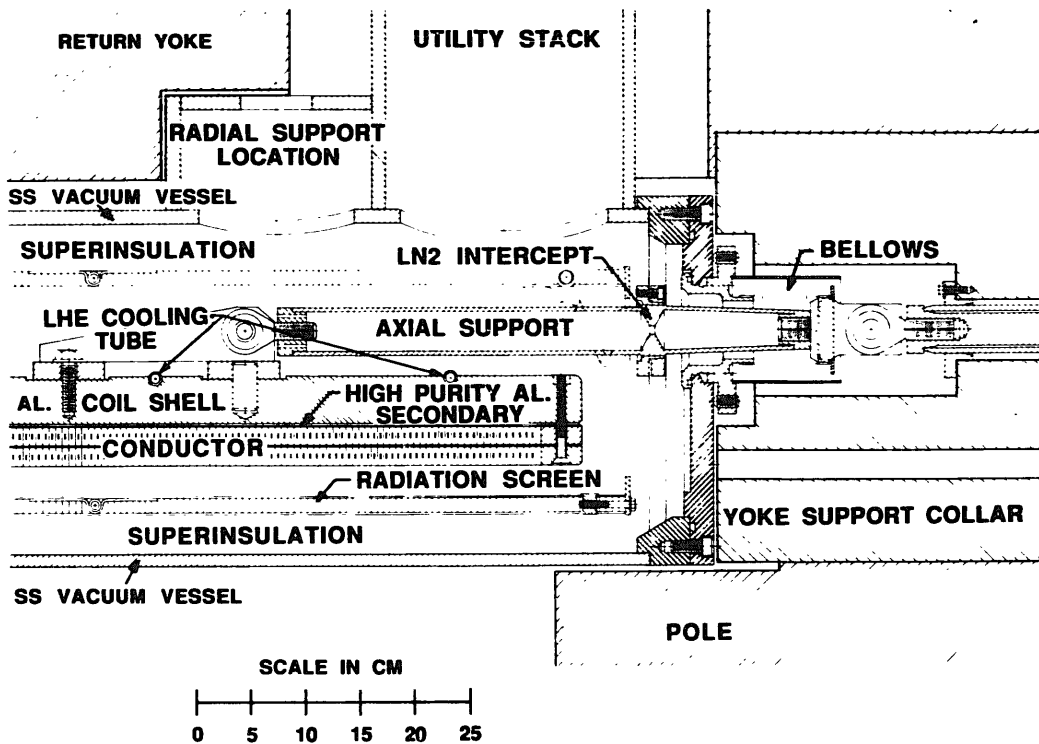


Fig. 5. Section near one end showing the cryostat, radiation screen, superconducting windings in the aluminum shell and an axial support fixture.

to protect the coil during a quench (about 1 min time constant) but not generate excessive heat during normal charging and discharging (about 80 min time constant). The all aluminum construction greatly minimized thermal stresses.

The winding was done by feeding the conductor in compression on the inside of the coil shell, slowly rotating on a turntable, synchronized to the conductor feed. Several stations along the conductor path outside the shell prepared the conductor (shot blasting, degreasing, drying, burr detection and taping). The last station was a platform inside the coil form that used a caterpillar feed and runway to push the conductor onto the previous turn. The platform rose as 650 turns per layer were added to the coil. Using an inductive technique, Oxford Instruments monitored the coil for turn-to-turn faults. The seven joints on the coil were made by reducing the thickness of the conductor from 5 to 3.3 mm, laying two such lengths together and making two edge welds, using a high purity aluminum filler over a length of 800 mm. Joint resistance is estimated to be  $2 \times 10^{-10} \Omega$ . The joints between the coil and current leads were made by copper-plating and soft-soldering, thus yielding demountable joints. After winding, the coil was vacuum impregnated with an epoxy resin and cured at 120°C. A section near the end of the coil is shown in fig. 5.

#### 2.4. Thermosyphon system

A key design goal was to avoid quenches in cases of utility or refrigerator problems. This has been achieved by locating above the magnet a 700 l dewar which delivers cold liquid helium to a manifold on the bottom of the coil. This manifold supplies 32 riser pipes fastened to the outside of the coil shell where the helium absorbs heat and decreases in density. The buoyancy of lower density liquid helium and gas bubbles rising in the pipes draws the liquid around the circuit in one direction. The two-phase flow returns to the dewar where it separates. This natural flow circulation, referred to as a thermosyphon, is self regulating, reliable and avoids the use of a liquid helium pump. Some of the cold gas cools the current leads and the neck of the dewar; the rest returns cold to the refrigerator. The small inventory of liquid helium in the coil means that the gaseous helium generated during a quench can be accommodated in a benign way. The 700 l dewar provides over one day of operation with disabled refrigeration. Valves inside the dewar allow forced flow cooling from the refrigerator during cooldown when there are no significant buoyancy effects to drive the thermosyphon circulation.

The details of the thermal coupling between the risers and the coil shell are important to both ramping

the coil and its protection in case of a quench. The risers are stainless steel tubes embedded in indium-packed channels cut in the coil shell. The thermal impedance of this interface turned out to be higher than anticipated, limiting the cooling capacity of the thermosyphon to about 200 W. This limits our charging voltage to about 3 V or ramping rate to about 0.7 A/s, thus requiring a time of about 1.5 h to reach full current. Temperatures of 6 K on the coil shell are typical during ramping. At the high heat loads encountered in a quench the thermosyphon cooling loop becomes saturated as the helium in the risers completely evaporates. The cooling capacity of this dried out condition can be set by adjusting a constricting valve in the loop. It is set at the few hundred watts level but with the higher than expected thermal impedance of the riser-coil shell interface, the drying out of the thermosyphon is not critical.

#### 2.5. Radiation screen

Thermal isolation of the coil is provided by a liquid-nitrogen cooled radiation screen which is insulated from the cryostat by about 100 layers of aluminized Mylar superinsulation. The screen consists of inner and outer cylinders of aluminum honeycomb panels 15 mm thick with aluminum tubing bonded to one skin. The heat load to liquid nitrogen is slightly less than 50 W. The coil-side surfaces of the radiation screen are lined with a low emissivity material to reduce the radiant heat load on the coil. Fig. 5 includes a portion of the radiation screen. During cooldown of the system, a controller mixes liquid and gaseous nitrogen to provide a controlled ramp of the temperature of the radiation screen over a period of days, thus matching the coil cooldown rate and avoiding thermal stresses. During normal operation, the radiation screen piping is filled with liquid nitrogen.

#### 2.6. Refrigeration system

The superconducting coil is cooled by either of two Koch process model 1430 liquefiers. These previously cooled the CLEO I coil. They have mechanical engines with a refrigeration capacity of 100 W, liquefaction capacity of 40 l/h or combinations between. The system is interconnected to have nearly complete redundancy for the active components, the refrigerators and compressors. In addition to the 700 l dewar above the coil there is a 1000 l dewar that can be filled by either refrigerator or from a vendor's dewar. In normal operations the refrigerators are switched approximated every 12 weeks and the 1000 l dewar is not used. The various sources of helium are connected in a large cryogenic valve box to a coaxial transfer line going to the 700 l dewar. This low-loss coaxial line, made by

Kabelmetal Electro GmbH, also returns cold helium gas and carries liquid nitrogen for the radiation shield. The line is a semi-flexible design that permitted operation in the test location without rebuilding. Estimates of the cryogenic requirements are 8 W for the coil with cold gas return, a similar number for the valve box and transfer lines and 14 l/h liquid equivalent with warm gas return. The refrigerators operate without attention during nights and weekends.

### 2.7. Current leads

The 3300 A current leads were designed by Oxford Instruments to have low heat conduction from room temperature to the liquid helium while maintaining a margin of safety against overheating in case of loss of helium gas coolant for the 80 min magnet rampdown time. The extra thermal mass for this safety condition was obtained by adding material in the form of fins. Before installation the leads were tested to 110% of normal operating current and at operating current with no gas cooling. The performance indicated that the magnet would ramp down safely without quenching. The control, monitoring and alarm systems make operation of the leads automatic. The helium gas flow is controlled at the warm return end by a regulating valve that is set by the temperature of the lead at a point 20% from the warm end. This regulation adjusts for the current in the lead and the return pressure of the helium compressors. The controller has two different temperature set-points: one optimized for refrigerator operation and the other "over-cooled" for dewar operation. A second set of controllers powers heaters on the warm ends of the leads to prevent condensation.

### 2.8. Cryostat and supports

The stainless steel cryostat, which supports the 30 ton weight of the CsI calorimeter, is supported by the massive steel return yoke. The cryostat consists of a 12 mm thick outer cylinder, a 10 mm inner cylinder and two 20 mm thick end flanges which are bolted and sealed with O-rings. The coil is movable inside the cryostat in order to accommodate thermal contraction, to minimize magnetic decentering forces and to align the magnetic axis. The titanium supports are adjustable at 4 K through their coupling to bellows sealed ports in the cryostat wall and end flanges. There are four axial supports, all at the service end of the coil, acting either in tension or compression. They have a stiffness of several times the magnetic decentering forces. An axial support is shown in fig. 5. There are sixteen radial/azimuthal supports arranged in pairs tangential to the coil to act purely in tension. Strain gauges on all supports monitor the magnet loads and weight.

### 2.9. Instrumentation and monitoring

The status of the CLEO II magnet and refrigerators is monitored by a combination of data acquisition systems and a VAX workstation. The primary data acquisition system is an LSI-11/70 based computer which controls analog and digital hardware. This system (called the PX-11 and made by ADAC, Inc.) acquires data from the various sensors and writes it to a circular history buffer once every second. The coil temperatures as measured by Rh-Fe resistance sensors are separately digitized by a DORIC Datalogger. Similarly the temperatures in the refrigerators are measured using two readout controllers (made by Scientific Instruments, Inc.) for silicon diode sensors. The PX-11 then queries the DORIC and silicon diode controllers over RS-232 serial links. The history buffer is deep enough to hold about 40 min of data, 130 variables of 16-bit length recorded at one second interval.

A longer term record of the system status is kept by the VAXstation. The VAX queries the PX-11 over another RS-232 link once every 5 s for the latest readings. The VAX checks the variables and can raise an alarm if any variable is out of range. If a coil quench is detected, the VAX instructs the PX-11 to dump out its history buffer, with data in one-second intervals, from 20 min before the quench to 20 min after, thus providing a detailed pre- and post-quench history. The VAX can store about a month's history in the five-second intervals. This is thinned to five-minute intervals and saved on tape for a permanent record.

The system variables that are monitored include temperatures, pressures, flows, strains, vacuum, helium level, currents and voltages. All serious fault conditions are sensed with hardware-wired alarms that automatically turn off the power supply. The computer alarms do not directly cause any action to be taken. This requires manual intervention. The entire instrumentation and monitoring electronics are powered by an uninterruptible power system.

### 2.10. Coil acceptance tests

A first set of tests of the superconducting coil was made at Oxford Instrument's construction facility at 40% of full current without the steel yoke. Vacuum integrity, cryogenic heat loads, thermosyphon performance and magnetic excitation were measured. The thermosyphon cooling capacity was tested by energizing built-in heaters at various levels. A quench was initiated by closing the thermosyphon with the heaters on. The quench started when the conductor reached 9.1 K, as expected. The time evolution of the quench and the maximum temperature (32.7 K) matched a quench model prediction (34.5 K).

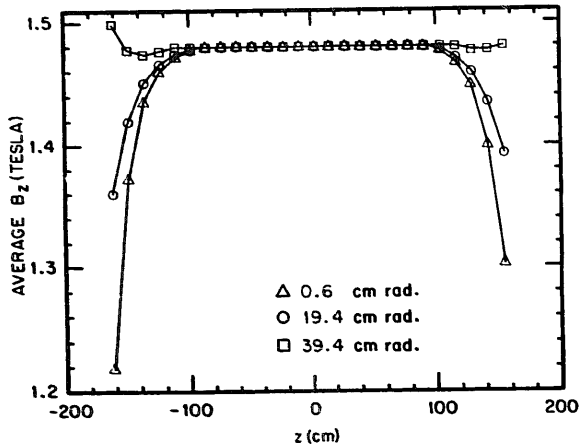


Fig. 6. Plot of the axial magnetic field for three radii. The data are averaged over azimuth.

The coil and two layers of the return yoke were assembled away from the beam line [9] at Cornell in 1988. After a cooldown time of twelve days, using one refrigerator, the tests started with two self-induced quenches at full current. Their origin is still not understood, but were typical of training events. The current decayed during a quench in about one minute. The coil reached an average temperature of 65 K in agreement with prediction. After operating the coil at the full field of 1.5 T at 3300 A, the temperature margin was tested by increasing the coil temperature 1.5 K with the heaters, out of an expected margin of 2.2 K. The current margin was explored by running at 102% of the full current. Another quench occurred recently after the coil was warmed and re-cooled. The coil has been warmed and re-cooled several times in the past two years without experiencing subsequent quenches. This recent quench is not understood.

### 2.11. Magnetic field homogeneity

The magnetic field was mapped with a three-axis Hall probe referenced to a fixed NMR probe. Traverses in  $z$  (the axial direction) were made at fixed radius and azimuth. The data, averaged over azimuth, were fit to appropriate polynomials in  $r$  and  $z$  in a manner consistent with Maxwell's equations. Fig. 6 shows typical results for  $B_z$ . Field uniformity over the 2 m long by 1 m radius drift chamber volume is better than 0.1%. These measurements in the test location were taken without the CESR samarium-cobalt permanent magnet interaction quadrupoles in place. Calculations using the program TRIM indicate that the effect of these quadrupoles is localized to forward directions, i.e., near the physical quadrupoles, with the realistic condition that the permanent magnet material has a differential magnetic permeability of 1.03. The external quadrupole field of this material has been

ignored in this calculation but its effect is small and falls off as  $1/r^3$ . Overall the magnetic field is uniform to 0.2% in the drift chamber volume over 95% of the total solid angle. The tracking program assumes a uniform field.

### 2.12. Magnetic field absolute value

During normal data-taking the magnetic field is monitored with an NMR probe that is located a few centimetres beyond the end of the drift chamber. This is not the same position as in the field mapping when the samarium-cobalt quadrupoles were not installed. Therefore a calibration of the average, effective magnetic field in the drift chamber volume has been made using event reconstruction involving  $\mu$  pairs and the known masses of the particles  $D^0$ ,  $\phi$  and  $K^0$ . This yielded a correction to the magnetic field at the centre of the magnet of 0.11% compared to the field measurement with the NMR probe, which is near the magnet pole, and the longitudinal field mapping. This correction is within the estimated accuracy of the measurements.

## 3. Tracking system

### 3.1. Overview

Charged particle trajectories are measured in CLEO II with a set of three concentric, cylindrical wire drift chambers as shown in fig. 2. The common axis of the chambers is aligned along the direction of the storage ring beams. Different goals are achieved with each of the three chambers that would be more difficult to simultaneously meet with a single chamber. The outer drift chamber, with radius from 17.5 to 95 cm, is used primarily to measure charged particle momentum vectors at the vertex. Momentum transverse to the beam axis,  $P_T$ , radial distance of closest approach of the track extrapolation to the beam line, and the azimuthal direction,  $\phi$ , are measured with 40 axial (parallel to the beam axis) wire layers. Longitudinal measurements, polar angle and the longitudinal distance from the centre of the interaction region to the extrapolation of the track to the beam axis, are measured with 11 small angle stereo wire layers and two layers of segmented cathode readout.

In a 1.5 T field, particles with a  $P_T$  of 90 MeV/c cross only seven layers in the outer drift chamber before curling around. Transverse momentum is then better measured in the intermediate drift chamber. This chamber, originally installed as a vertex detector, has ten axial wire layers with radius from 8.4 to 16.0 cm for  $P_T$  and  $\phi$  measurements. On average, the layer spacing and cell width is 70% that of the outer drift chamber, providing better granularity for separating

tracks. The polar angle is measured with two layers of segmented cathode readout in addition to charge division on all wires. The inner vertex detector has six longitudinal wire layers with radius from 4.7 to 7.2 cm. This provides the most precise transverse direction measurements for determining particle directions and separating primary from secondary vertices.

The drift chambers provide acceptance that is homogeneous over azimuth for the polar angle range  $|\cos \theta| < 0.90$ . However, track reconstruction efficiency and resolutions are poorer at polar angles below  $45^\circ$  ( $|\cos \theta| > 0.71$ ) because of the reduction in the number of layers. Each of the three drift chambers is described below. This is followed by a description of the readout electronics and the gas circulation system. Finally, our current understanding of the momentum, direction and specific ionization resolutions is discussed.

### 3.2. Outer drift chamber

The outer drift chamber (DR) has been previously described [7]. This is a small cell device with nearly equal size rectangular cells filling the volume. A total of 12240 sense wires and 36240 field wires are arranged in a pattern of 51 layers of cells, with three field wires for each sense wire. Axial layers are grouped by three or five, with equal number of wires per layer within each group. To provide local resolution of the drift distance sign ambiguity, sequential layers are offset by  $1/2$  cell in azimuth within these layer groups. Neighbouring layer groups, which have different numbers of wires per layer to preserve a nearly equal cell size, are separated by single stereo layers as illustrated in fig. 7. There are 40 axial layers and 11 stereo layers. (See table 2 for a description of the wire layers in all three CLEO drift chambers.)

Segmented cathode surfaces, rather than field wires, shape the field cage on the inner surface of layer 1 and the outer surface of layer 51. Segmentation is about 1 cm along the beam direction so that the image charge of the avalanche at the wire is spread over three pads on the cathode. The cathode is divided into 16 (8) azimuthal sections in the inner (outer) cathode, each section covering 6 (48) wires, to reduce confusion of cathode signals correlated to different sense wires.

Mechanical support for the wires is provided by 3.175 cm thick annular aluminum endplates separated by 193 cm at the inner surfaces (see fig. 8). The endplates were ground with flat surfaces, but as installed, bow inward by 0.79 cm at the inner radius due to the total force of the tensioned wires. At the outer radius, the endplates are screwed to a ring which stiffens them against the bowing forces of the wires and attaches them to the outer shell (see fig. 9). The outer shell supports the tension of the wires and pro-

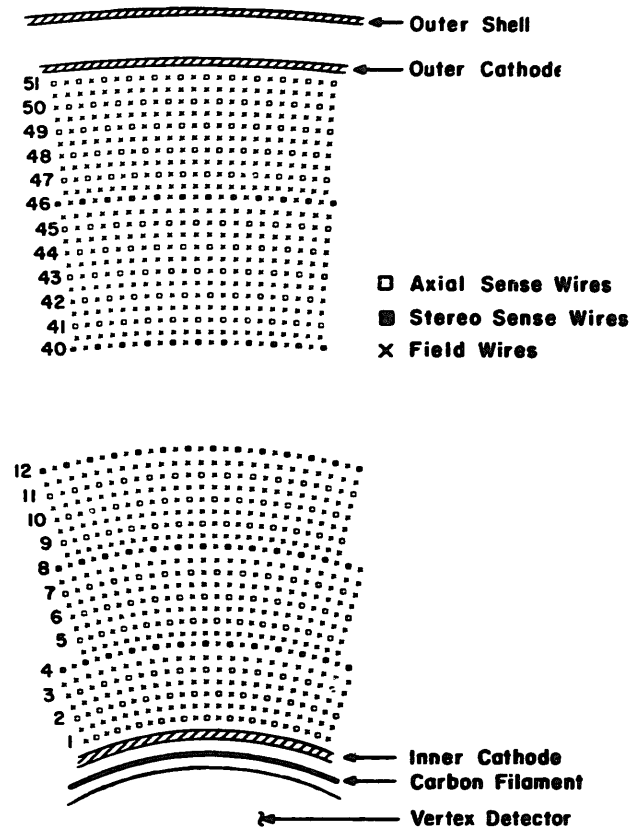


Fig. 7. Outer drift chamber cell structure.

vides the gas seal. It is made of composite panels to reduce the total material in front of the electromagnetic calorimeter. The inner radius gas seal consists of a carbon filament reinforced epoxy tube. This is attached to the inner edge of the annular endplates with stainless steel rings as displayed in fig. 9. Space is left over most of the circumference to feed through the inner cathode traces. The outer support ring also has screw holes to attach handles during transport and to locate the chamber inside the magnet.

The sense wires are 20  $\mu\text{m}$  diameter gold plated tungsten tensioned with 50 g. The field wires of layers 1 to 40 are 110  $\mu\text{m}$  gold plated 5056-aluminum tensioned with 170 g. At larger radii, the field wires are 110  $\mu\text{m}$  gold plated copper-beryllium tensioned with 270 g. The use of copper-beryllium wires introduces additional material that reduces tracking resolution. However, at large radii, with short moment arm after scattering, the effect of the higher  $Z$  material is reduced. Wires are held by copper/brass crimp pins, insulated from the aluminum end plates by plastic bushings made of ULTEM 1000, a polyetherimide resin [10] (see fig. 8). Holes were drilled in the endplate to an accuracy of 37  $\mu\text{m}$ , rms. The position of the 20  $\mu\text{m}$  sense wires in the 100  $\mu\text{m}$  centre hole of the crimp pins is undetermined by 23  $\mu\text{m}$ . Contributions to the uncertainty of the wire location due to the error in

concentricity of the crimp pins and plastic bushings are small compared to these two errors resulting in a total uncertainty of 45  $\mu\text{m}$ , rms.

The method of holding the wires produced two problems in the reliability of the outer drift chamber. During operation, in the period from 1986 to mid 1990, there have been occurrences of broken wires at the rate of one per six weeks and shorted bushings at the rate of one per week. Wire breakage occurs mostly in the aluminum field wires at the point where the crimp

was made with the wire under full tension. The crimping of aluminum is very sensitive because aluminum is softer than the copper in the crimp pin and aluminum tends to creep under large stress. There is only a small window in the amount of crimp force where the force is large enough to hold to wire from slipping and small enough to avoid breakage. Bushing shorts occur in sense wire bushings where the crimp pin, at positive high voltage, is separated from the endplate, which is at ground, by only 0.75 mm of bushing material. These

Table 2

The central detector tracking layer topology. The radius of the sense wires, the number of sense wires per layer, the stereo angles of the outer chamber, and the total material between the beam line and the sense wire (in units of %-radiation-length) are listed for each chamber. One half the length of the sense wires for each chamber are: PTL, 25.0 cm; VD, 35.0 cm; DR, 96.2 cm. These numbers combined with the sense wire radius can be used to calculate the angular acceptance of each layer, i.e.  $\max(\cos \theta)$

Layer No.	Radius [cm]	Wires per layer	Stereo angle [deg]	Material in front [% R.L.]	Layer no.	Radius [cm]	Wires per layer	Stereo angle [deg]	Material in front [% R.L.]
PTL					VD				
1	4.73	64	0	0.46	7	8.47	64	0	1.38
2	5.15	64	0	0.52	8	9.22	64	0	1.38
3	5.60	64	0	0.58	9	10.04	64	0	1.39
4	6.10	64	0	0.64	10	10.93	64	0	1.39
5	6.64	64	0	0.70	11	11.91	64	0	1.40
6	7.23	64	0	0.75	12	12.78	96	0	1.40
					13	13.52	96	0	1.41
					14	14.31	96	0	1.41
					15	15.15	96	0	1.42
					16	16.03	96	0	1.42
DR					DR				
17	19.90	96	0	2.51	43	56.42	240	0	2.73
18	21.30	96	0	2.52	44	57.93	252	5.57	2.74
19	22.71	96	0	2.52	45	59.23	264	0	2.74
20	24.21	108	3.77	2.53	46	60.64	264	0	2.75
21	25.52	120	0	2.54	47	62.04	264	0	2.66
22	26.92	120	0	2.55	48	63.55	276	-6.01	2.77
23	28.33	120	0	2.56	49	64.85	288	0	2.78
24	29.83	132	-4.22	2.57	50	66.26	288	0	2.79
25	31.14	144	0	2.57	51	67.66	288	0	2.80
26	32.54	144	0	2.58	52	69.16	300	6.41	2.80
27	33.95	144	0	2.59	53	70.47	312	0	2.81
28	35.45	156	4.69	2.60	54	71.87	312	0	2.82
29	36.76	168	0	2.61	55	73.28	312	0	2.83
30	38.16	168	0	2.62	56	74.78	324	-6.45	2.84
31	39.57	168	0	2.63	57	76.09	336	0	2.85
32	41.07	180	-4.69	2.63	58	77.49	336	0	2.85
33	42.38	192	0	2.64	59	78.90	336	0	2.86
34	43.78	192	0	2.65	60	80.30	336	0	2.87
35	45.18	192	0	2.66	61	81.71	336	0	2.88
36	46.69	204	5.13	2.67	62	83.21	360	6.89	2.89
37	47.99	216	0	2.68	63	84.52	384	0	2.90
38	49.40	216	0	2.69	64	85.92	384	0	2.91
39	50.80	216	0	2.69	65	87.33	384	0	2.91
40	52.31	228	-5.56	2.70	66	88.73	384	0	2.92
41	53.61	240	0	2.71	67	90.14	384	0	2.93
42	55.02	240	0	2.72					

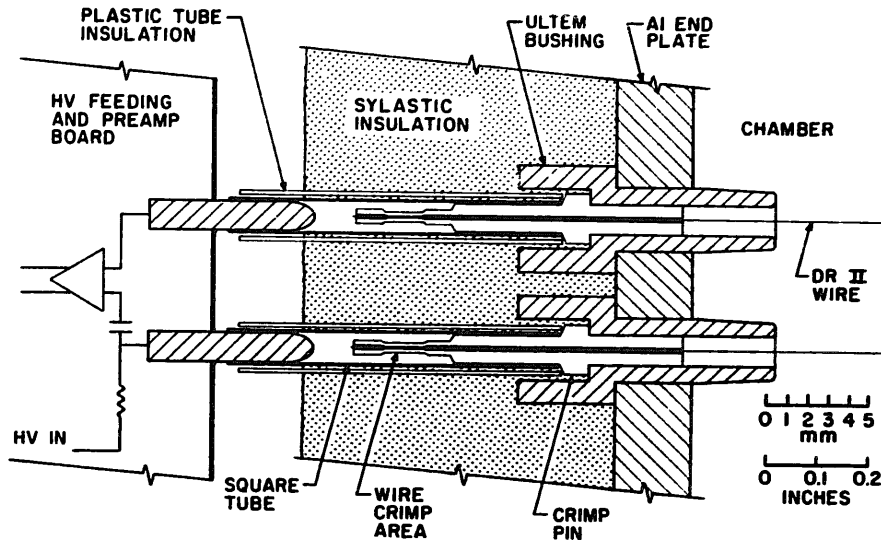


Fig. 8. Outer drift chamber endplate, feedthroughs and wires. The sense wire is connected to the high voltage.

shorts occur in an isolated region in radius, indicating that there was a quality control problem in the size of the pins, bushings, or drilled holes that results in stresses on the bushings which accelerate the formation of cracks and electrical breakdown. It has been found, although not completely understood, that the frequency of both of these problems are greatly reduced by holding the end plate temperature to less than 25°C.

The segmented cathodes are made of single sided 25 μm aluminium foil bonded to 188 μm Mylar sheets [10]. For the inner cathode surface, 32 sheets are etched as shown in fig. 10. Each active cathode pad covers 1 cm in the axial direction and 7.53 cm, corre-

lated to six wires, in azimuth. Two sheets are used to cover the length of each of the 16 azimuthal sections providing active area for  $|\cos \theta| < 0.92$ . The sheets are bonded to the outer diameter of a Rohacell [10] tube so that the signal and ground traces of each sheet are covered by the active pads of an adjacent overlapping sheet. Traces, bonded to the Mylar substrate, pass from the outer surface to the inner surface of the support tube through a slot, then through a slot formed between the carbon filament inner gas seal and the inner diameter of the annular end plate as shown in fig. 9. The outer cathode is divided in azimuth into eight panels. There are 192 active pads measuring 0.95 cm in the longitudinal direction and 71.3 cm in the

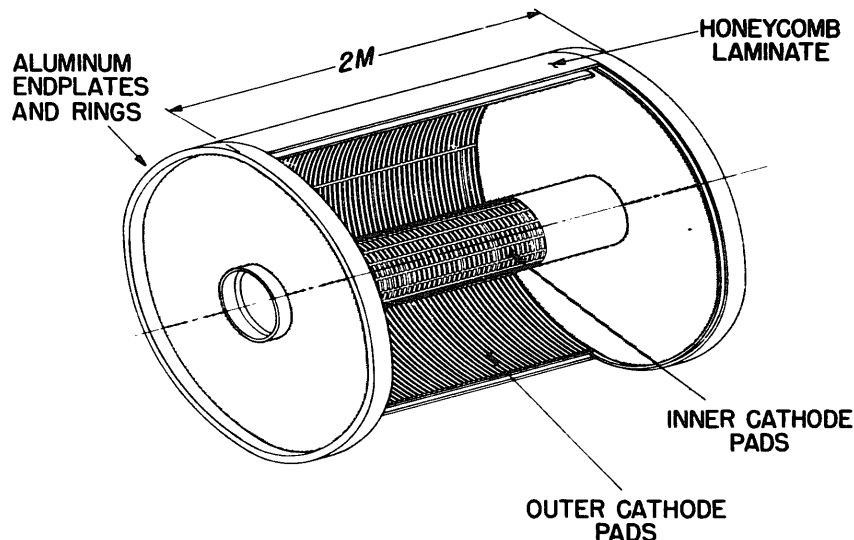


Fig. 9. Outer drift chamber, endplates, inner and outer support structure.

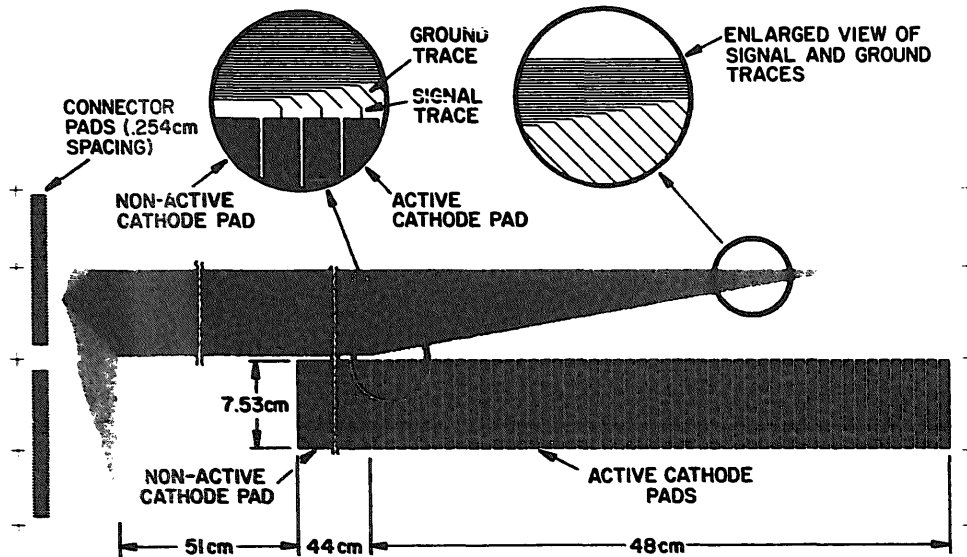


Fig. 10. Outer drift chamber, inner cathode etched surface.

azimuthal direction, contributing to the field cage of 48 wires. The full length of each panel is 1.826 m, providing an active area for  $|\cos \vartheta| < 0.71$ . The panels are composite. The inner face is an etched aluminized Mylar sheet which forms the active surface. The outer surface is Lexan [10] over a layer of fibreglass. An inner core, needed to provide thickness for rigidity, is plastic honeycomb, 6.35 mm thick. Traces, etched in the aluminum on the Mylar substrate, wrap around an axial edge from the inside surface of the panel to the outside. There, the traces are connected to a twisted pair cable which is brought outside the gas volume through slots machined in the endplate.

### 3.3. Intermediate drift chamber (vertex detector, VD)

The intermediate drift chamber was first installed in CLEO in 1984 as a vertex detector. A total of 800 sense wires and 2272 field wires are arranged to form 10 layers of small hexagonal cells, with three field wires for each sense wire, as shown in fig. 11. All wires are axial, and are divided into two groups with 64 cells per layer in the inner group (layers 1 to 5), and 96 cells per layer in the outer group. Ambiguity of the sign of the drift distance can be resolved locally with half cell staggering from layer to layer within the group. To allow for running at a higher voltage and provide for more ionization the chamber is operated at 20 psi absolute pressure. The gas is similar to that in the outer drift chamber, 50% argon and 50% ethane but with a small amount of water added to reduce the amount of organic compound building up on the wires.

As in the outer drift chamber, segmented cathode surfaces, rather than wires, shape the field cage on the inner surface of the first layer and the outer surface of

the last layer. Segmentation is 5.85 (6.85) mm along the beam direction on the inner (outer) cathode surface so that the image charge of the avalanche at the wire is spread over three pads on the cathode. Both inner and outer cathode surfaces in the intermediate drift chamber are divided into eight azimuthal sections to reduce confusion of cathode signals correlated to different sense wires. To provide further measurements in the axial direction, the sense wires are made of a nickel-chromium alloy with about three times the resistivity of gold plated tungsten and are instrumented for charged division measurements. The field wires are made of aluminum.

Mechanical support for the wires is provided by copper clad G-10 annular endplates separated by 70

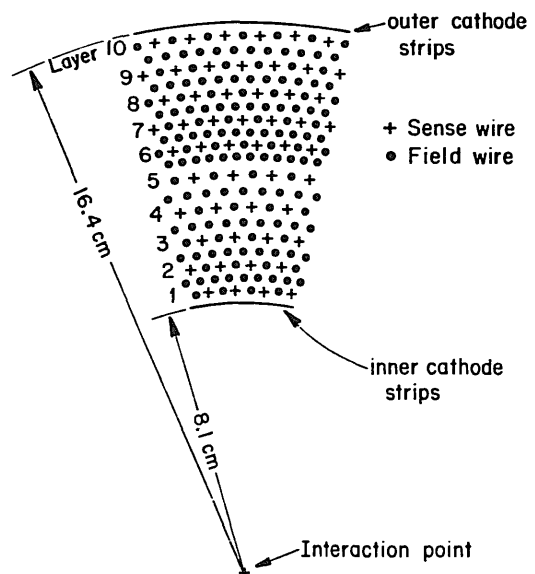


Fig. 11. Intermediate drift chamber cell structure.

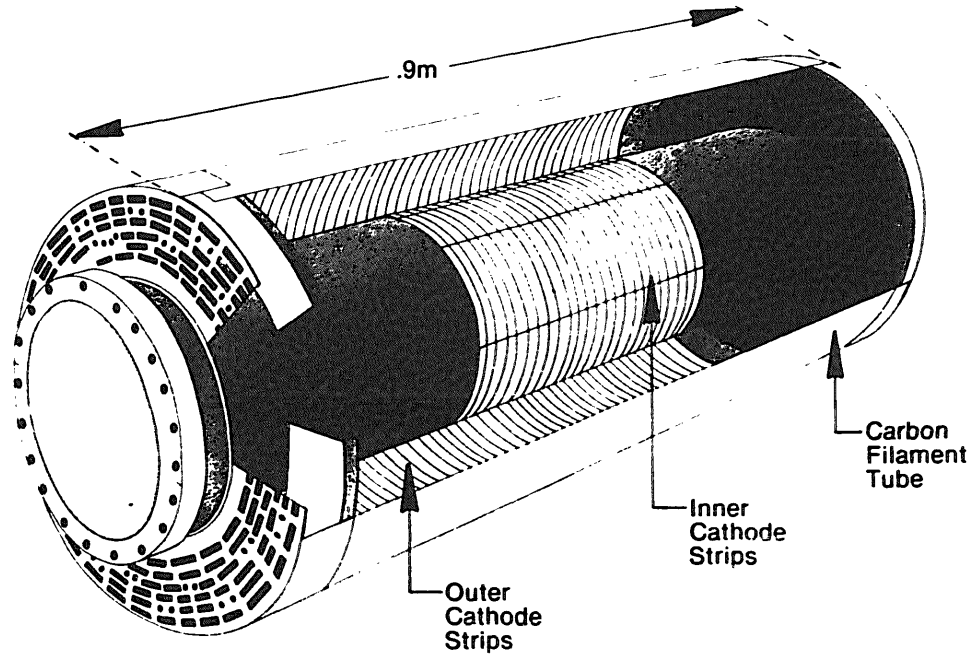


Fig. 12. Intermediate drift chamber.

cm at the inner surface (see fig. 12). The endplates are supported by carbon filament reinforced epoxy tubes at the inner and outer radii. On the inner surface, the carbon filament tube is pinned and epoxied into position. On the outer surface, the carbon filament tube is sealed to the endplates with O-rings, and screws hold it in position. Wires are positioned directly by ridge slot surfaces machined on the inside surface of each G-10 endplates at the appropriate radii, and holes drilled on the other side. The radial positions of the wires are defined by the slots machined 5.1 mm deep into the gas volume side of the endplates. Matching holes are drilled 21.6 mm deep into the outside surface of each endplate, for each wire (see fig. 13). These holes define the azimuthal position, as the wires are pulled to one side before pinning. The hole and slot overlap to form a “D” shape through which the wire can be easily inserted and positioned without the added uncertainties of insulating bushings and crimp pins as in the outer drift chamber. Hollow cylindrical bushings are inserted into the holes on the outside of the endplate. A tapered pin inserted into the bushing holds the wire in place by friction. In the case of field wires, the bushings are brass to provide an electrical connection to the copper cladding on the endplate, while for the sense wires, the bushings are made of Delrin [10].

The segmented cathodes in the intermediate drift chamber are made of 76  $\mu\text{m}$  Mylar sheets with 8  $\mu\text{m}$  aluminum foil bonded on both sides. Sheets are etched as shown in fig. 14 with each sheet covering one half of the active length of the chamber and 1/8 of the

azimuth. The signal lines for the active pads are then on the reverse side of the Mylar. To provide a low impedance electrical connection from the active pads to the pick-up pads that terminate each signal line, a small hole was made through the Mylar which was filled with silver ink. Each of the etched sheets are bonded directly to the structural carbon filament tubes that define the inner and outer radii of the chamber. The signal lines are brought outside the gas volume through the glue joint or O-ring joint where the structural tube connects to the endplates.

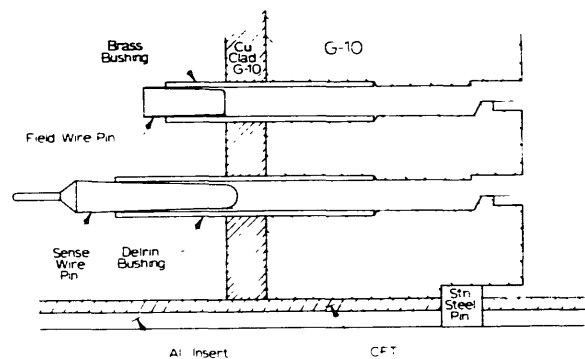


Fig. 13. Intermediate drift chamber wire support.

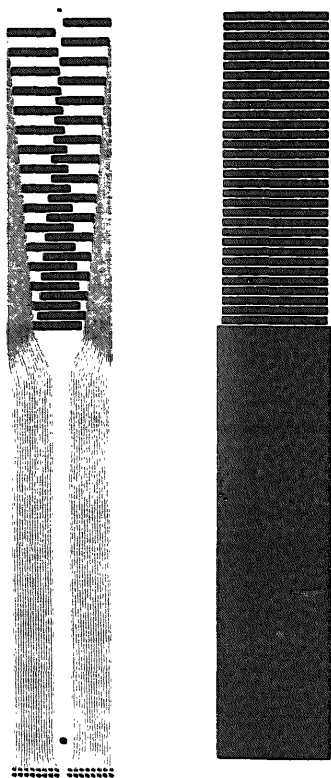


Fig. 14. Intermediate drift chamber cathodes.

### 3.4. Inner drift chamber (precision tracking layers, PTL)

The inner tracking detector was constructed and installed in CLEO II in 1989. It is a six-layer tube chamber, with 64 axial wires per layer and half cell staggering between sequential layers with the purpose of making precise measurements of transverse particle direction near the interaction point. No longitudinal direction measurements are made with this chamber. It is similar to a three-layer device that was installed in CLEO I from 1986 to 1988, and to a vertex detector

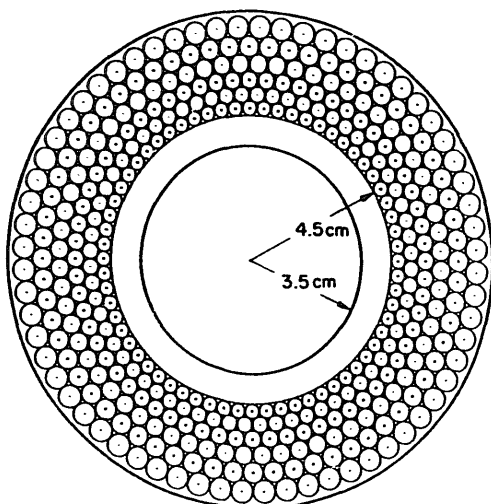


Fig. 15. Inner vertex detector component tube alignment.

built for the AMY detector at KEK [11]. The field cage for each wire is defined by an aluminized Mylar tube, instead of cathode wires as utilized in the outer and intermediate drift chambers. The diameters of the cathode tubes and the radial spacings of the layers are determined by the requirement that each tube make contact with all neighbouring tubes in that and adjacent layers. Thus, all of the tubes are glued together to form a unit that provides the mechanical stability and internal alignment of the chamber. Alignment of the tubes was fixed at the time of bonding them together with a temporary system of rods and endplates. A ground steel rod was inserted into each of the 384 tubes to hold its shape and position. In addition to these, two other layers of rods, inside the innermost and outside the outermost real layers, were used to better define the positions of the boundary layers. The eight layers of rods, with the rods of the six internal layers inside the aluminized Mylar tubes, were then stacked around a cylindrical mandrel and fixed in position by precision drilled endplates as shown in fig. 15. Once stacked into this rigid aligned structure, the component tubes were bonded with an epoxy.

Aluminum bushings are inserted into each of the aluminized Mylar cathode tubes, shown in fig. 16. Held in place by conductive epoxy, these provide electrical contact to the aluminized inner walls of the tubes. For the outer four layers, electrical contact is made from the cathode surfaces, through the bushing, to an aluminum endplate, which also serves to mechanically stabilize the assembly of tubes in the absence of the system of alignment rods and plates. The inner two layers are spaced too closely compared to the diameter of the outer section of the aluminum bushing to allow the endplate to be extended down to this radius. Instead, the cathodes of these layers are electrically connected together and to the endplate by bridging the aluminum bushings with conductive epoxy.

Sense wires are 15  $\mu\text{m}$  gold plated tungsten, tensioned at 22 g. They are positioned in ULTEM bushings inserted into the ends of the aluminum bushing described above as shown in fig. 16. Inside the bushing, a "v" groove provides the precise alignment of the wires. Tension is held by a friction pin inserted into the bushing and epoxy. Gas flow is maintained in this tube design, with small holes in the insulated bushing providing a route on each side of the tubes. The entire detector is encapsulated by a 21  $\mu\text{m}$  Mylar wrap, with G-10 endplates. This defines the gas volume and provides a means to make electrical connections from the fragile friction pins holding each sense wire to cable connectors mounted on the endplates.

### 3.5. Readout

All chambers are operated with positive high voltage applied to the anode wires and cathodes (wires and

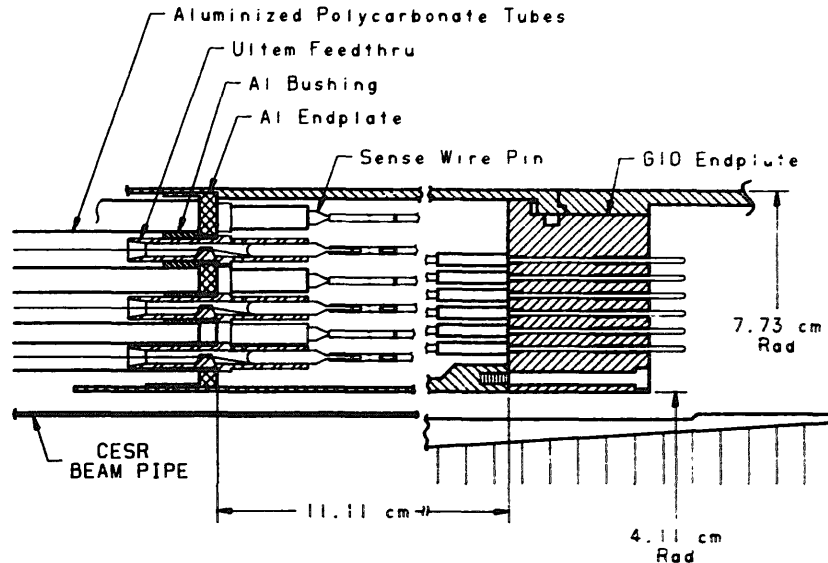


Fig. 16. Inner vertex detector endplate, wires and bushings.

pads) held at ground. Low impedance connection of the cathodes to ground is required to operate the chambers in the CESR storage ring environment. Each anode wire is connected through a blocking capacitor to a preamplifier mounted on the endplate of the outer drift chamber (see fig. 2). On the outer drift chamber, the blocking capacitors, preamplifier hybrids, and high voltage distribution resistors are mounted on printed circuit boards (24 channels per board) that are connected directly to the anode crimp pins. There are a total of 515 of these boards on the two ends of the chamber: with odd numbered layers read out on the west and even numbered layers on the east.

For the intermediate drift chamber, the VD, 95 cm of coaxial cable is used to connect each sense wire to a

discrete preamplifier mounted on the outer drift chamber endplate. To extract an axial coordinate through charge division, the wires are read out on both ends. High voltage distribution and the preamplifier input blocking capacitors are mounted on the endplate of the VD chamber.

The inner drift chamber, the PTL, is exposed to the most radiation and is the least accessible for repair. To provide the capability to turn off individual wires, the signal for each wire is brought out to a position on the face of the outer drift chamber through a coaxial cable, at high voltage. There, groups of eight channels are terminated with a printed circuit board that provides the high voltage distribution and anode blocking capacitors. These connect to discrete component preampli-

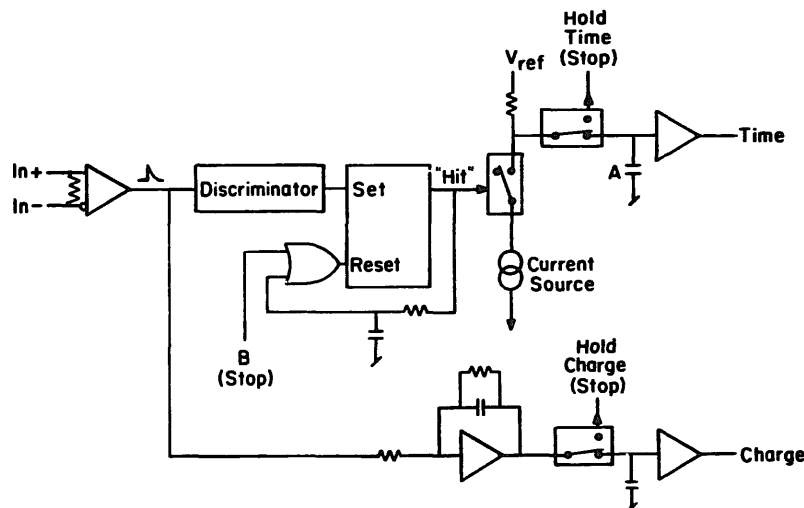


Fig. 17. Schematic of sample-and-hold circuits.

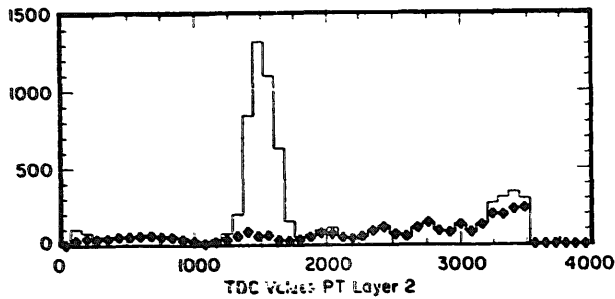


Fig. 18. Raw time of hits in the intermediate drift chamber. The histogram is from data recording with normal trigger. The data points are from channels known to have already ramped down and are currently in process of recovering.

fiers mounted along with those for the intermediate drift chamber.

Amplified differential signals are transferred over 8 m of twisted pair cable to readout electronics mounted outside the endcap muon chambers on the steel plates (see fig. 2). The sample-and-hold circuits, which measure time and pulse height (fig. 17), have only single hit capability but have proven to be adequate in the CESR environment. Rampdown of the timing capacitor, "A" in the figure, is started when the input amplified signal crosses threshold and stopped after 800 ns. In the case that the L0 trigger was satisfied (see trigger section) the timing capacitor rampdown is stopped with a gate, input at "B", typically 430 ns after the beam crossing. For specific ionization measurement, charge is integrated from the threshold crossing for a time of 900 ns for the outer (DR) and inner (PTL) drift chambers, but only 500 ns for the intermediate (VD) detector to improve the charge division resolution.

There is no active reset in the CLEO II electronics. Reset pulses create noise which may be above threshold in the timing circuits, especially of the segmented cathodes in the outer drift chamber. Presently, the time between crossings in CESR is 360 ns and the maximum drift time in the outer drift chamber, with a magnetic field of 1.5 T, is about 400 ns which does not

leave time to actively reset the electronics. Instead, all channels are reset passively with an RC time constant of about four beam crossings. This causes some nonlinearity in the time to charge relation but that is compensated for in the calibration. A more serious problem due to the reset method is that the system is sensitive to charge deposition from about 30 previous crossings. Extra hits are a problem in the two inner detectors which are closer to the beam and have less azimuthal granularity. Most extra hits can be eliminated because the time measurement is not within the limits placed by the time of the latest beam crossing and the maximum drift time as can be seen from the raw time of hits distribution in fig. 18. Channels that lie on tracks from the latest crossing, but were ramped down in a previous crossing are not used until their capacitor recovers full charge. During this time period a "stale data" bit is set on.

### 3.6. Argon-ethane gas system

The CLEO II gas system supplies all three tracking chambers (PTL, VD, DR) and the muon detectors with a mixture of 50% argon and 50% ethane ( $C_2H_6$ ). The functions of the system are to prepare the proper gas mixture, to supply an adequate and stable flow to each subsystem, to maintain a stable operating pressure, and to provide continuous monitoring of all important flows, pressures, and gas composition. The needs of each client detector differ from one another, so the characteristics of the individual gas subsystems vary in the four cases. Table 3 summarizes the gas-related properties of the detectors.

There is one common gas mixer for all the detectors. The bulk argon and ethane are passed through 10- $\mu$ m filters, and then fed into separate electronic mass flow controllers (MFCs) set to assure equal flow for the two gases. The output from the MFCs then join and accumulate in a 1300 l buffer tank at 30 PSIG for subsequent input to the detector systems.

All the subsystems are designed to run just above atmospheric pressure, except the VD, which operates

Table 3

Operational properties of the four gas subsystems in CLEO II. Shown are the volume in litres, operating pressure in atmospheres, the influx of fresh gas, recirculation flow, the leak rate in l/min, the number of detector volume changes per day, and the oxygen level at the detector exhaust

System	Volume [l]	Pressure [atm]	Fresh [l/min]	Recirc [l/min]	Leaks [l/min]	Volumes per Day	O <sub>2</sub> [ppm]
MU	9000	1.005	2.1	9.5	1.5	1.5	260
DR	5100	1.005	2.4	8.2	0.3	2.3	40
VD	60	1.379	0.37	-	0.18	8.9	< 15
PTL	8	1.005	0.21	-	< 0.01	38.0	< 15

at 1.38 atm (20PSIA). The pressures are maintained separately in each system by a proportional valve (PV) connected in a feedback loop with a pressure transducer (see fig. 19 as an example of one system). If the pressure dips below (goes above) a preset value, the PV closes (opens) slightly until the desired pressure is attained. The DR and MU systems each have a 300 l in-line buffer tank between the transducer and PV to stabilize the pressure oscillations. The PTL system does not use such a valve; its output gas is vented directly through a few mm of oil to the exhaust. Oil-filled bubblers act as emergency pressure relief at the input and output of the DR, MU, and PTL detectors. These bubblers are set slightly above and below the respective operating pressures. There must be protection against both positive and negative pressures because of the presence of the in-line recirculation pumps (for DR and MU) and a master exhaust line, which because it is vented by a fan to the air, sits below atmospheric pressure. The VD is protected by mechanical relief valves at input and output.

The DR and MU are both large volume detectors needing flows of at least one volume change per day. The cost of gas precludes such flows if the all chamber exhaust gas is vented to air. Hence the gas in each of these systems is recirculated. Recirculation allows setting the flow through the detectors independently of the influx of fresh gas, but also requires removing the oxygen that diffuses into the system through leaks. Nitrogen, of course, also accumulates to a limited extent but does not adversely affect the ionization process or chamber lifetime as does a high concentration of oxygen. Fig. 19 shows a schematic of the DR recirculation system. Flow around the recirculation loop

is maintained by an MFC. Just in front of the MFC is a 1300 l buffer tank at 6 PSIG. That pressure is set by a mechanical backpressure regulator, which, if the pressure exceeds the setting, sends excess gas out of the loop. Fresh gas is sent into the loop at 2.4 l/min, much smaller than the recirculation flow of 8.2 l/min. The recirculation pump is located just after the PV at the chamber exhaust, and is followed by the purifier.

The gas purifier removes oxygen, large molecules, and particulates in the stream. A small flow of hydrogen is injected into the gas just upstream of an in-line palladium catalytic converter; the hydrogen and oxygen in the passive catalyst combine to form water. The gas then passes through molecular sieve material, composed of a synthetic crystalline alumina-silicate with its waters of hydration removed, which adsorbs all water vapour passing through up to 25% of its weight. When the sieve becomes saturated it can be recycled off-line by baking for a few hours at 300°C while flushing with argon. After the sieve, a 10- $\mu$ m in-line filter removes any remaining dust in the stream.

Oxygen levels are monitored at the output of each detector, as summarized in table 3. In addition, there is an oxygen probe just after the palladium catalyst in the purifier. Flow of hydrogen into the purifier is adjusted to keep this oxygen level small (< 25 ppm).

Gas enters the DR volume through eight holes in the endplates, four on each end of the chamber in its upper half near the outer radius. Gas exits the chamber through eight holes in the lower half of the chamber, located symmetrically with the entrance holes.

Analogously, the MU gas system recirculates and purifies its own flow. The "fresh" gas at the MU input is actually the exhaust from the DR loop; the exhaust

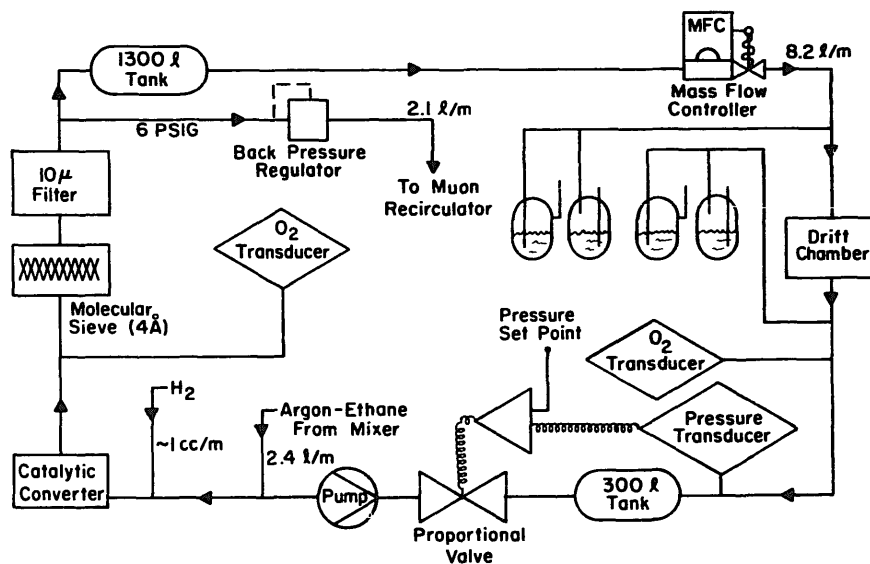


Fig. 19. DR gas recirculation system.

from the MU loop is vented to air. A total of 9.4 l/m flows from the 1000 l buffer tank which is regulated at 5 PSIG. The flow is then distributed to ten parallel streams, one for each barrel octant and one for each endcap. Each of those ten streams is again distributed in parallel to about ten routes, one per layer in the octant/endcap; counters in each layer are connected in series. Each such parallel stream is protected against over- and under-pressure with bubblers to air. Each octant/endcap is periodically checked for leaks by switching in-line a pair of mass flow transducers and comparing measured input and output flows.

The gas composition is periodically monitored at a number of points by a gas analyzer which measures the gas density (relative to argon) via its thermal conductivity. The relative flows in the gas mixer are calibrated by comparing the mixed gas to a "standard" reference gas, commercially prepared to be  $(50.0 \pm 0.1)\%$  ethane with the balance argon. The ethane fraction is maintained to a stability of  $\pm 0.1\%$ .

Part of the input gas to the VD and PTL systems is passed over a water reservoir prior to reaching the chamber (20% of the flow for the VD and 10% for the PTL). Presence of water vapour in drift chamber gas has been shown to have palliative effects on wire currents and chamber lifetimes in a high radiation environment [12].

### 3.7. Momentum and angular resolution

Momentum resolution can be parameterized to have two components: one from the error in measurement of the curvature of a track due to individual measurement errors in drift distances; the other from the distortion of the track from a true helix due to multiple scattering. Thus, we expect to resolve momentum (perpendicular to the magnetic field) according to the relation:

$$(\delta p_t/p_t)^2 = \left( \frac{53sp_t}{BL^2\sqrt{n}} \right)^2 + \left( \frac{0.054\sqrt{t}}{BL} \right)^2,$$

where  $s$  (in metres) is the accuracy of individual position measurements in the drift chambers,  $p_t$  is the transverse momentum in GeV/c,  $B$  is the magnetic field strength in tesla,  $L$  is the length in metres over which measurements are made,  $n$  is the number of position measurements and  $t$  is the thickness of obstructing material in the chambers in radiation lengths. The position measurement resolution,  $s$ , for the outer drift chamber is shown in fig. 20. Close to the cell edge (distance from sense wire = 1.0) the resolution is degraded because the electric field is weak and the drift path is distorted in the 1.5 T magnetic field. Along with the poor resolution, there is a loss of efficiency close to the cell edge, at a 1.5 T field, so that the

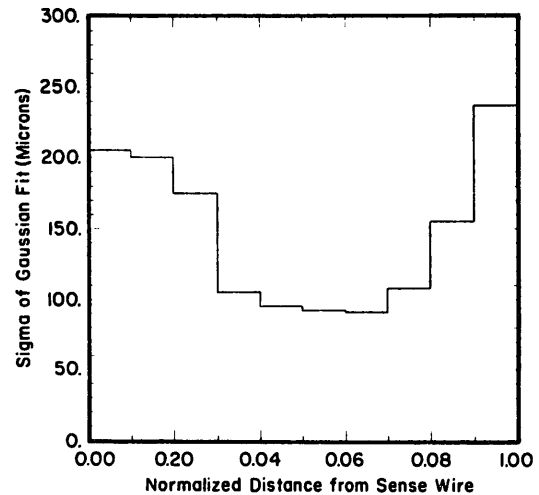


Fig. 20. Position measurement resolution vs position within the cell of the outer drift chamber. 0.0 is at the sense wire and 1.00 is at the edge of the cell ( $\sim 7$  mm from the sense wire).

average efficiency in the drift cell is only 85%. Near the wire, the resolution is limited by the spacing between primary ions in the chamber gas. The resolution observed near the wire is poorer than expected indicating the discriminator threshold is too high to be sensitive to single ions. These thresholds have not been lowered because to do so would increase the noise rate. In the central part of the cell, the resolution is relatively constant at 100  $\mu\text{m}$ . In all regions of the cell the resolution is actually somewhat worse than is shown in fig. 20 because there are non-Gaussian tails in the distribution of measurement errors. This degrades the expected momentum resolution either by increasing the position measurement resolution,  $s$ , used in the equation above or, reducing the number of position measurements,  $n$ , by not using hits which disagree with the fit.

The scattering material in the central detector is listed in table 2. In the active region the total material has a thickness of 0.0247 radiation lengths. Note that a substantial portion of this material, 0.0108 radiation lengths, lies at the interface between the intermediate and outer drift chambers. A kink is allowed at the radius of this interface in fitting the tracks to minimize the effect of the concentration of material. Using the formula given above with  $B = 1.5$  T,  $L = 0.85$  m,  $n = 49$ ,  $s = 150$   $\mu\text{m}$ , and  $t = 0.025$  r.l. the expected resolution becomes

$$(\delta p_t/p_t)^2 = (0.0011p_t)^2 + (0.0067)^2,$$

which leads to  $\delta p_t = 47$  MeV/c at  $p_t = 5.280$  GeV/c. This is slightly lower than the measured resolution of 64 MeV/c shown in fig. 21.

Understanding the resolution of the azimuthal and polar angle calculated from the reconstructed track is

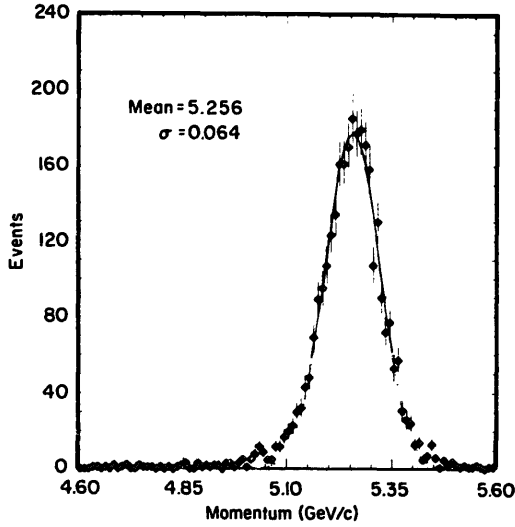


Fig. 21. Measured momentum of muons from the reaction  $e^+e^- \rightarrow \mu^+\mu^-$  at 5.280 GeV beam energy.

important for estimating event reconstruction efficiencies. Our current understanding of these resolutions is based on a sample of  $e^+e^- \rightarrow \mu^+\mu^-$  events, which provides an estimate at high momentum (5.0 GeV/c). The rms measured resolutions are

$$\delta\phi = 1 \text{ mrad}; \delta\theta = 4 \text{ mrad}.$$

The difference between the azimuthal and polar angular resolution is expected because there are only 15 measurements in the polar direction: 11 from stereo wire layers in the outer drift chamber, and four from cathode readout layers. The stereo wire layers, with a longitudinal position resolution of from 3 to 5 mm depending on stereo angle, and the cathode readout layers, with resolution about 1.8 mm combine to give a polar angle resolution of 0.003 rad. However, the angular resolutions depend on the track curvature (the particle momentum) and empirical testing of the momentum dependence would be useful. Once the momentum resolution is understood, angular resolution can be inferred using the width of the two pion mass spectrum from the decay:  $K^0 \rightarrow \pi^+\pi^-$ . This analysis is still in progress.

Angular acceptance for particles that are of sufficient momentum to not curl inside the outer drift chamber is limited by the number of longitudinal direction measuring layers at small radius. Requiring four longitudinal measurements (for redundancy and to allow for imperfect efficiency) limits the acceptance to  $0.92 \times 4\pi$  (see table 2). This can be improved to 96% by loosening the redundancy requirement and using the radius at which the track exits the outer drift chamber as a polar angle measurement. Low momentum particle acceptance is important for the detection of many decays of the B meson. It is also important for separating exclusive channels from background.

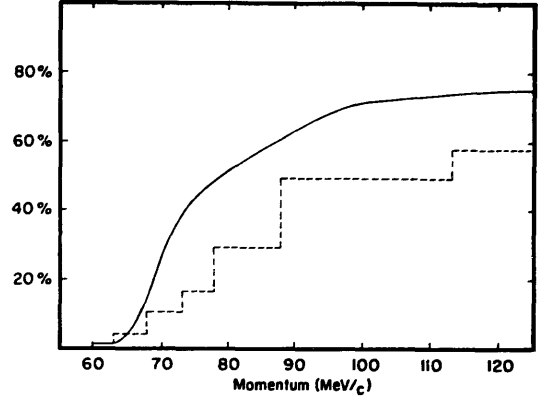


Fig. 22. Track reconstruction efficiency at low momentum calculated from Monte Carlo simulation of a pion in the drift chambers with a magnetic field of 1.5 T. The solid curve is for the single isolated tracks. The dashed histogram, is the result after embedding the same set of pion tracks in a real data sample of hadronic events recorded at the T(4S).

Charged particles are not detected below a momentum of 65 MeV/c due to the material in the particle path. The acceptance is further reduced by overlaps with other tracks, and as in the case of higher momentum, by the limited number of longitudinal measuring layers at low radius so that the efficiency rises above 65 MeV/c reaching 50% at 100 MeV/c as shown in fig. 22.

### 3.8. Charged particle identification by specific ionization

Particles have been identified in CLEO II by measuring the specific ionization energy loss ( $dE/dx$ ) in the 51 layers of the main drift chamber. Fig. 23 shows  $dE/dx$  vs momentum for hadronic tracks. Because of the large Landau tail of the ionization distribution, we take, as the best estimator of  $dE/dx$ , the 50% trun-

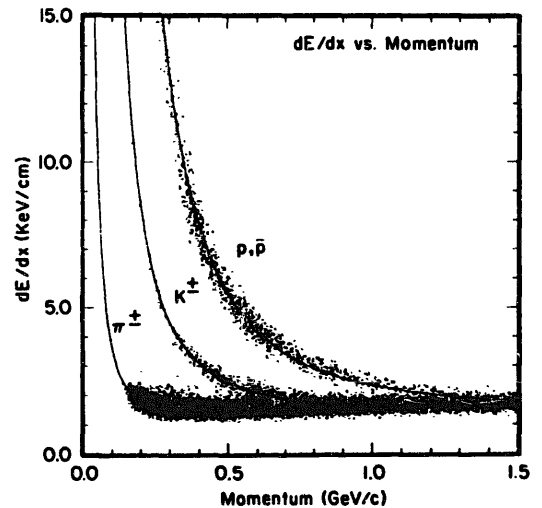


Fig. 23. Specific ionization vs track momentum for hadrons.

cated mean [13]. In order to obtain optimum resolution, the raw data must be corrected for the following effects.

a) Dip angle saturation. When a track is produced in a direction that is perpendicular to the sense wires, there is the highest density of ionization along the  $z$  direction. This causes electric shielding which effectively reduces the gain (thus the collected charge) for each hit on that track. Therefore the measured charge depends on the polar angle of the track, with the largest effect at angles close to  $90^\circ$ .

b) Drift distance. The amount of charge reaching the wire within the gate time depends on the distance the electrons have to drift from the track to the wire. This depends on the electric field shape within the cell, and in part on the magnetic field strength through the  $E \times B$  effect.

c) Entrance angle. The drift distance distribution depends on the magnitude of the entrance angle of the track, in the  $(r, \phi)$  plane, into the cell. We have found there is also a dependence on the sign of the entrance angle due to the  $E \times B$  effect.

d) Axial-stereo layer. Again, due to different electric field shapes of axial and stereo cells, the drift distance distribution depends on the type of layer.

All of these dependencies have been measured and a five-dimensional, 1600 bin map has been produced which is used to correct the charge associated with each hit on a track. For a track with 40 or more good hits, a resolution of 6.2% has been achieved for Bhabha tracks, while for minimum ionizing pions, we get 7.1%.

## 4. The time-of-flight system

### 4.1. Introduction

The time-of-flight (TOF) system in the CLEO II Detector is used as a primary trigger for data recording (the trigger system is described in section 7), and as a tool for particle identification. The momentum of a charged particle is measured from the track curvature in the drift chamber. Measuring the “time” to reach the TOF scintillation counter allows constraint on the particle mass which enables particle identification.

There are two major parts of the TOF system, the barrel and the endcap. The barrel counters cover the polar angles from  $36^\circ$  to  $144^\circ$ , while the endcap counters extend from about  $15^\circ$  to  $36^\circ$  on the west side and from  $144^\circ$  to  $165^\circ$  on the east. The solid angle subtended by the barrel counters is about 81% of  $4\pi$  and that by the endcap counters is 16%. Below, we present descriptions of the barrel and endcap counters and summarize the current status of the measured time resolutions.

### 4.2. Barrel time-of-flight counters

There are 64 barrel counters located immediately outside of the central drift chamber and fastened by straps to the inside surface of the crystal container. Fig. 24 shows a drawing of a barrel counter. The thickness of 5 cm was chosen to maximize the thickness without harming the performance of the cesium iodide calorimeter. Bicron BC-408 scintillator was chosen for the fast decay time (2.1 ns) and long attenuation length (2.5 m). At each end of the scintillator there is attached a light pipe made of UVT lucite with a  $17^\circ$  bend. The light pipe was formed with the proper angle by using heat lamps to warm the lucite and bending the light pipe in a precisely constructed jig. The scintillator and the light pipes are glued together with HE 17017 epoxy obtained from Hartel Plastics. This epoxy forms a very strong bond with good light transmission. At the phototube end of the light pipe, there is a short UVT lucite transition piece from the end of the light pipe to the cylindrical photomultiplier tube. The joints between the light pipe and the transition piece and the photomultiplier are made with Hexel Epolite 5313. This epoxy was chosen for its optical quality, constant properties over long times, and strong joint which can be broken with a sharp knife to allow replacement of the photomultiplier tube. The counters were wrapped first with aluminum foil and subsequently with black tape.

The photomultiplier tubes are a slight modification of the Amperex 2020. The photocathode is somewhat different with a higher quantum efficiency. The accelerator electrode is not connected internally to dynode 5, but is connected to a spare pin so that its voltage can

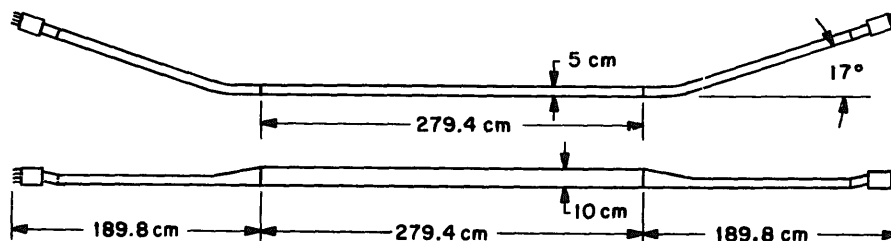


Fig. 24. Barrel time-of-flight counter.



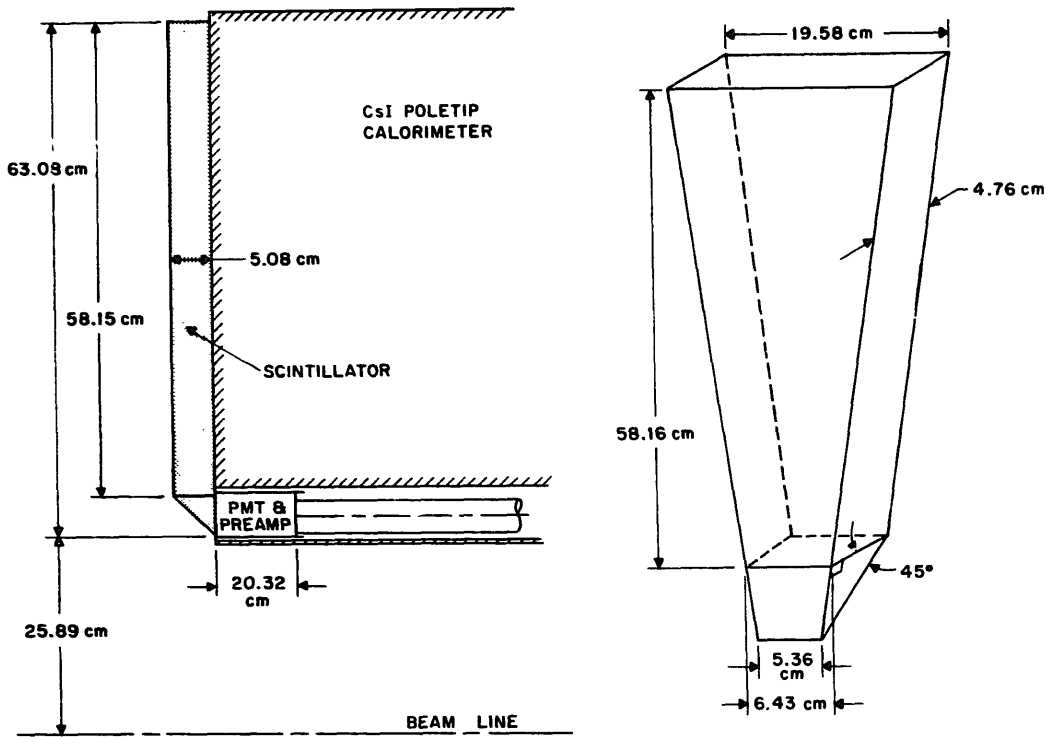


Fig. 26. (a) Side view of an endcap TOF counter mounted on the endcap calorimeter. (b) Design of the endcap TOF scintillator.

R2490 tubes were tested by placing them in an experimental test setup with a 1.5 T magnetic field parallel to the tube axis. We found the gain reduction varies from 70 in the best case to about 250 in the worst case, for an operating voltage of 2400 V, which is typically about 200 V above the plateau shoulder. In the same series of tests, we found no evidence of timing resolution degradation due to the magnetic field. The gain reduction is compensated by a fast, high gain preamplifier at the photomultiplier tube output. Its circuit diagram is shown in fig. 29 and is based on the Signetics wideband high frequency amplifier NE5205. The amplifier gain used in laboratory tests was 50 and saturated at an output of about 5 V. Inside CLEO II, the photomultiplier outputs were fed by RG58/U coaxial cables to amplifier cards mounted on the outside face of the solenoidal pole tips and the amplifier gains were reduced to about 15. All 56 endcap counters were tested in a laboratory bench setup at an operating voltage of 2400 V with the preamplifier. The r.m.s. timing resolution varied from 120 ps in the best case to 250 ps in the worst case, the average value being about 170 ps.

4.4. Readout electronics

The data acquisition cards for the time-of-flight system were designed and constructed at Harvard. For each photomultiplier signal there are two time to pulse height converters and a circuit for recording the integrated charge in the pulse. For each of the time

channels there is a discriminator which determines the point on the input pulse at which the time measurement is started. The stop signal for the time measurement is derived from the rf frequency of CESR and is

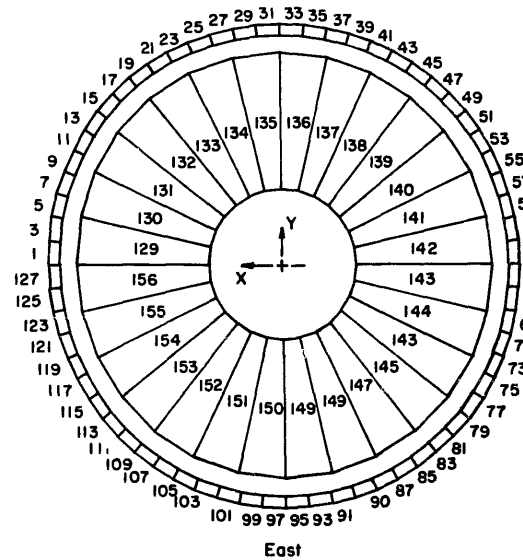


Fig. 27. Rear view of the east endcap TOF counters on the face of the CsI poletip calorimeter, and the relative location of the barrel counters. The numbers shown are the phototube addresses. The 64 barrel counters each have two phototubes; the tubes on the east side are odd integer; those on the west side of the same counter have an address number one larger. West endcap phototubes are addressed 157 through 184.

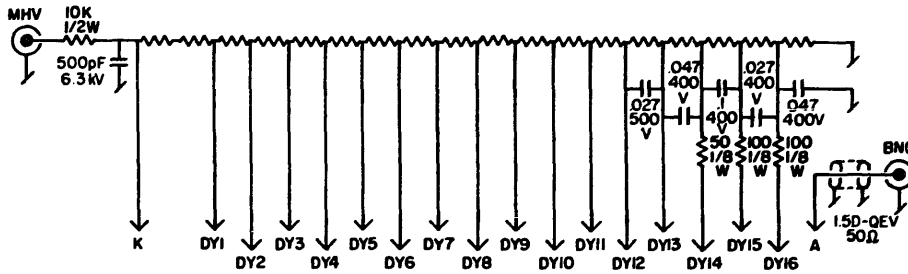


Fig. 28. Circuit diagram of the base assembly for the Hamamatsu R2490 photomultiplier tube. Unless otherwise specified, all capacitors are in  $\mu\text{F}$ , and the resistors are 470 k $\Omega$ , 1 W.

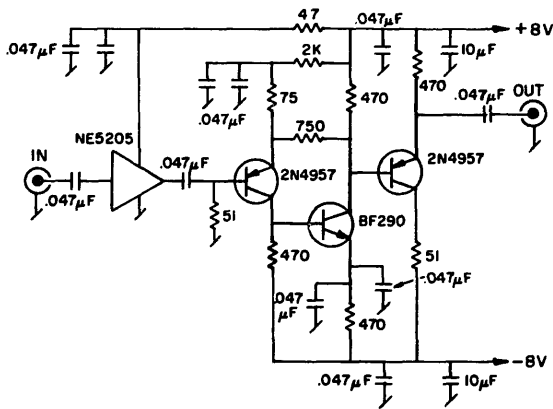


Fig. 29. Circuit diagram of the fast preamplifier.

ers with a time constant of 2  $\mu\text{s}$ . The discriminator thresholds are 40 and 80 mV, and phototube high voltages are set so that a minimum ionizing particle produces a 400 mV pulse. Upon receipt of a suitable trigger, the analog signals of time and pulse height measurements are stored using sample and hold circuitry and read out by the crate controllers. A programmed pulse generator is used to calibrate the electronic circuits. The signals are recorded as a function of the delay of the pulse and the data are analyzed to determine the pedestal and time-(TDC counts) relation for each electronic channel.

directly related to the time at which the beams collide. (The CLEO II timing system, which provides the stop signal is described in section 7.) The two discriminators are set to separate threshold levels so a measurement of the two times can be used to correct for the rise time of the photomultiplier pulse. There is no reset for the primary storage capacitor and each channel recov-

#### 4.5. Calibrating the TOF system

Bhabha events are used to calibrate the system. Events are selected for which there is only one hit in a counter and the momentum and trajectory are used to calculate the time-of-flight. Let  $T_{mij}$  represent the time calculated from TDC counts for phototube  $i$  for event  $j$ . The calculation is based on electronic calibration constants. The time measured by a phototube is com-

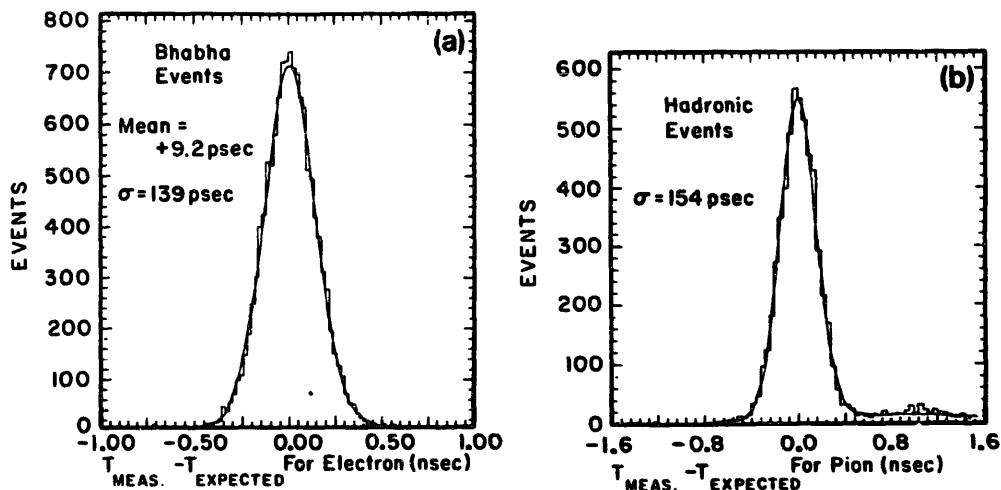


Fig. 30. Time resolution obtained with the barrel time-of-flight counters: (a) for Bhabhas; and (b) for pions in hadronic events.

pared to the expected time,  $T_{ij}$ , which is given by an expression of the form

$$T_{ij} = T_{0j} + T_i + L_j/v_i + K_i/Q_j^n$$

Here  $T_{0j}$  is the calculated time for the electron to move from the interaction point to the scintillator,  $T_i$  is a time offset constant for each channel,  $L_j$  is the distance from the point where the electron crosses the scintillator to the end of the scintillator,  $v_i$  is the velocity of signal propagation in the scintillator,  $Q_j$  is the measured pulse height in ADC counts, and  $K_i$  and  $n$  are parameters which depend on pulse shape and the time slewing in the discriminator. For each photomultiplier tube  $T_i$ ,  $v_i$ , and  $K_i$  were taken as free parameters and the best values determined by minimizing the difference between  $T_{mij}$  and  $T_{ij}$  with the Bhabha data. For initial studies,  $n$  was set to 0.5. It was subsequently varied and with  $n = 0.15$ , the time resolution improved by 5 ps. For the barrel counters, there are two phototubes on each scintillator and initially the fitting was done using the same effective velocity of the light signal for both phototubes. It was found that the resolution improved 25 ps by allowing each phototube to have an independent velocity parameter. The resolution obtained for Bhabhas is 139 ps. Fig. 30a shows a plot of the time resolution for an independent sample of Bhabha events not used in the calibration. A plot of the time resolution on pions from hadronic events is shown in fig. 30b, where momentum is required to be less than 0.7 GeV/c. The high side tail is due to kaons, and a two-Gaussian fit gives a time resolution of 154 ps, rms, for pions. This resolution provides a  $2\sigma$  separation for pions and kaons of 1.07 GeV/c momentum. Similar results were obtained for both low and high threshold discriminator channels. The two channels will be used to extrapolate to zero pulse height for counters where there are two hits in a counter and therefore both phototubes of the counter can not be used for the same particle, or when the pulse height ADCs overflow. Ref. [14] describes the test program used to develop the barrel time-of-flight counters. The test gave an average resolution of 110–120 ps. Recent studies suggest that the difference between the test resolutions and that obtained in the CLEO II detector may be partially due to variations between the rf-derived stop signal and the true time of the bunch crossings. The Barrel TOF counters already provide significant information for particle identification. The separation of hadrons is illustrated in fig. 31 where  $1/\beta$  derived from the TOF counters is plotted as a function of track momentum for a set of hadronic events recorded at the T(4S).

The readout electronics for the endcap TOF counters is the same as that used for the barrel counters and a similar calibration procedure using Bhabha events has been implemented. The counters were oper-

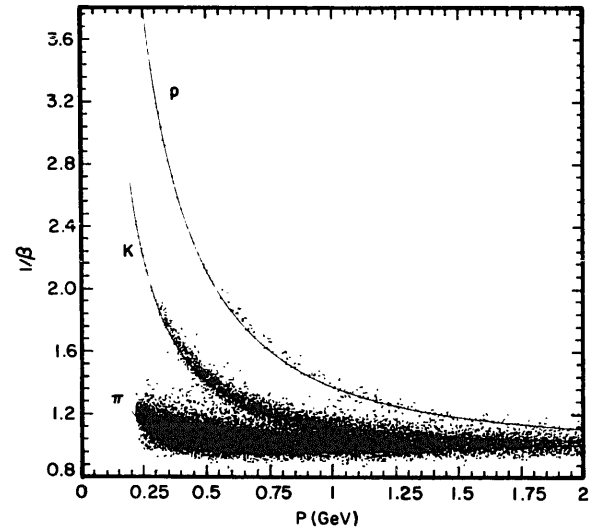


Fig. 31.  $1/\beta$  ( $\beta = v/c$ ) versus track momentum measured in the drift chambers for a sample of hadrons in the barrel TOF counters.

ated at a voltage between 2200 and 2400 V. The time difference distribution between the measured and expected times from a sample of Bhabha events not used in the calibration resulted in a timing resolution of about 272 ps, which is not as good as the average of 170 ps from bench tests. Calibrating the endcap time-of-flight counters is more difficult than the barrel. Since there is only one phototube per counter, one can not study position dependent correlations. Furthermore, using Bhabha events introduces a complicated spread in the timing caused by electromagnetic showers initiated in the drift chamber endplate, where one of the electrons from the shower enters the scintillator at a significantly closer distance to the phototube than the primary electron. The result presented here on the endcap time resolution is preliminary and calibration of the endcap counters is still under study.

## 5. The electromagnetic calorimeter

### 5.1. Introduction

The CLEO II calorimeter consists of 7800 thallium-doped cesium iodide (CsI) crystals. A number of previous publications [15–18] have explored the suitability of such a detector and associated readout schemes. For the CLEO II application (in which a highly segmented, large-volume shower detector at a 1 m radius in a 1.5 T field must make precision measurements on photons from 15–5000 MeV) thallium-doped cesium iodide has been shown [16] to be technically superior and more cost-effective when compared to alternatives, such as NaI, BGO, BaF<sub>2</sub>, or lead glass.



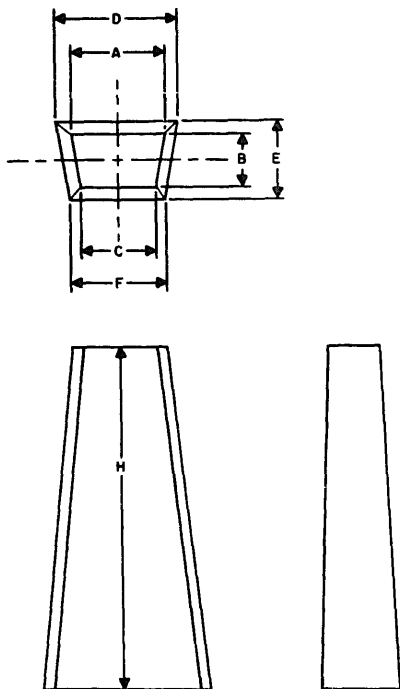


Fig. 32. Definition of the dimensional parameters determining crystal size and shape.

tween crystals, which degrades energy resolution, is kept to a minimum. The holder, consisting entirely of aluminum components, is shown in fig. 33. It has cylindrical inner and outer walls, capped by a cover annulus at each end, and surrounds an internal lattice of 64 longitudinal fins (separating every other crystal in azimuth) and 13 lateral rows of fins (separating every fourth row in  $z$ ). The fins provide the necessary rigidity and separate the CsI blocks into snugly packed  $2 \times 4$ -block pockets. The holder is 3.37 m long and its inner wall has a radius of 1.024 m and a thickness of 1.59 mm; the fins are 0.51 mm thick. An outer skin of radius 142.5 cm consisting of eight panels, each 6.35

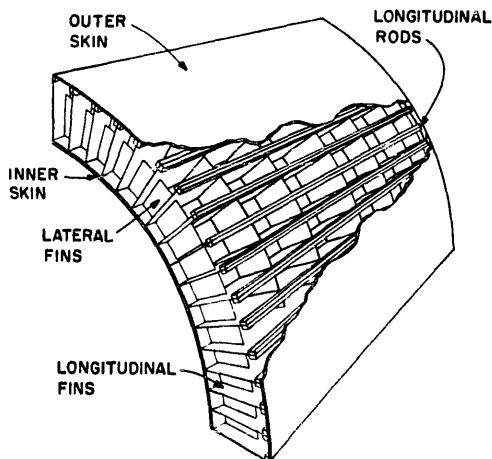


Fig. 33. A portion of the barrel crystal holder.

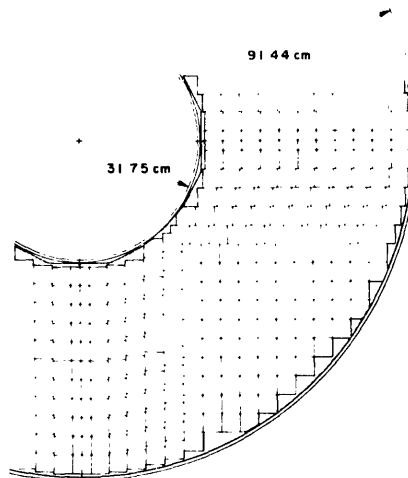


Fig. 34. A quadrant of an endcap crystal holder showing location of the endcap crystals.

mm thick and covering the full barrel length, closes the structure. The barrel holder was built on a steel inner mandrel that provided strength while loading the crystals into the pockets and transporting the completed unit. The mandrel and barrel holder were rolled into place on a central rail and the whole unit lowered slightly to rest on the inner wall of the cryostat of the superconducting coil. The mandrel was then reduced in diameter and rolled back out.

Each endcap holds 828 crystals stacked inside a cylindrical holder, as shown in fig. 34, so that the maximal amount of area near the outer radius is covered by CsI. All endcap blocks are rectangular (see table 4). The arrangement of crystals in each endcap is four-fold symmetric; the same pattern of 207 crystals is repeated, rotated by  $90^\circ$  each time. The aluminum holder has inner and outer cylindrical walls capped by circular cover plates. The inner and outer wall radii (thicknesses) are 0.321 m (6.35 mm) and 0.914 m (9.53 mm), respectively, and the front cover plate is 6.35 mm thick. Each front plate is located 1.248 m from the interaction point.

Preamplifier boards are mounted directly behind the crystals. Cables, light fibres, and cooling tubes pass through the end covers in the barrel and near the outer radius of the endcaps. All joints, rivets, and openings in the crystal holders were covered with sealant; nitrogen flows through each holder to keep the CsI dry. The on-line computer routinely and automatically checks temperature and humidity monitoring stations (eight in the barrel and three in each endcap) to verify that the cooling and drying systems are working properly. The temperature is maintained at  $(28 \pm 2)^\circ\text{C}$ , and the humidity at less than 1%. The barrel and endcap holder dimensions allow for a tolerance of  $\pm 0.1$  mm on the crystal lateral dimensions, and for a total of 0.13 mm of wrapping around each block.

Calorimeter performance varies considerably with polar angle because the energy response is degraded by the material present in support structures and readout electronics for the tracking chambers. The central barrel region, which covers 71% of the solid angle ( $45^\circ < \theta < 135^\circ$ ), has the smallest amount of material in front of it. Material close to the CsI crystals reduces energy resolution only by photon conversion and absorbing the electron energy via ionization, whereas material far in front of the crystals introduces a much greater effect because the energy is dispersed over a broad region. The total material between the beam line and the first wire layer of the main drift chamber is 2.5% radiation lengths. The argon-ethane gas and the 51 wire layers contribute another 0.4% (see table 2 for more details). The nearby material consists of the outer cathode layer, 1% r.l.; outer wall, 2% r.l.; and the TOF counters, 12% r.l. A larger amount of material exists between the interaction point and each endcap. The drift chamber endplate is 3.18 cm of aluminum, and the cables, readout boards mounted on the endplate, support bars, and a copper cooling plate (3 mm thick) mounted just in front of the endcap TOF add substantially to the material. Below  $25^\circ$  the vertex detector endplate and cables block the path as well. The barrel-endcap transition region ( $32^\circ < \theta < 36^\circ$ ) is blocked by drift chamber supports and the outer wall of the endcap holder, and has inadequate CsI in depth to contain high energy showers.

Neighbouring blocks in the barrel are staggered longitudinally with respect to each other by a distance which varies with polar angle from zero at  $90^\circ$  to 9 cm at  $35^\circ$ , as shown in fig. 2. Staggering has been shown [16] to deteriorate energy resolution near crystal boundaries by a small but measurable amount; the shower can leak out the sides and rear of the staggered crystals. Such effects are significant only near the ends of the barrel where the staggering is large. The effect is reduced by the non-vertex pointing geometry.

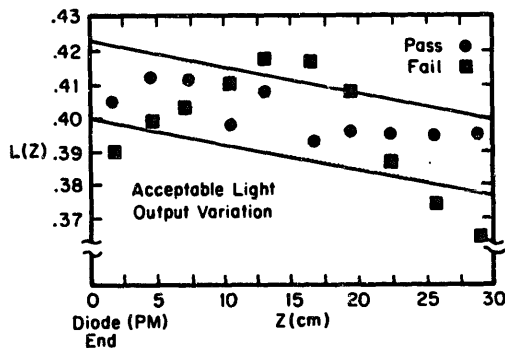


Fig. 35. An example of the specification for crystal gradient; two crystals with the same  $G_z$  but different scatter in the light output are shown. One passes the specification and one fails.

### 5.3. Crystal acquisition and evaluation

After a lengthy initial evaluation [16] of thallium-doped CsI crystals from four manufacturers [24], two were chosen, each to provide half the CLEO II crystals. The specifications demanded high absolute light output, uniformity in response along the length of the crystal, strict adherence to dimensional tolerances (see table 4), absence of visible defects such as bubbles, cracks, or cloudiness, and no crystal fluorescence after exposure to fluorescent light. By supplying manufacturers with measurement tools similar to those developed for CLEO II, evaluation of these criteria for every crystal became a routine and reproducible task. The manufacturers wrapped each block in three layers of 0.04 mm white Teflon followed by 0.01 mm aluminized Mylar, assuring high internal reflection and light-tightness of each crystal.

Light output characteristics were measured [16] by exposing each crystal at ten positions along its length to 662 keV photons from a collimated  $\text{Cs}^{137}$  source and reading out the light with a green-sensitive Amperex XP1017 photomultiplier. The signal from the 662 KeV line was compared to the same line measured with the same phototube, but using a small "standard" CsI block. The crystal specification required the average light output,  $L_a$ , to exceed 20% of that obtained with the small "standard" CsI block. The longitudinal gradient,  $G_z$ , defined as the relative change in light output from the front to rear end of the crystal from a linear fit to the light output, typically lies between  $-1$  and  $+11\%$ . The actual specification required that at most one of the ten light output measurements could lie outside a band centred on the value of  $L_a$ , as shown in fig. 35. Such a positive gradient, as compared to zero, does not hurt energy resolution at low energy and improves it above 1 GeV: the increased light output at the back of the crystal partially compensates for fluctuations in rear shower leakage which dominate the resolution at high energies. Both light output and gradient depend crucially upon the purity of the crystal-growing materials, the clarity of the resulting block, surface preparation, and wrapping. The  $L_a$  and  $G_z$  values for all crystals are shown in fig. 36.

### 5.4. Crystal readout

Four silicon photodiodes mounted on a 6 mm thick UVT lucite window on the rear face of each crystal convert the scintillation light from the CsI into electrical signals. For redundancy, each of the photodiodes is connected to an independent nearby preamplifier. The cable from the preamplifier travels outside the CLEO II detector to the mixer/shaper card, which sums the four preamplifier signals from each crystal and shapes

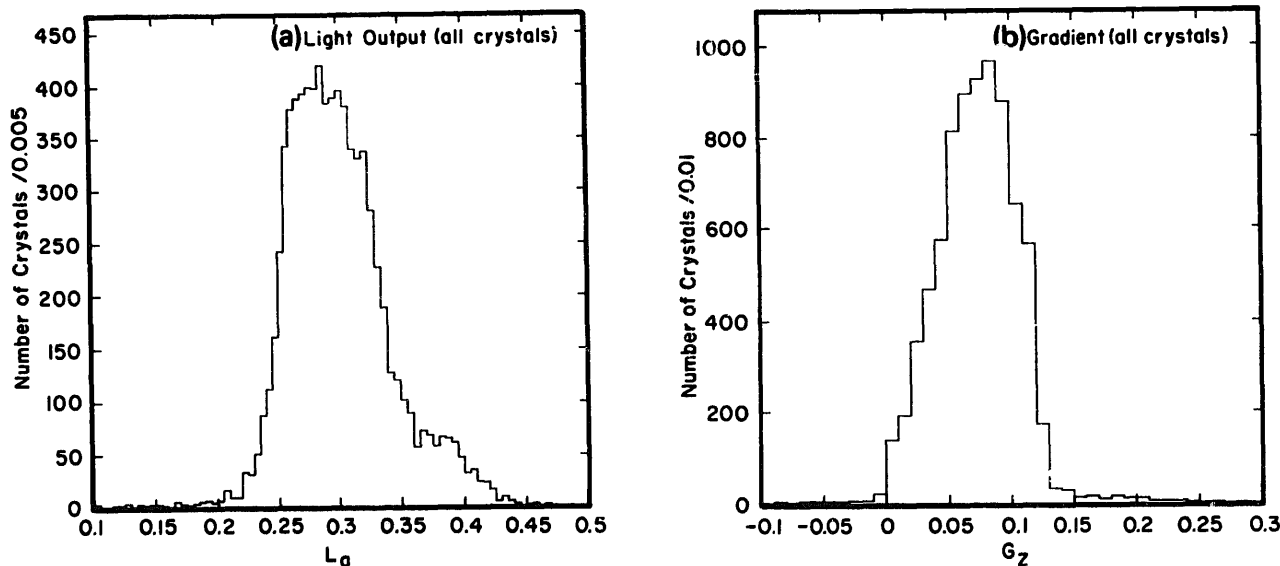


Fig. 36. Distributions: (a) average light output  $L_a$  and (b) gradient  $G_z$  from source measurements of all crystals in CLEO II. Crystals with  $L_a < 0.2$  and  $G_z > 0.15$  are from early orders and were placed near the inner radius of the endcap.

the signal for input to the ADC. Fig. 37 shows the time structure of the pulses at each stage of readout.

The Hamamatsu S1723-0j photodiode [16–18] has an active area of  $1 \times 1 \text{ cm}^2$ . When a reverse bias voltage of 10 V is applied, each diode has low leakage current (typically 1 nA) and a junction capacitance of 75 pF. Early diode failures from increased surface leakage currents were traced to the epoxy coating, and Hamamatsu subsequently eliminated this problem. The manufacturer checked the production orders by baking at  $80^\circ\text{C}$  for two days and passing those diodes with low leakage currents ( $< 5 \text{ nA}$  at 20 V and  $25^\circ\text{C}$ ). After delivery, diodes were operated for one week at 20 V and  $25^\circ\text{C}$ , and those with high currents were discarded.

A schematic of the charge preamplifier is shown in fig. 38. It features hybrid implementation, a single +15 V power supply, differential noise immunity to output cable pickup, a rise time of 15 ns, and fall time of 180  $\mu\text{s}$ . The rise time of a pulse from the calorimeter is dominated by the 900 ns decay time of the CsI(Tl). Noise referred to the input is about 250 electrons without the photodiode connected. With a diode connected the noise is approximately 600 electrons rms. Under computer control, charge may be injected at each channel's input to calibrate electronic gain and linearity. Preamplifiers are arranged in groups of 16 per board, servicing diodes on four neighbouring crystals. Each board dissipates 3 W of power, so copper tubes, in thermal contact with a copper case surrounding each board assembly, are used to circulate freon for cooling. The FET is the most likely component to fail (see fig. 38). The manufacturer thermally cycled the preamps ten times between  $-40^\circ\text{C}$  and  $+140^\circ\text{C}$  and operated them at  $85^\circ\text{C}$  for two days, rejecting any failures. The circuits were tested again after delivery.

The mixer/shaper first sums the four signals per crystal. It has a pole-zero shaper to eliminate the long tail of the preamp pulse and has a circuit to drive twisted-pair cables to the ADCs. The circuit diagram is shown in fig. 39. The rise time is 2  $\mu\text{s}$  and fall time is 9  $\mu\text{s}$ ; fig. 37 shows the pulse shape. A fine gain adjustment is available to compensate with about 5% accuracy for crystal-to-crystal variations in light output for triggering purposes. Each input is computer-addressable to select the preamp/diode channels to be used for each crystal and simultaneously adjust the gain to account for any of the input channels turned off. The cards reside in one of the 24-card crates specifically designed for the CLEO II calorimeter. There are a total of twenty four mixer-shaper crates, 16 for the

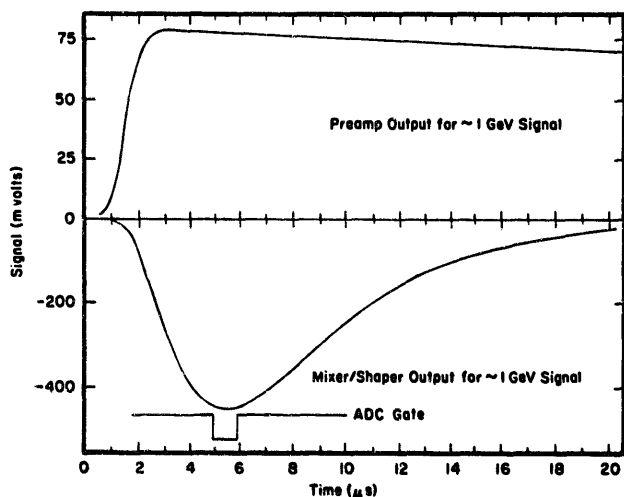


Fig. 37. Pulse shapes at output of the preamps, and mixer/shaper circuits, and sampling gate for the ADC.

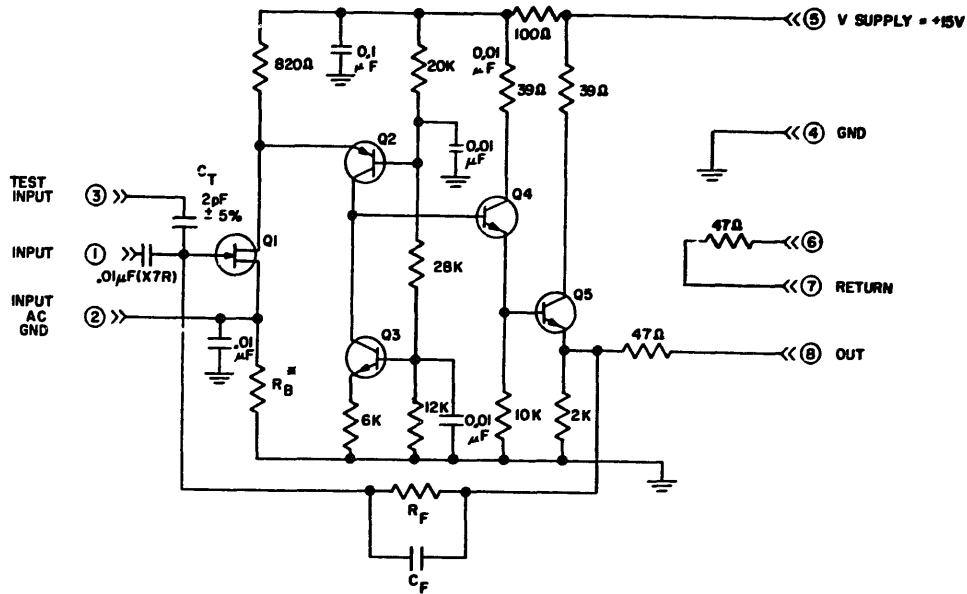


Fig. 38. Circuit diagram of the CLEO II hybrid charge sensitive preamplifier for crystal readout connected to the silicon photodiode.  $R_F = 100 \text{ M}\Omega \pm 5\%$ ,  $C_F = 1 \text{ pF} \pm 5\%$ ,  $R_B^*$  to be trimmed for FET ( $0.6 \text{ k}\Omega \leq R_B \leq 1.2 \text{ k}\Omega$ ).

barrel and four for each endcap. After the gain variations have been equalized but before shaping for the ADC, the analog signals from the 16 crystals on each mixer/shaper card are differentiated and summed together for trigger purposes. The resultant 16-crystal sum is fed to two on-board discriminators, set at 100 and 500 MeV respectively, which then act as input bits to the trigger system (section 7).

LeCroy Fastbus model 1885N ADCs, with 96 channels per card, digitize the analog pulse for readout into

the data acquisition system. The signal from the mixer/shaper is attenuated by a factor of 20 at the ADC, filtered with a 10 kHz high pass filter, and integrated with a 1- $\mu$ s gate as shown in fig. 37. The digitized output has 12 bits of precision and an extra bit indicating high or low range. High and low range differ in gain by a factor of eight, so these modules have an effective 15 bit dynamic range. The ADCs are operated in auto-range mode in which the ADC itself automatically chooses the appropriate gain for the

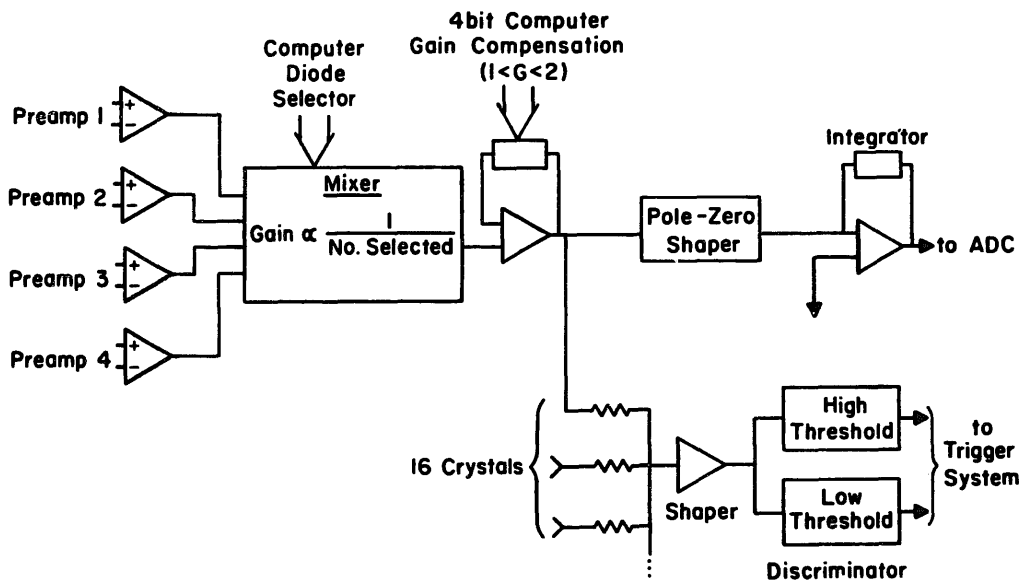


Fig. 39. Schematic of the mixer/shaper circuits between the crystal preamplifiers and the ADCs.

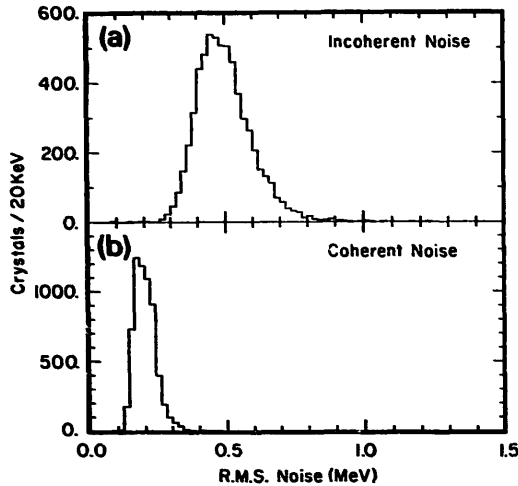


Fig. 40. RMS noise levels in individual crystals, as broken down between (a) the incoherent and (b) coherent contributions.

signal present at the input. Four Fastbus crates, with 21 ADC slots filled per crate, house the ADC cards for CLEO II.

The electronic noise in the system can be given in ADC counts (or equivalent MeV) and can be broken down into coherent and incoherent contributions. The incoherent contributions from a group of summed crystals combine in quadrature, whereas the coherent ones add linearly. The primary source of incoherent noise is Schottky noise from the photodiode leakage currents, whereas the coherent contribution is primarily in the ADC module. These noise levels can be measured by the width of individual and summed crystals when there is no true energy signal present, such as during a pedestal calibration with no beams in CESR. The distributions of the rms pedestal values from a no-beam calibration are shown in fig. 40. The average values are 0.5 MeV incoherent (2.3 ADC counts) and 0.2 MeV coherent (0.9 ADC counts); most channels have less than 1 MeV incoherent and 0.5 MeV coherent noise levels.

The hardware components performing the sparsification of the ADC's output data is described in section 7. The algorithm selects for readout into the computer the address and ADC value of all crystals that are located within two blocks of any deposition  $> 6$  MeV, and is more than a standard deviation above pedestal.

More precisely, a crystal's data is saved as part of the event if it is both a) above pedestal by two or more counts, and b) one of the crystals in the  $5 \times 5$  block array centred around a crystal which is 25 or more counts above pedestal. This results in approximately 430 crystal digitizations written to tape on a typical hadronic event.

The failure rate of the crystal readout components is an important figure of merit for performance, especially for the diodes and preamplifiers inside the detector because they cannot be repaired without disassembling CLEO II. Diodes fail by exhibiting large leakage currents and hence a high noise level. Preamplifiers fail by yielding almost no signal or an erratic one. Fortunately, because the cables from all four diode/preamplifier combinations on each crystal are brought outside the crystal holder, those diodes (or preamplifiers) that fail can be deactivated in the mixer/shaper circuit. Crystals can operate adequately even with only one live diode/preamplifier combination, though the incoherent electronic noise relative to the signal is a factor of two smaller with all four channels alive. Of the total 31200 diode/preamp channels in CLEO II, 108 were found to be faulty or disconnected after assembly of the calorimeter. In a subsequent 13 month period of operation, from February 1990 until March 1991, 35 preamplifiers and 9 diodes failed, and 6 mixer/shaper cards and 2 ADC boards were replaced due to malfunctions. At this rate, it should require in excess of 19 years before one crystal has only one live diode/preamp, and more than 69 years until one crystal has all four of its channels dead.

### 5.5. Light flasher calibration system

A light flasher system monitors changes in the calibration of the photodiodes and the crystals (electronic pulser calibration monitors the components downstream of the diodes). The goal of the system is to detect if the light-sensitive gain changes more than 0.5% on a day-to-day basis. The schematic of the system is shown in fig. 41. Light fibres transmit the flasher pulses from a flash tube to the readout end of each crystal. The light then reflects off the crystal surfaces and is collected by the photodiodes.

Two EG and G FX280 xenon flash tubes each serve 3900 crystals (an endcap and half of the barrel each).

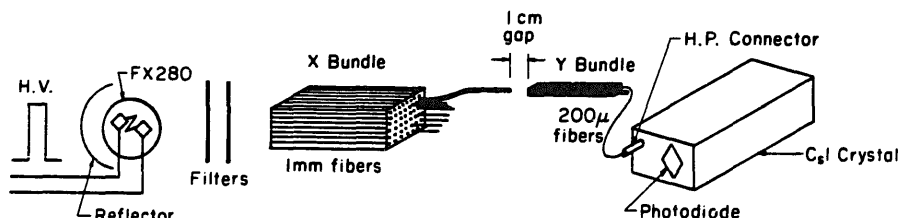


Fig. 41. Schematic of the light flasher system.

There is a parabolic mirror behind each of the flash tubes. Pieces of green and white plastic are placed in the 5 cm gap between the tube and 1-mm fibre bundles in order to match the light spectrum to that of CsI scintillation light, and to diffuse the light so that all the fibres are illuminated more uniformly. There are 156 1-mm diameter PCS (plastic clad silica) fibres grouped in six bundles at the flash tube end. Each of these 1mm fibres then connects to a bundle of 50 PCS fibres, each 200  $\mu\text{m}$  in diameter. In turn these thin fibres transmit light to individual crystals. There is a 1 cm gap between each pair of mating 1 mm fibres and 200  $\mu\text{m}$  fibre bundles. This ensures that all the 200  $\mu\text{m}$  fibres are illuminated uniformly. The 200  $\mu\text{m}$  fibres are connected to the back of the crystals, where the photodiodes are mounted, using Hewlett Packard snap-in connectors HFBR 4001/4005.

The intensity of the light pulses changes too much from pulse to pulse and from one day to the next to monitor small changes in the absolute gain of each crystal. Therefore, only the gain change of a crystal relative to its "neighbours" is monitored (those crystals flashed by the same bundle of 200  $\mu\text{m}$  fibres are defined as the neighbours). Since the fluctuation of the relative pulse heights is typically 1% (3% for absolute normalization), the statistical accuracy of a 25-pulse measurement is 0.2% for each crystal. The flasher system has been useful in detecting failed diodes and swapped cables. When one of the four diodes on a crystal fails, it is obvious that a large change ( $> 10\%$ ) in the flasher calibration has occurred, whereas the electronic calibration might only show a subtle increase in pedestal width in such a case. There has also been an occurrence of swapped cables that went undetected until the flasher data indicated the problem. This latter problem is easier to detect with the flasher system because the optical characteristics vary from one crystal to the next more than the electronic gains.

### 5.6. Clustering and calibration

The ADC values in the raw data banks are converted into energies before shower reconstruction begins. This requires electronic pedestal subtraction, gain multiplication appropriate to the run being analyzed, and conversion to absolute energy units. Periodic pulsing of the electronics monitors changes in the pedestals, gains, and noise in the readout system, which can be due to slow drifts in the electronics or different properties of replaced mixer/shaper or ADC modules. Crystal-to-crystal calibrations, normalized for beam energy electrons, are calculated using  $e^+e^- \rightarrow e^+e^-$  events. These constants are computed by minimizing the rms width of the Bhabha electron shower energy distribution and constraining it to peak at the beam energy; this requires solving a linear equation involving a 7800

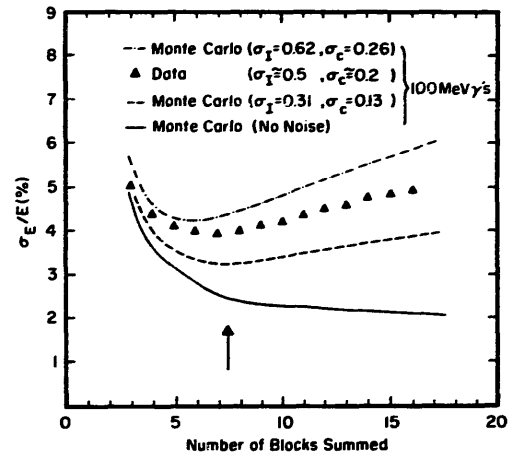


Fig. 42.  $\sigma_E/E$  as a function of the number of highest- $N$  crystals summed. The curves were generated from Monte Carlo shower simulation of 100 MeV photons with appropriate noise included. The points were measured with real data, the 100 MeV photon lines at the T(3S). The arrow indicates the actual number summed in the CLEO II cluster algorithm for 100 MeV photons.

$\times 7800$  sparse matrix. In principle, these constants can be obtained accurate to  $\pm 0.5\%$  for every crystal in a  $30 \text{ pb}^{-1}$  dataset ( $< 1$  week of running at current CESR luminosities). In practice, the crystal constants change slowly with time and need to be updated only every few months.

Reconstruction of calorimeter showers begins with the formation of clusters from individual crystal hits. The most energetic crystal in any cluster is the only cluster member exceeding 10 MeV to have higher energy than any of its immediate neighbours. Each member of a cluster is physically located at most two blocks away from another member of the same cluster.

The energy and position of each cluster are computed from its most energetic  $N$  crystals, where  $N$  varies logarithmically with the total cluster energy from 4 at 25 MeV to 17 at 4 GeV ( $N = 4$  below 25 MeV and  $N = 17$  above 4 GeV). These values [25] of  $N$  minimize the energy resolution, as shown in fig. 42, which would otherwise be degraded further by electronic noise. This algorithm yields better energy resolution than other possible methods, such as summing a fixed number of crystals near the highest, or summing all neighbouring crystals over some threshold. It does so by selecting crystals with the largest energy deposition and rejecting those most likely to be dominated by noise (i.e. the smallest), and includes the right number of crystals as a function of energy. In a small percentage of cases a crystal may belong to two clusters, in which case its energy is apportioned between them. The absolute calibration correction described below is then applied to the cluster energy to yield the best estimate of the energy of the incident particle assuming it to be a photon.

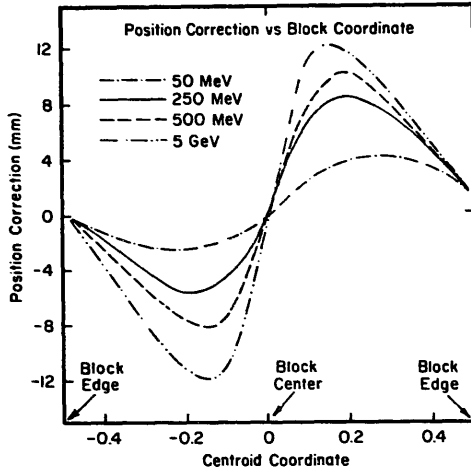


Fig. 43. Lateral correction in azimuth as a function of block centroid coordinate for various energies. A positive centroid coordinate is at larger azimuth angle than the block centre. The curves are not perfectly anti-symmetric about the block centre because the crystals are systematically tilted to point away from the beam line.

The position vector of each cluster is computed in two steps. First, the centroid is calculated as the energy-weighted sum of the coordinates of each crystal's geometric centre. Then a correction vector is added to the centroid. The correction has two pieces, a lateral component correcting the shower location in the plane perpendicular to the incident particle's direction, and a longitudinal piece which adjusts the depth into CsI of the shower centre. Both components depend on cluster energy. The lateral correction varies with the proximity of the centroid to the edges of a block. The lateral correction, which is only applied to barrel clusters (where particles strike a nearly rectangular array of crystals at normal incidence), is small near the centre and edge of a block, and moves the centroid away from the block centre in between [16] as shown in fig. 43. The longitudinal correction places the shower at the depth within the CsI where an electromagnetic shower would have its mean energy deposition. This depth can be calculated analytically for CsI as a function of the shower energy  $E$  as

$$\text{Depth [cm]} = 5.45 + 0.97 \ln(E[\text{MeV}])$$

which varies from 10 cm at 100 MeV to 14 cm at 5 GeV. Assigning the correct shower depth is important for matching showers to charged track trajectories projected into the calorimeter, and in the endcaps to assign the polar angle correctly.

Absolute energy normalization for photon clusters requires a number of techniques to cover the entire photon energy range. Such normalization accounts for the difference between photons and electrons at 5 GeV and the effects of shower leakage, crystal gradients, and the cluster algorithm, all of which vary with

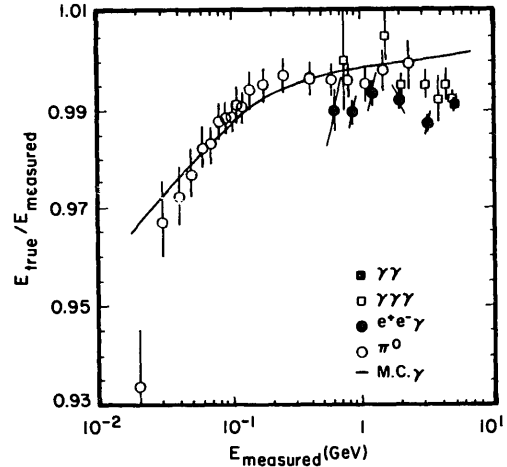


Fig. 44. The correction factor  $E_{\text{true}}/E_{\text{measured}}$  for absolute photon energy calibration, measured using different techniques.

photon energy. Such a calibration has only been performed so far for showers in the region  $45^\circ < \theta < 135^\circ$ , and is summarized in fig. 44. Photon pairs from  $\pi^0$  decays, constrained to the expected mass, yield a calibration accurate to about  $\pm 0.5\%$  below 2 GeV. Above 500 MeV, photon energies in radiative Bhabha events are compared to the constrained value obtained from the measured momenta of the electron and positron, yielding calibrations accurate at the  $\pm 0.5\%$  level. Similarly, radiative  $\gamma\gamma$  events (with three photons observed

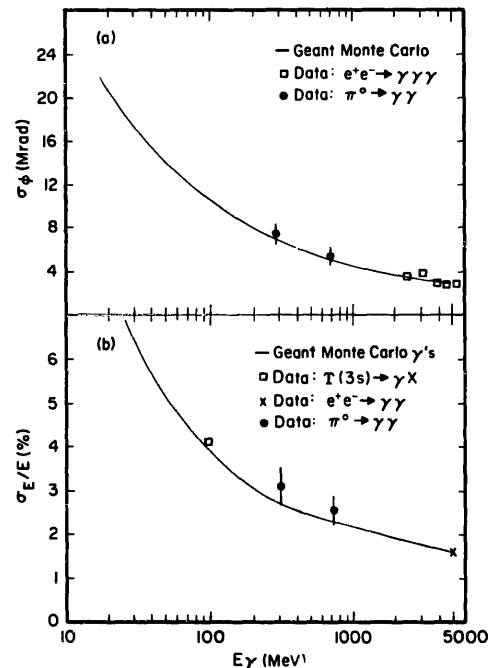


Fig. 45. (a) Azimuthal angle resolution of the calorimeter as a function of photon energy. (b) Shower energy resolution of the calorimeter as a function of photon energy.

in the detector) can be used for photon energies above 700 MeV, using energy-momentum conservation and the measured angles; the result is also accurate to about  $\pm 0.5\%$ . Final states with two back-to-back photons provide an accurate normalization at the beam energy. Finally, Monte Carlo shower simulation [26] can be used as a cross-check. Within the quoted errors, all these techniques are consistent where they overlap, yielding an absolute calibration accurate to  $\pm 1\%$  at 25 MeV,  $\pm 0.5\%$  at 100 MeV, and  $\pm 0.2\%$  at 5 GeV. The errors relevant for determining energy differences of nearby photon lines [27] are much smaller because the variation of the absolute calibration with energy is gradual.

The calibration procedures described above have maintained an absolute run-to-run gain stability of better than  $\pm 0.25\%$  as monitored by measured Bhabha energies and  $\pi^0$  masses over time. There is no observed angular dependence within the barrel of the absolute energy calibration; i.e. the energy-dependent correction is identical for  $45^\circ < \theta < 135^\circ$ .

### 5.7. Performance of the calorimeter

With these calibrations the CLEO II calorimeter has performed superbly. Figs. 45a and 45b show the angular and energy resolutions, respectively, defined as  $\text{FWHM}/2.36$  of the relevant distributions (which are non-Gaussian and asymmetric). Photon energy resolution in the barrel (endcap) is 1.5% (2.6%) at 5 GeV, and 3.8% (5.0%) at 100 MeV. Barrel (endcap) angular resolution in azimuth is 3 mrad (9 mrad) at 5 GeV and 11 mrad (19 mrad) at 100 MeV. The energy resolution can be parametrized as

$$\text{Barrel: } \frac{\sigma_E}{E} [\%] = \frac{0.35}{E^{0.75}} + 1.9 - 0.1E,$$

$$\text{Endcap: } \frac{\sigma_E}{E} [\%] = \frac{0.26}{E} + 2.5,$$

while angular resolution [28] is given by

$$\text{Barrel: } \sigma_\phi [\text{mrad}] = \frac{2.8}{\sqrt{E}} + 1.9,$$

$$\sigma_\theta [\text{mrad}] = 0.8\sigma_\phi \sin(\theta),$$

$$\text{Endcap: } \sigma_\phi [\text{mrad}] = \frac{3.7}{\sqrt{E}} + 7.3,$$

$$\sigma_\theta [\text{mrad}] = \frac{1.4}{\sqrt{E}} + 5.6,$$

where the photon energy  $E$  is in GeV. These parametrizations come from Monte Carlo simulation of showering in the CLEO II detector, including electronic noise. Not included in the simulation is the modest degradation due to other particles in an event

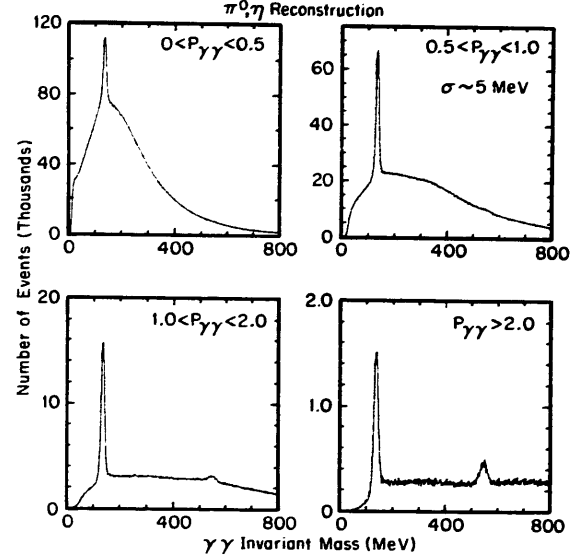


Fig. 46. Invariant mass of pairs of calorimeter showers unmatched to charged tracks in four  $\gamma\gamma$  momentum ranges (from a data sample of hadronic events at the T(3S)).

and beam-related energy overlapping with the photon clusters. These effects vary with event topology and CESR operating conditions. The endcap resolutions quoted are tentative and are the subject of further study. The barrel resolutions measured in CLEO II data are also shown in fig. 45 and are consistent with the predictions. Barrel energy resolution at 100 MeV measured with inclusive T(3S) decays [27] is  $(4.2 \pm 0.2)\%$  and at 5 GeV measured with  $e^+e^- \rightarrow \gamma\gamma$  events is  $(1.5 \pm 0.1)\%$ . The 100 MeV resolution compares favourably with that obtained by CUSB [29] (4.8%) and Crystal Ball [30] (4.8%). Angular resolution consistent with Monte Carlo is measured with  $e^+e^- \rightarrow \gamma\gamma\gamma$  events above 2 GeV. The  $\pi^0$  mass width depends on both the energy and angular resolution of its component photons and is consistent with the Monte Carlo predictions.

In part, the power of CLEO II lies in its ability to implement precision reconstruction of decays involving photons. Many of such decays involve intermediate  $\pi^0$ s or  $\eta$ s, which decay into two photons. Fig. 46 shows the invariant mass of pairs of showers not matched to the projections of charged tracks. The  $\pi^0$  peak is evident in all four momentum bins plotted, and the  $\eta$  peak appears above 1 GeV/c. The rms width of the  $\pi^0$  peaks is approximately 5 MeV, which is dominated by energy resolution at low momenta and angular resolution at high momenta. Much can be done, depending on the application, to improve  $\pi^0$  (and  $\eta$ )  $\rightarrow \gamma\gamma$  reconstruction beyond what has been done here, including, for example, cuts on the lateral shower shape and decay angle. A photon detection efficiency of 50% in the barrel calorimeter can be obtained,

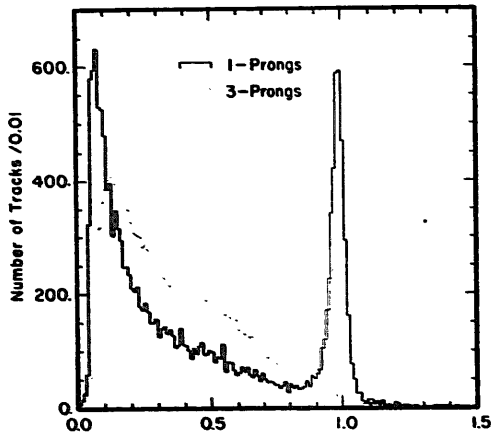


Fig. 47. The ratio of shower energy to momentum  $E/p$  for tracks in events in the one-vs-three charged-track topology, a sample rich in  $\tau$ -pairs. The one-prong side tracks, shown in the solid histogram, are normalized to the same number of entries as the three-prong side tracks (dotted). The expected electron peak is evident at  $E/p = 1$  for the loner track.

compared with 10% for CUSB [29] and 15% for Crystal Ball [30]. The fine segmentation allows the separation of individual photon showers from  $\pi^0$  decay up to  $\pi^0$  energies of 2.5 GeV, above which energy the showers sometimes merge. Merged-shower  $\pi^0$ s can be distinguished from single photons by their larger lateral shower spread.

The calorimeter energy can be used in conjunction with the momentum and  $dE/dx$  from the tracking chambers for electron identification. By utilizing the ratio of shower energy to momentum ( $E/p$ ), lateral shower shape, difference between the projected track position and the shower location, and specific ionization in the drift chamber gas, powerful hadron rejection (several hundred to one) is achieved while maintaining a high efficiency ( $> 90\%$ ). By far, the most powerful of these is  $E/p$ . Fig. 47 shows the ratio of shower energy to track momentum for events in the one-vs-three topology, a sample rich in  $\tau$ -pairs. For the 1-prong side, there is clear evidence for the expected electron peak near unity, in contrast to the 3-prong side, which shows no enhancement.

Data have been acquired with a random trigger under normal colliding beam conditions. These data yield identical results for the rms pedestal width as the no-beam pedestal calibrations, but do show evidence for occasional beam associated showers. For example, there is typically a shower in 1/10 random events in each of the polar angular ranges

$$(0.87 < |\cos \theta| < 0.94), (0.71 < |\cos \theta| < 0.87), \\ (|\cos \theta| < 0.71).$$

These beam related showers have energy distributions as shown in fig. 48. Approximately 1/5 of those show-

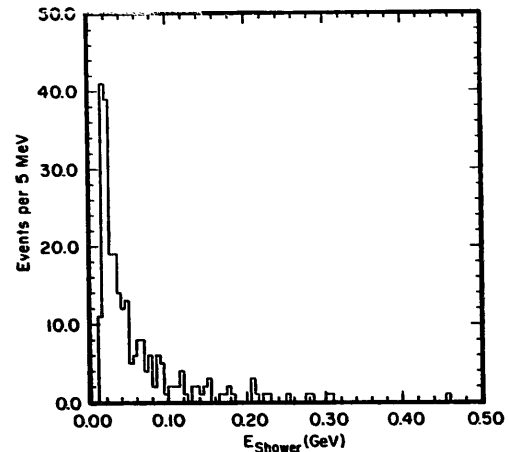


Fig. 48. Distribution of largest shower energy per event in the barrel from a random trigger run under normal colliding beam conditions. The bin with 0 to 10 MeV energy, which contains 90% of all events, is suppressed because a “shower cluster” must contain at least one crystal with energy greater than 10 MeV.

ers have energy above 50 MeV, and 1/10 above 100 MeV. Such showers are present at low angles in the endcaps ( $< 20^\circ$ ) in about half of the events, and have an energy distribution similar to that of the barrel. The rate of such extra showers in both barrel and endcap, however, strongly depends on CESR beam conditions, and has been observed to be considerably higher for certain run periods. No evidence for radiation damage yet exists, even for those crystals most at risk near the inner endcap radius. Inner endcap crystals have been exposed to a dose of 100 rad, and with calibrations based on vertical cosmic rays, show less than 5% degradation in light output since installation. Other crystals have been exposed to far less radiation, and also show no measurable decrease in light output.

## 6. The muon identification system

### 6.1. Description of the hardware

The muon identification system for CLEO II was designed with the goals of maximum solid angle coverage, high efficiency, low probability of a hadron being misidentified as a muon (fake rate), reliability and ease of operation. Because of space limitations the muon chambers only cover the polar angle range  $30^\circ$  to  $150^\circ$ , which is 85% of the total solid angle. Here we present a brief description of the system and a summary of performance level. A more detailed account of its construction and performance can be found in a separate paper [31]. Barrel muon chambers are embedded in an iron absorber at depths of 36, 72 and 108 cm of iron (see fig. 1). Additional muon chambers (endcaps)

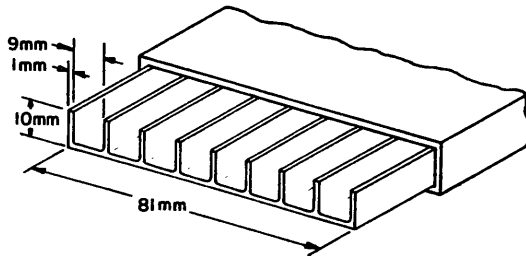


Fig. 49. Cross section of a plastic proportional tube in the muon detector.

cover the two ends of the detector. The total equivalent thickness of iron absorber varies from about 7.2 to 10 nuclear absorption lengths ( $\lambda_i = 16.8$  cm in iron [32]), depending on the direction of the track.

Ease of operation is obtained by using “plastic streamer counters” [33], operating in the proportional mode, at 2500 V with a 50:50 argon–ethane mixture. The counters are about 5 m long and 8.3 cm wide. The cross section of a counter is shown in fig. 49. The eight anodes in each counter are 50  $\mu\text{m}$  diameter silver-plated Cu–Be wires. They are ganged together, giving an rms space resolution per counter of 2.4 cm, which is better than the spatial uncertainty due to multiple scattering at the momenta of interest in our experiment. The comb-like plastic profile [34] is coated with graphite to provide a cathode on three sides of each anode. One hit coordinate is obtained by reading out the anode signal, while the orthogonal coordinate (along the counter) is measured with external copper pickup strips, of the same width as the counters. The argon–ethane gas mixture is provided by the gas system developed for the central drift chamber, described in section 3.

In order to achieve high efficiency, we have instrumented each iron gap and the exterior of the iron absorber with “units”, each composed of three layers of 20, 25, 29, or 24 counters, depending on the unit location (see table 5). Each layer has readout of the orthogonal coordinates. The reason for having three layers is the following: two slightly staggered layers are needed to eliminate the geometrical inefficiency of a single layer, and the third layer provides redundancy in case of malfunctioning of some counters. Furthermore

the use of appropriate logical combinations of hits in the three layers allows noise rejection while maintaining an adequate efficiency.

High voltage is provided by 32 computer-controlled power supplies, one for each unit. The high voltage ripple is kept below levels at which it would contribute to the pedestal width. The voltage drops at most 1% at maximum current draw. The normal current drawn by a unit is below 1  $\mu\text{A}$  and a software-controlled trip is set at 10  $\mu\text{A}$ . External high voltage distribution boxes allow disconnecting individual counters.

Charge division read-out is used to determine the two orthogonal space coordinates for each hit in the muon detector. Each layer of counters is divided into two subgroups (multiplets) of between 10 and 15 counters each (see table 5). The anode wires from each counter within a multiplet are connected via 100  $\Omega$  resistors to each neighbour and the string is connected at each end to a charge integrator via a 15–20 foot long, 50  $\Omega$  cable. In each layer the external copper pickup strips that provide the orthogonal coordinate are divided into 4 multiplets of either 9 or 15 strips each. These strips are also interconnected by 100  $\Omega$  resistors to each neighbour and the two outside strips are connected to charge integrators. In this way, signals from the 2352 counters and 5472 strips are processed by a total of 1152 charge integrators and associated electronics. In order to monitor the electronic gain stability, provision has been made to inject a fixed charge into each charge integrator from a pulser. The readout electronics is described in more detail in ref. [31].

## 6.2. Hardware performance

After the initial shakedown period (June–November, 1989), the CLEO II muon detector has performed reliably. We currently have 86 disconnected counters (out of a total of 2352) because of excessive gas leaks or broken wires. Most of these counters were found to be defective during assembling and testing the units, but too late to make replacement practical. Since the installation and shakedown period, six counters had to be disconnected because of shorted wires.

Table 5

Unit structure. The first three entries in the table refer to eight octants, each containing three Units, surrounding the magnet coil (see fig. 1). The Unit designated “Return” is at the inner most iron gap, “Inner” is at the middle gap, and “Outer” is at the outer most gap. Four end cap units are required to cover an end of the detector

Unit location	No. of units	No. of layers	Useful size [ $\text{m}^2$ ]	Multiplet counters	Structure strips
Return	8	3	$4.39 \times 1.67$	10 + 10	9 + 15 + 15 + 15
Inner	8	3	$4.87 \times 2.0$	10 + 15	15 + 15 + 15 + 15
Outer	8	3	$4.87 \times 2.42$	14 + 15	15 + 15 + 15 + 15
Endcap	8	3	$4.38 \times 2.00$	10 + 14	9 + 15 + 15 + 15

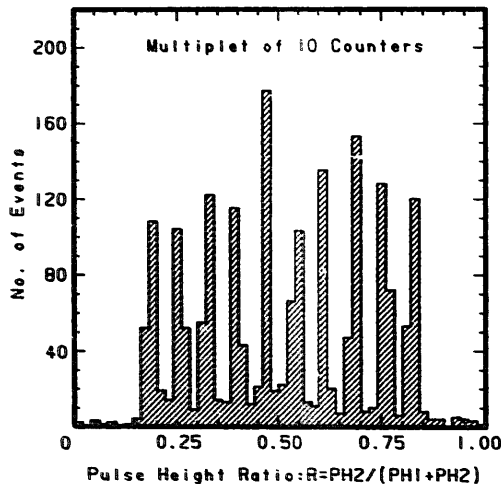


Fig. 50. Pulse height ratio distribution from charge division readout of an anode multiplet.

The electronics has also performed well. Since June 1989, we have changed only one out of a total of 24 data cards (this was to fix two channels whose pedestals were fluctuating). Calibration data is taken every two or three days to monitor pedestal mean and width stability. They have remained satisfactorily constant. During normal data recording we monitor the muon chambers on-line using cosmic rays and muon pairs produced in the  $e^+e^-$  collisions. The on-line diagnostics are designed to detect problems which affect large parts of the muon system – e.g. gas is turned off, disconnected data cards, etc.

### 6.3. Charge division calibration

The actual position of a hit (i.e. counter and strip number within a multiplet) can be determined from the ratio of pulse heights recorded at the two ends of the charge division line, which connects counters (or strips) in the multiplet. The relation between pulse height ratio and space coordinates is determined by off-line calibration. The electronic gain ratio between the two ends of each charge division multiplet are absorbed into the calibration. The pulse height ratio distributions for the anode wire readout produce clearly resolved peaks for each individual counter as illustrated in fig. 50. The distributions are therefore self-calibrating. The peaks due to individual strips in the pulse height ratio distribution are much broader and not easily resolved. The resolution of the charge division is worse in this case because of the smaller amount of charge induced on the strips compared to the wires, and there are counter-to-counter differences in the external pickup strip ratio due to slightly varying distance between the counter wires and a pickup strip. This dependence has not yet been optimally calibrated under real experimental conditions. The relation be-

tween the pulse height ratio and the space position of the hits is obtained by predicting the hit position from the muon trajectories measured in the central tracking system for  $e^+e^- \rightarrow \mu^+\mu^-$  events. The resolution thus obtained is satisfactory and the electronic system has been stable enough that the same calibration of the charge division has been used for all data collected so far.

The space resolution of the detector, defined as the rms spread in the difference between the projected track position in the layer and the hit position, is determined by three factors:

i) the propagation of the errors of the track parameters, measured in the drift chamber, when the track is projected to a unit;

ii) multiple scattering in the CsI calorimeter and in the iron absorber, important at the relatively low energies typical of our experiment, and

iii) the intrinsic space resolution of the counters and strips, i.e. the accuracy with which we can determine the space position of a counter and strip hit. The intrinsic space resolution of the counters is dominated by the width of the individual counters (rms width =  $8.3/\sqrt{12} = 2.4$  cm). For the strips the intrinsic rms width is approximately 5.3 cm. In both cases these distributions are symmetric but not Gaussian, as explained in ref. [31]. The anode space resolution, taking into account propagation of tracking errors and multiple scattering, for 5.28 GeV muons, is 3.7, 4.6 and 5.7 cm for the barrel units at successively greater iron depth, and 7.2 cm for the endcap units, reflecting the increase in multiple scattering of the tracks. The corresponding resolutions for the strips are: 5.5, 7.0, 7.5 and 9.0 cm.

### 6.4. Muon identification procedure

The first step is to extrapolate into the muon detector each track reconstructed in the central detector, taking into account  $dE/dx$  energy loss. The path length to each muon layer is calculated in terms of nuclear absorption length. Then a search is made for hits in the muon units that are likely to be traversed by the track and a two-dimensional  $\chi^2$  of the distance between the measured and the projected hit positions is calculated. If this  $\chi^2$  is less than 16, we consider that layer to be hit. Since the errors are not Gaussian, we cannot associate a confidence level to this number. It should be considered as an adjustable parameter to reach the best compromise between maximizing the muon identification efficiency and minimizing the fake probability. The track is considered as definitely detected in a unit if at least two out of the three layers in that unit are hit.

The track is assigned the depth of the outermost unit in which it is detected. If there are other units at

Table 6  
Muon identification efficiencies from  $e^+e^- \rightarrow \mu^+\mu^-$

Depth requirement	Solid angle coverage	Muon identification efficiency
$> 3\lambda_i$	$0.85 \times 4\pi$	$0.986 \pm 0.016$
$> 5\lambda_i$	$0.82 \times 4\pi$	$0.975 \pm 0.016$
$> 7\lambda_i$	$0.79 \times 4\pi$	$0.895 \pm 0.015$

greater depth that, according to track extrapolation, are expected to be hit but there are no hits in those units (i.e. if the track's depth is less than predicted) then the track is considered as a non-muon. Also, a track is considered a bad quality muon candidate if it fails to give at least one associated layer hit in each of the units along its path at a depth less than the maximal one.

6.5. Efficiency

The identification efficiency is defined as the ratio of number of muons detected by the muon system to all muon tracks reconstructed in the central detector and calorimeter. It was determined for fast muons using  $e^+e^- \rightarrow \mu^+\mu^-$  CLEO II events. This identification efficiency versus depth requirements (listed in units of nuclear interaction length,  $\lambda_i$ ) is shown in table 6 for tracks within the angular acceptance of the muon detector that satisfy the depth requirement. In fig. 51 the identification efficiency is plotted vs the cosine of the polar angle. The Monte Carlo simulation, tuned according to measured unit efficiencies during the cosmic ray test [35], reproduces the above results reasonably well and is assumed to give a good estimate of the efficiency at lower momenta. A sample of 23 000 Monte Carlo muons generated uniformly in  $\cos \theta$  and

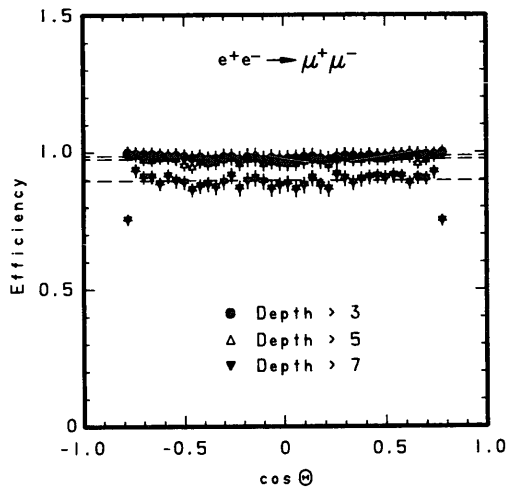


Fig. 51. Muon identification efficiency from  $e^+e^- \rightarrow \mu^+\mu^-$  events vs  $\cos \theta$ , for three different depth requirements.

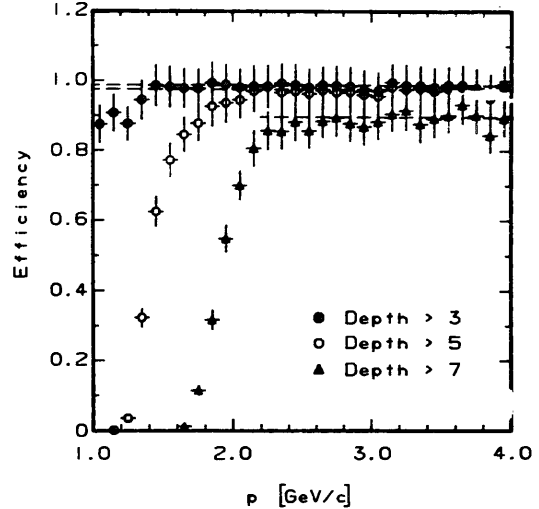


Fig. 52. Monte Carlo calculation of muon identification efficiency vs muon momentum, within the good angular acceptance regions, for the three different depth requirements:  $> 3\lambda_i$ ,  $> 5\lambda_i$ ,  $> 7\lambda_i$ .

in momentum from 0.6 to 4.0 GeV/c was used to determine the momentum dependent efficiency. The result is shown in fig. 52.

As an example of the use of the muon detector system we have looked for  $\psi$  mesons with momentum less than 2.0 GeV/c in a sample of  $491 \text{ pb}^{-1}$  taken by CLEO II at the peak of the  $\Upsilon(4S)$  resonance. Fig. 53 shows the  $\mu^+\mu^-$  invariant mass spectrum. We required one track to penetrate at least five nuclear absorption lengths, while for the other track the requirement was lowered to more than  $3 \lambda_i$ . From a Gaussian fit, we estimate the peak contains  $256 \pm 18 \psi$  mesons over a background of 32, giving a signal to background ratio of 8.

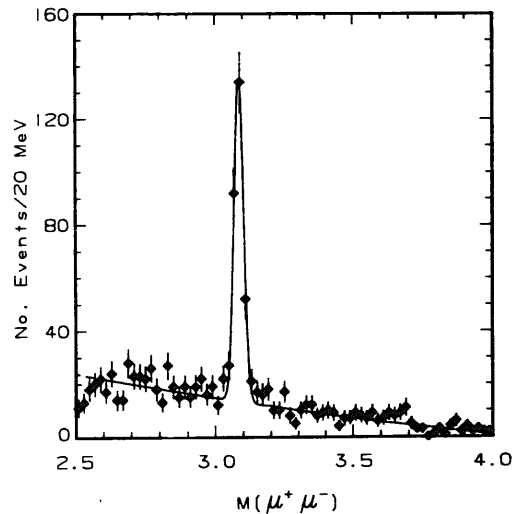


Fig. 53.  $\mu^+\mu^-$  invariant mass spectrum from CLEO II 1990-1 data at the  $\Upsilon(4S)$ .

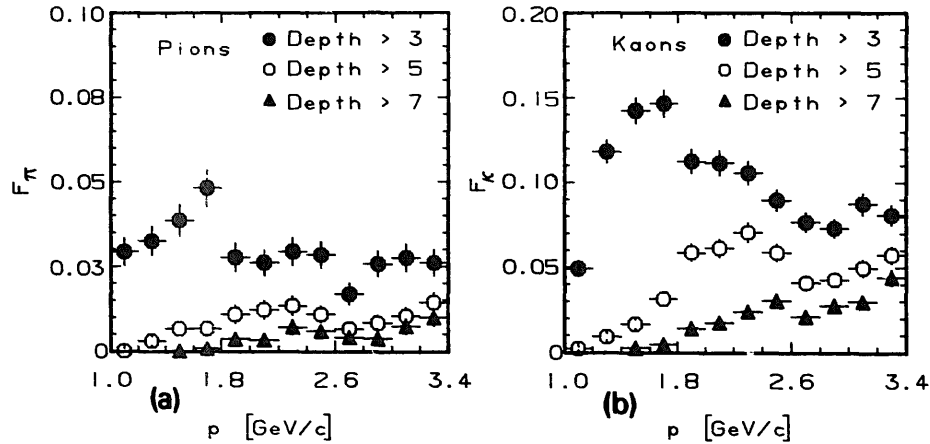


Fig. 54. Fake rate due to (a)  $\pi^\pm$  and (b)  $K^\pm$  as a function of momentum, for different depth requirements (Monte Carlo simulation).

### 6.6. Fake probability per track

The fake rate is defined here as the ratio of number of hadrons misidentified as muons (i.e. fakes) to all charged tracks within the muon detector geometrical acceptance and in a given momentum bin. The fake rates,  $F_\pi$  and  $F_k$  (due to  $\pi$  and  $K$ , respectively), for different depth requirements, determined by Monte Carlo simulation, are shown in fig. 54 as a function of the momentum of the incident hadron. The shape of the momentum dependence of the fakes rate for  $\pi$  and  $K$  are similar, but the fake probability per kaon is roughly four times higher than per pion. The momentum dependence reflects two effects:

i) the relative contributions of the different mechanisms leading to the fake muon signal change with increasing momentum and depth;

ii) with increasing momentum more information becomes available from units at greater depths, thus allowing better hadron rejection via increased nuclear absorption.

In order to verify experimentally the fake rates obtained from the Monte Carlo simulation, 370000  $K^0$ 's decaying into  $\pi^+\pi^-$  have been selected from the  $\Upsilon(4S)$  data. Keeping only  $K_s^0$  with the decay vertex at least 1 cm away from the beam line, the non  $K_s^0$  background becomes negligible. The fake rate determined this way is compared to the one produced by Monte Carlo simulation in fig. 55. The agreement is satisfactory. The excess of the fakes in the  $\pi$  sample from  $K_s^0$  decays for small momenta possibly comes from the random match of noise hits, not yet simulated by our Monte Carlo. A more extensive check of the fake rate, including fakes due to  $K^\pm$ , is underway. It

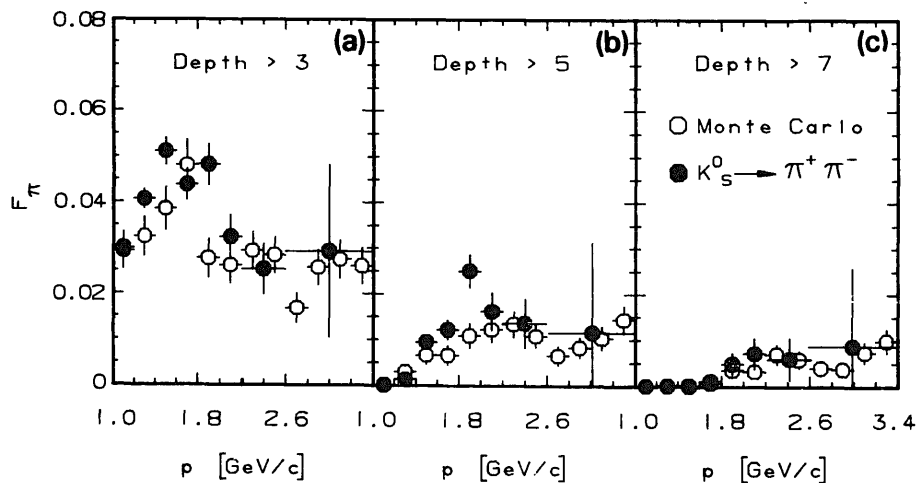


Fig. 55. Comparison between data and Monte Carlo of fake rate due to pions vs momentum for three different depth requirements. The pions are from reconstructed  $K^0$  decays.

uses  $K^-$  from the decay chain  $D^{*+} \rightarrow D^0 \pi^+ \rightarrow (K^- \pi^+) \pi^+$  and  $T(1S)$  hadronic decays and will be completed when more  $T(1S)$  data is available.

## 7. Timing, trigger and data acquisition

### 7.1. CLEO II timing system

Every colliding beam experiment needs hardware to provide gates and strobes properly timed to the crossing of the beams in the detector and to handle the enabling, disabling, and resetting the various detector elements. At CESR, keeping these signals aligned with beam in the interaction region is made more difficult by the uneven spacing of bunches in the storage ring (see fig. 56).

There are several particularly crucial timing parameters in CLEO II. The time-of-flight electronics is gated every beam crossing. The time-to-amplitude converters are started by the arrival of a pulse from the scintillators and stopped in common by the end of the gate. Given that the intrinsic resolution of the time-of-flight system is on the order of 150 ps, we need to keep the gate width and, more critically, the gate end time very stable with respect to the beam crossing time. In the drift chamber the time-to-amplitude converters are stopped by the lowest level (“L0”) trigger (see below). The investigation of the trigger is done by latching trigger inputs on the leading edge of a strobe and investigating the trigger memory outputs on the trailing edge. Again the time of the end of this strobe are critical to the experiment, since every nanosecond of jitter adds 25–50  $\mu\text{m}$  to the chamber spatial resolution. The calibration system needs a high degree of selectability in delay time and yet stability at any setting that is as good as the beam stability in CESR.

To properly match the uneven inter-arrival times of beams in the interaction region and to create strobes and gates with reproducibilities of the same quality as the beams themselves, the electronics used by the accelerator staff to inject beams into CESR was replicated for CLEO II use. The two signals sent to CLEO

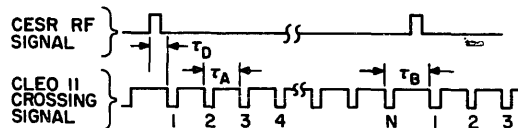


Fig. 56. Timing structure of CESR. Shown are the rf synchronization signal from CESR and the CLEO crossing signal. For  $N$  bunches of electrons and  $N$  of positrons there are  $N-1$  equal intervals  $\tau_a$  between collisions followed by one interval of length  $\tau_b$ . For  $N=3$ ,  $\tau_a = \tau_b = 854$  ns; for  $N=7$  (the present configuration)  $\tau_a = 364$  and  $\tau_b = 378$  ns. The offset  $\tau_d$  is chosen to open gates and time strobes for when the beams collide in CLEO II.

II by the CESR timing system are a copy of the overall timing start signal, which runs at 390 kHz, the revolution frequency in the storage ring; and a copy of the accelerator’s 23.8 MHz clock, derived from the rf system which operates at a frequency of 500 MHz.

Each critical signal [36] has a coarse delay circuit and a fine delay circuit [37], as shown in fig. 57. The coarse circuit delays the overall start signal by an 8-bit programmable number of 24 MHz clock cycles; i.e., the delay is 0 to 11  $\mu\text{s}$  in 42.02 ns steps. This delayed start is the input to the fine delay circuit, which has a rate multiplier to produce an internal 71.4 MHz clock. Just as shown in fig. 56, this circuit can be set to provide between 1 and 61 equally spaced outputs, followed by the appropriate gap until the start of the next train of pulses. The time of the first of this train of outputs with respect to the input signal is also programmable in 8-bits with roughly 165 ps steps.

A beam pickup monitor has been used to evaluate the performance of these fine delay circuits. Fig. 58a shows the arrival time of this pickup signal as measured in the TF timing system whose common stop is the output of such a circuit. The resolution of this signal is 30 ps. The 8-bit input to this common stop signal can be changed to check the linearity of the circuits. The deviation from such linearity is depicted in fig. 58b for various values of the setting. Both of these figures are consistent with the 50 ps stability predicted for these circuits [38].

Less-critical delays and widths are handled by 8-bit programmable delay generators (AD9500) located in a module called the sequencer; these signals are usually referenced to the L0 strobe. Examples of the signals using these generators are the start and width of the higher level trigger strobes and the closing time of the pulse height gates in the central tracking chambers.

Two of the detector systems employ digital delays (“pipelines”) in generating trigger inputs [39]. The time-of-flight system has a simple double latch scheme

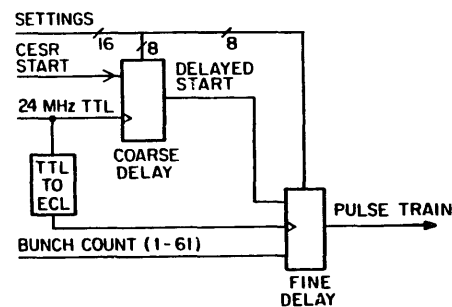


Fig. 57. Schematic of delay generation of critically timed CLEO II signals. The “CESR Start” and “24 MHz TTL clock” are provided by CESR. The experimenter chooses the 8 bits of coarse delay and 8 bits of fine delay as described in the text. The resulting train has its number of equally spaced pulses determined by the “bunch count”.

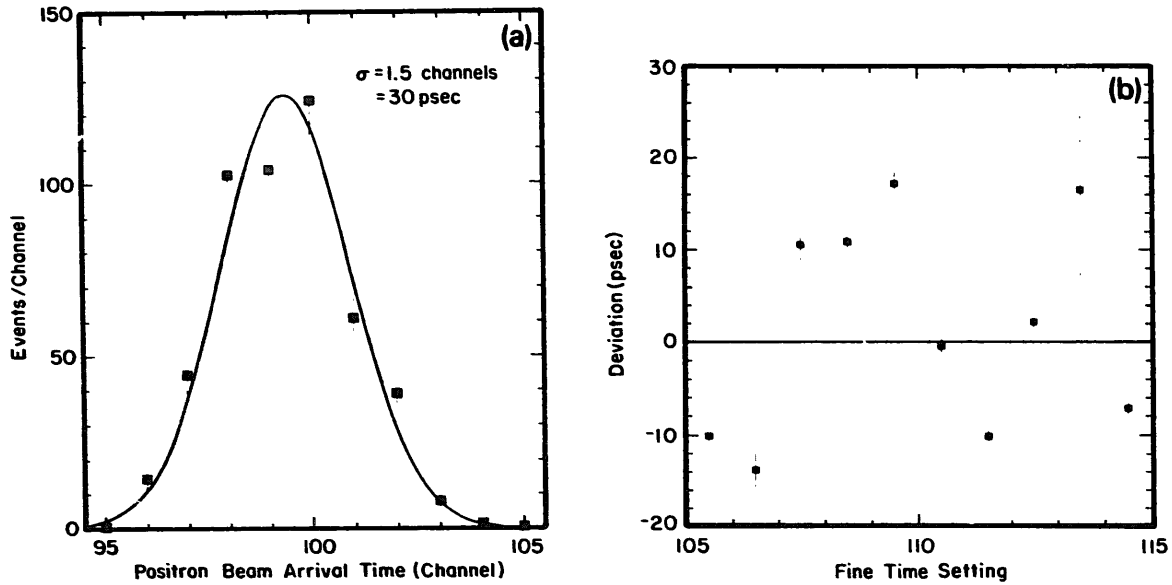


Fig. 58. (a) The positron beam arrival as timed by the time-of-flight system. The beam signal is from induced charge on a passive detector located 5 m from the interaction point. (b) Residual from a straight line fit vs programmed delay for a fine delay circuit used in CLEO II. The nominal difference between settings is 165 ps.

which would be necessary if coincidences between the central drift chamber and the time-of-flight were required in the L0 trigger or if CESR changes its mode of operation to use more than seven bunches of electron and positrons (see fig. 59).

The CsI crystal system is rather slow in generating trigger signals. Triggers relying solely on energy deposition in the crystals (eg.,  $e^+e^- \rightarrow \gamma\gamma$ ) will therefore satisfy the L0 trigger at a much later time than those that have time-of-flight or tracking information avail-

able at L0. Nonetheless, we wish to always examine the pulse height in the crystals at the same time with respect to the collision that produced the event. Therefore, if L0 was satisfied by time-of-flight and/or tracking, the sequencer sends extra clock pulses to the CsI digital pipeline and delays the closing of the CsI pulse height gate. If, on the other hand, the L0 trigger was due exclusively to crystal energy, no extra clocking or delay are generated.

One of the most important functions of the sequencer is to reset detector and trigger electronics and to re-enable the experiment after an event. There are three situations for executing the two-part reset sequence: initialization, such as at the beginning of data collection; resumption of data collection, usually after reading out the detector; re-enabling of the trigger system and detector after an unsuccessful search for a higher level trigger [39]. A schematic of the operation of this reset sequence is shown in fig. 60. The first signal in the sequence, ASRST, is generated asynchronously to collisions, immediately upon receipt of the request for the reset; this resets all the sequencer logic, clears the calibration controller, clears the CsI ADC buffers, restarts the CsI digital clocks (to clear the CsI trigger pipeline described above), reopens all the pulse height gates, and frees the drift chamber trigger logic to self-reset [40].

The second signal, SYRST, is synchronous with the beams crossing in the interaction region, being timed by the programmable coarse and fine delay circuits described above [36]. The minimum amount of time between ASRST and SYRST is set by the experi-

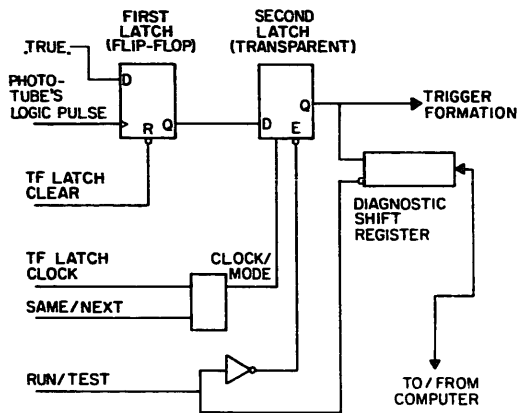


Fig. 59. Schematic of the time-of-flight trigger bit generation showing the double latch scheme which is effectively a two-slot pipeline. The first latch is set by the arrival of a signal from the time-of-flight data electronics. To move the information in the pipeline either i) the mode of operation must be "SAME" so that the second latch is transparent or ii) the "TF latch clock" must arrive before the "TF latch clear". A "TEST" mode of operation exists to load patterns via the computer.

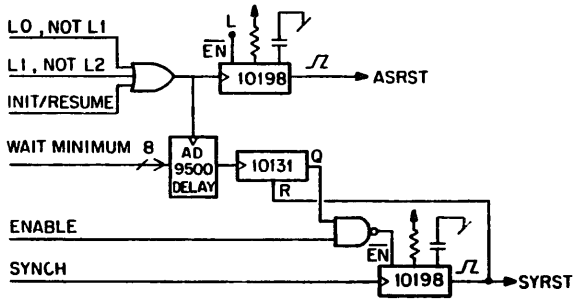


Fig. 60. Schematic of the reset sequence showing the generation of the asynchronous and synchronous pulses. The AD9500 affords 8 bits of programmable delay between generation of ASRST and the enabling of SYRST.

menter and is typically 800 ns. The functions of SYRST are clearing the trigger logic, enabling the L0 strobe and the detector timing gates, clearing the time-of-flight trigger logic, and enabling the calibration controller.

For SYRST to be asserted the ENABL input to the sequencer must be armed. This signal is logically low during the readout of the detector. After an event the ENABL line is not set logically high for approximately 12  $\mu$ s after ASRST, allowing the devices to properly clear their timing and charge capacitors before re-enabling data recording.

### 7.2. CLEO II trigger system

The CLEO II trigger system is described in a previous article in this journal [39]. Here only an overview of the system and details of changes and modifications will be given.

A trigger system with three tiers or levels has been developed. The flow of trigger logic is depicted in fig. 61. In the absence of triggers, the detector is active, with the wire chambers continuously collecting time

and pulse height information. If the data is not read out, the information decays away with approximately a 1.3  $\mu$ s time constant. The scintillator electronics is gated every beam crossing.

Level 0 (L0) is fast, simple, yet discriminatory. It receives inputs from the time-of-flight scintillators, from the vertex detector, and the CsI electromagnetic calorimeter, attempting to reduce the 2.7 MHz crossing frequency to a rate on the order of 20 kHz. The experimenter is able to define any number of sets of criteria for L0, all of which are logically OR'd.

Whenever any of the L0 criteria are met, all gates to the detector are disabled and a search for a set of the Level 1 (L1) trigger combinations requested by the experimenter is initiated. L1 receives inputs from the scintillators, from the vertex detector and central drift chamber, and from the electromagnetic calorimeter. The time required for these devices to all be "ready" for L1 interrogation is approximately 1.0  $\mu$ s, so an L0 rate of 20 kHz implies a minimum of 2% dead time. The goal of L1 is to reduce this rate to 25 Hz at present CESR luminosities. If no L1 criteria have been met, the trigger logic is reset and gating of the experiment resumes. Each set of L1 criteria has a specific set of L2 criteria which will be examined if those L1 criteria are met. The L1 triggers can be prescaled via 8-bit programmable scalers.

At present only the vertex detector and drift chamber contribute to L2. The readiness time for L2 is now 50  $\mu$ s, although implementation of new L2 schemes might increase this waiting period. Since the L1 rate is not envisioned to exceed 50 Hz, this wait for L2 results in only 0.25% dead time. As with L1, if no proper L2 criteria are met the system is reset and gating resumes.

Since submitting the article detailing this system [39], several significant changes have been made to the system:

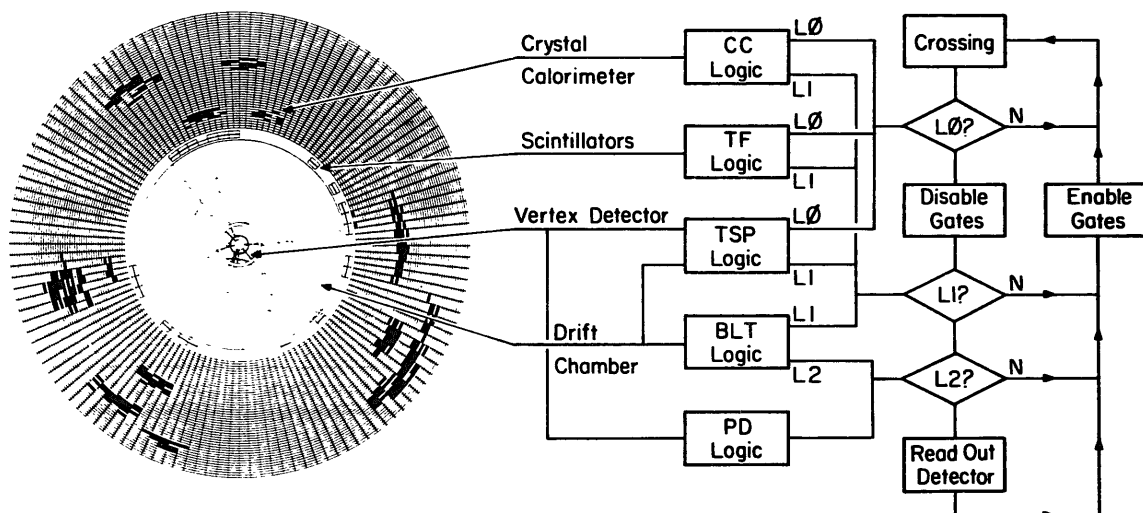


Fig. 61. Flow of the tiered trigger for CLEO II, showing the various detector elements used in each level of the decision process.

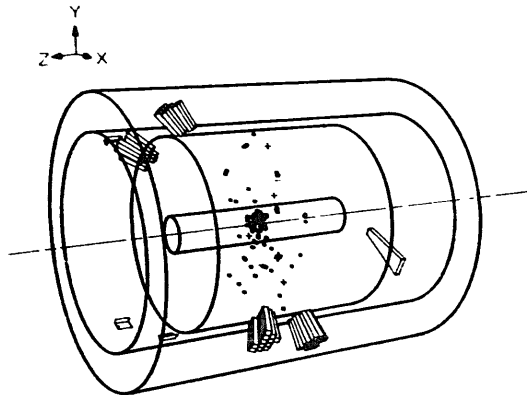


Fig. 62. An event in the CLEO II detector that was accepted only on the newly added two-photon trigger lines. This event is of the type  $\gamma\gamma \rightarrow f_2 \rightarrow \pi^0\pi^0$ .

i) Two-photon physics: In an attempt to increase our sensitivity to  $\gamma\gamma$  physics (i.e.,  $e^+e^- \rightarrow e^+e^-\gamma\gamma$ ), several new criteria have been added to the trigger specifications. The coincidence of an endcap time-of-flight scintillator with a vertex detector track has been added as an acceptable combination to have an L0 trigger; this has increased the L0 rate by roughly 25%. At L1 two new combinations appear. The first (designed to capture untagged, all-neutral events) demands non-adjacent high-threshold bits set in the CsI barrel calorimeter in conjunction with no charged tracks traversing the drift chamber. The second new L1 combination is designed to find single-tagged  $\gamma\gamma$  events; it requires an electron signature in the endcap time-of-flight and CsI endcap calorimeter, two non-adjacent low threshold bits in the CsI barrel calorimeter, and at most one short track in the drift chamber. There are no L2 requirements. In typical running conditions these  $\gamma\gamma$  specifications add 8% to the overall trigger rate. An example of an event which we accepted by virtue of having these new trigger requirements is shown in fig. 62.

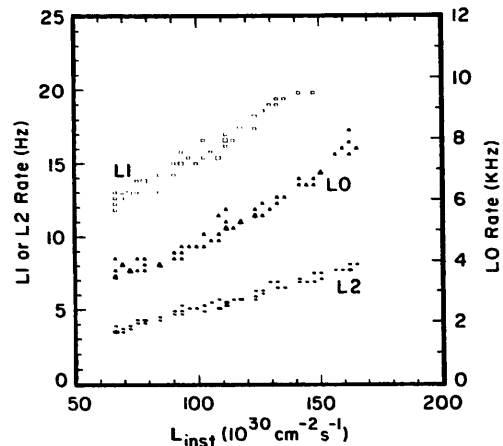


Fig. 63. Rates for the three trigger levels vs luminosity in a recent run. Note that the luminosities are the on-line data recording values and that the points for L0 use the right axis.

ii) Barrel time-of-flight inputs: Increases in CESR luminosity have forced us to use the AND of the two ends of the barrel time-of-flight scintillators as the basic trigger element instead of the OR of the two ends. Coupled with improved background conditions, this change has reduced the L0 rate by a factor of more than 5.

iii) L0 strobe time: The relative time of investigating the L0 trigger inputs with respect to the beams crossing has been increased to 405 ns. This has been done to improve the efficiency of the vertex detector in the L0 decision process. This change does, unfortunately, reduce the resolution of charge division in the vertex detector since the charge collected now has more time to equalize between the two ends of the chamber.

iv) Dead time induced by L0 triggers: By fine-tuning various delays, the number of crossings "lost" when a valid L0 combination fails to find a valid L1 combination has been reduced from 7 to 6. This makes the dead time associated with the lowest trigger level 0.22% per kHz. Given these changes, the actual rates for L0,

Table 7  
Readout crates in CLEO II

Device	Type	Number crates	Ready time [ms]	Sparsification
Outer drift chamber	Analog	20	7.2	T.AND.Q
Vertex detector	Analog	4	7.0	T.AND.Q
Precision tracker	Analog	1	4.6	T.AND.Q
Time-of-flight	Analog	1	2.4	T1.OR.T2.OR.Q
Muons	Analog	2	2.9	Q1.OR.Q2
Trigger	Digital	7	0.4	None
CAMAC	Digital	1	0.4	None
CsI calorimeter	Fastbus	1	8.0	SPARXL

L1, and L2 in a typical data run are shown in fig. 63 as a function of instantaneous luminosity.

7.3. CLEO II data acquisition system

Once the trigger system has decided that an event of interest has occurred, the data from the CLEO II detector must be read out to facilitate software tests of event quality (sometimes referred to as the "Level 3 trigger") and record the event for subsequent analysis. CLEO II has three distinct types of data systems:

- i) analog circuits developed by the CLEO II staff which store their timing or charge information on capacitors;
- ii) Fastbus electronics for the storage of information from the CsI calorimeter; and
- iii) digital information from the trigger system and various CAMAC modules.

The detector electronics is organized into "data crates" as indicated in table 7. With each crate is associated a microprogrammed controller which executes multiple instructions per clock cycle. The trigger system generates a signal which interrupts both the on-line VAX-3200 and the data crate controllers. The controllers for the analog devices have a fast ADC and a local memory for the storage of constants such as pedestals and time windows which allow us to suppress channels that have no useful information. This sparsification has a different algorithm for each of the various analog systems. In the tracking devices (central drift chamber, vertex detector, precision tracker) the data stream consists of a cell ID, a time, and a charge. For

this triplet of data to be kept the time must be within a specified window and the charge must be above a certain minimum. In the time-of-flight system the data stream has four entries: an address, two times, and a charge. For the quartet to be passed on, one of the three variables must be within a specified range. The muon system, which employs charge division, has triplets of data consisting of an address and two charges; this triplet is accepted if either of the two charges is above a specified minimum value.

Upon receiving the event interrupt from the trigger, all the "analog" crates begin digitization in parallel, with a conversion time of 3  $\mu$ s per channel; the maximum digitization time for a crate for each detector element is also shown in table 7. The sparsified data for each crate is stored locally on the controller in a buffer RAM awaiting readout to the VAX-3200. In principle once the data is digitized the front end electronics could be re-enabled. In practice the input electronics, particularly for the tracking chambers, is sensitive to the crate controller clocking the data from its local memory to the on-line VAX-3200 and all crates must be digitized and read out before the re-enabling is performed. The controllers in the crates handling digital functions (trigger and CAMAC) prepare the data for read back and load it into a local buffer RAM. As shown in table 7 the digital crates are ready quickly.

The CsI calorimeter analog data is transmitted to LeCroy Fastbus ADC cards which digitize the data in 750  $\mu$ s. The data are then transferred to a sparsifier; this transfer takes 6 ms. Sparsification of the CsI data takes less than 1 ms, leading to a total "ready time" for

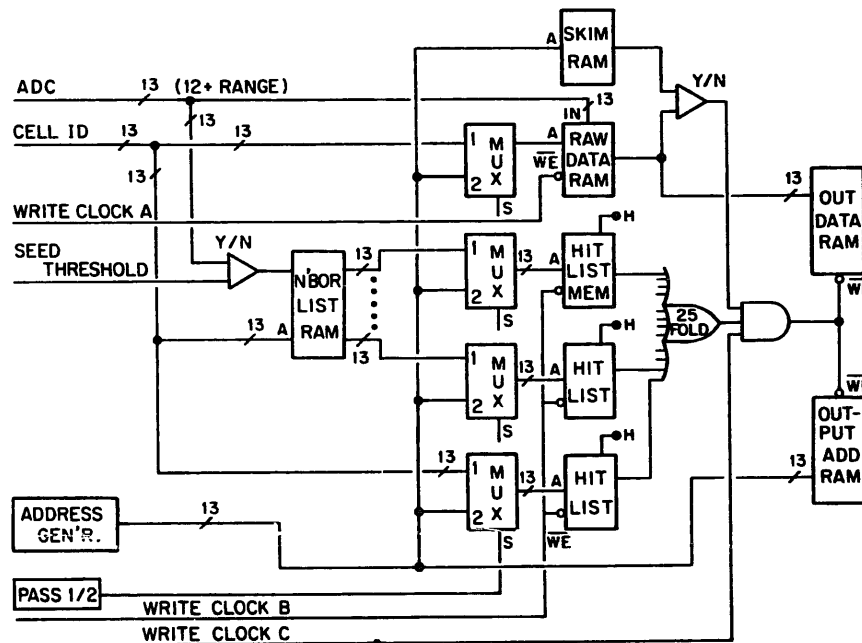


Fig. 64. Schematic showing the flow of sparsification of the CsI calorimeter data, as described in the text. On the first pass the hit list memories are filled. On the second pass the data from the hit list cells are compared to the thresholds stored in the skim ram.

the calorimeter of 8 ms (see table 7). To get proper resolution on 50 MeV photons, energies in CsI cells on the order of 1 MeV must be kept if they are associated with a shower centre. The noise level in a cell is typically 600 keV, thus making it difficult to simply sparsify based on a single threshold; either too many cells would be kept, defeating the purpose of sparsifying, or too many cells needed for good resolution would be tossed out. Therefore we need two-dimensional sparsification (to look at nearest neighbours and next-nearest neighbours of seed cells) and two passes of sparsification (since on the first pass we do not know if a particular cell is a neighbour to a seed).

This procedure has been designed into a hardware module called SPARXL; a schematic of SPARXL's operation is shown in fig. 64. The ADC information (13 bits of data) and cell address (also 13 bits) come from the FASTBUS electronics. After a trigger, every crystal's pulse height is digitized and the ADC data are read into the raw data RAM. On the first pass, the ADC value is compared with the seed threshold; if the cell qualifies as a seed, the addresses of its 24 neighbours (i.e., a  $5 \times 5$  array centred on the seed) are looked up in the neighbour list RAM. The 25 hit list RAMs are then loaded with a logical .TRUE. at these addresses (seed plus 24 neighbours). On the second pass, the address generator simultaneously presents the same 13 bit address to the 25 hit list RAMs, the raw data RAM, and a skim RAM. This last memory allows for each cell to have a different threshold to be kept as part of the shower. If any of the 25 hit list RAMs has its memory location set .TRUE. and the ADC value from the raw data RAM exceeds the skim threshold the address and data are put into the output RAMs. The timing of the write clocks, the switchover between passes, the cycling of addresses, and the event-by-event clearing are all handled by the microcode running in the SPARXL crate controller.

An on-line processor reads the data from the crates sequentially via a 16-bit bus (called YBUS) at a rate of 1.5 MBytes/s, and places the data from each event into one of 32 buffers located in a dual-ported memory. This FIFO buffer system consists of 1 MByte of memory in which we currently allocate 32 kBytes per event. It is read asynchronously by the on-line data-logging process, which formats the data into sequential ZEBRA [41] records and writes them to disk. The crates are addressed sequentially in the order that they nominally have data ready, as given in table 7 (time of flight first, CsI calorimeter last). The total readout takes about 12 ms, after which the experiment is re-enabled; hence the dead time incurred is 1.2%/Hz. This data bus is not a single cable since that cable would be too long (requiring several repeaters) and would make finding problem connections too difficult. Instead a fan-out for the bus has been implemented 33 m from

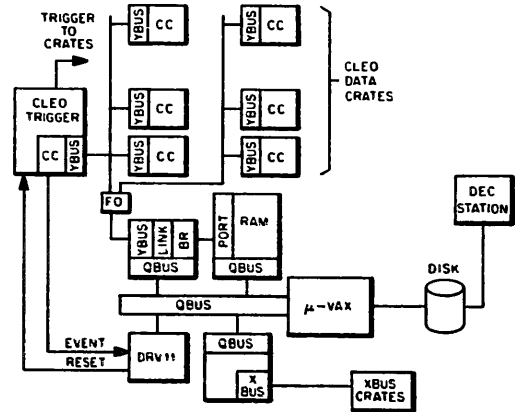


Fig. 65. The CLEO II bus scheme. The blocks labelled "CC" are crate controllers while "FO" is a fan-out for the YBUS.

the on-line computer which has six branches (see fig. 65); therefore each branch has only a small number of crates attached to it and all the necessary amplification done in one location [42].

As indicated in fig. 65 the VAX-3200 does not communicate with the YBUS directly but rather via a QBUS/YBUS interface. The data that has been read out of the crates is deposited in a dual port buffer memory to minimize dead time to the experiment. Also attached to the QBUS is another internal bus, denoted XBUS, which is used for setting high voltages, setting calibration parameters, and many other hardware functions.

## 8. Plans for the next few years

### 8.1. Upgrading the data acquisition system

The existing data acquisition system of the CLEO detector allows read out of the detector at a maximum rate of 10 Hz. This is limited by the on-line computer reading the event data from an intermediate memory file which can contain up to 32 events. Approximately 100 ms are required to read out an event from the buffer. At a trigger rate of 10 Hz, the detector live time is approximately 88%. To put these numbers into context, one should keep in mind the hadronic cross section at the  $T(4S)$  is 3.5 nb and CLEO typically begins data recording after beam filling with a luminosity of  $1.5 \times 10^{32}/\text{cm}^2/\text{s}$ . Hence, the hadronic event rate at the beginning of a run at the  $T(4S)$  is 0.52 Hz. However, we read out many events in addition to those from the hadronic cross section. There is much interest in studying  $\tau$  lepton decay and two photon physics. The trigger tagging of  $e^+e^- \rightarrow \tau^+\tau^-$  and  $e^+e^- \rightarrow e^+e^-\gamma\gamma \rightarrow e^+e^-$  (hadrons) events requires much looser trigger criteria because of the low multiplicity of these final states. Furthermore, one uses Bhabha and

muon pair events to help calibrate the detector. However, these do not produce a major enhancement in our data acquisition needs since we can prescale them to reduce the rate at which we are reading in the "calibration events." (We have been prescaling the endcap Bhabha trigger by a factor of 30.) Currently, our total trigger rate when recording data on the T(4S) is typically 6 Hz at the beginning of the run, and the detector live time is 90%. Approximately 12% of these triggers are multi-pronged hadronic events with a visible energy greater than 3.5 GeV, and 25% are calibration events. Therefore, the existing data acquisition system is adequate.

However, we often want to search for new phenomena, which can only be done by running the detector with a looser trigger and not prescaling. Furthermore, we expect a luminosity increase of at least a factor two from CESR within the next few years. To handle this increase in luminosity it is critical to upgrade the rate at which we can acquire data. A new data acquisition system, DAQ90, has been developed. The crate readout system will be changed to reduce the detector readout dead time from 12 to 2 ms per event. The goal of the new system is to readout digitized events at rates up to 50 Hz and to perform further rejection in software. This is accomplished by introducing point-to-point links between each crate and a central VME-based data sparsification and event formatting system. As each data item is digitized at the crate it is sent to its own dualported memory at the central system. Four Motorola 68040 processors empty the dualported memories over VSB (VME sub-system bus) and sparsify the data. A single 68040 then assembles the event fragments into an event record. This is then distributed to one of a set of DECstation 5000 computers where it is processed with code similar to our existing computer program, which allows event rejection and classification. We expect to enable more sophisticated event selection prior to transferring the data into the on-line computer, which will provide an order of magnitude increase in our data acquisition capacity. We are presently (June 1991) installing the DAQ90 system and will start using it after the summer shutdown.

### 8.2. A future upgrade of the CLEO vertex detector

In order to significantly improve the vertexing capability of the CLEO detector, it is necessary to further reduce the radius of the beam pipe, which is currently 3.5 cm, compared to 5.5 cm in the CLEO I detector. The reduction in beam pipe radius led to an increase in background which must be minimized before the beam pipe can be further reduced. Investigations indicated that the source of the background was, in roughly equal measure, scattering of beam particles off residual gas upstream of the interaction region, and synchrotron radiation (SR). The source of the SR hitting

the beam pipe at the interaction region was found to be reflections off of the wall of the vacuum chamber in the bending magnet region of the machine upstream of the interaction region. It was proposed that moving the vacuum chamber in this region by 2 cm would result in the SR that was hitting the IR being masked by an upstream flange. Subsequently, the vacuum chamber was moved, and the SR evident in the CLEO detector was reduced. We are now engaged in a program to understand and reduce the remaining beam gas background.

There is a research-development effort in both silicon and gas chamber detector which might be used in a future vertex detector system. A beam test was performed at FNAL of a double sided silicon telescope [43].  $1 \times 1 \text{ cm}^2$  prototype double sided detectors were manufactured by Hamamatsu, and used with microplex readout electronics based on the design used for the ALEPH detector at LEP. During the beam test the detectors were successfully operated and read out, and the data indicated spatial resolutions of 20  $\mu\text{m}$ , rms. There is not yet a detailed design for a smaller beam pipe and a new vertex detector system but we anticipate being ready to install a 2 cm radius pipe with double sided silicon strip detectors by Spring 1994.

### 8.3. The physics program

Since the turn on in October 1989, we have accumulated 150  $\text{pb}^{-1}$  on the T(3S), 15  $\text{pb}^{-1}$  on the T(1S), 530  $\text{pb}^{-1}$  on the T(4S), 230  $\text{pb}^{-1}$  on the continuum 26 MeV below the T(4S), and 65  $\text{pb}^{-1}$  above the T(4S). This data is being used to study T spectroscopy, charm and bottom decay,  $\tau$  lepton decay, and quark fragmentation. Although this is a significant data sample, to answer the many questions related to these subjects we plan to record an additional 1  $\text{fb}^{-1}$  on the T(4S), 0.5  $\text{fb}^{-1}$  below the T(4S), and 0.1  $\text{fb}^{-1}$  on the T(1S) with in the next two years. This will allow significant improvement in tabulation of the B meson branching fractions and better measurement of mixing and the CKM matrix elements. It will be interesting to see how much we learn with this new detector.

### Acknowledgements

Design, construction and assembly of the CLEO II detector took place over a seven year time span, 1983 to 1989. During this time, we received enormous help and advice from a wide array of technical professionals. We wish to thank the experimental support staffs at each of the Universities who undertook major responsibilities for building CLEO II. Design and construction of the calorimeter electronics was carried out through a coordinated effort between Cornell and Ohio

State University. The SUM-circuit electronic cards and the associated crates were designed, constructed and tested at OSU. We thank C. Rush of OSU who was responsible for this work.

The Harvard collaborators built the barrel time-of-flight counters and the associated readout electronics. The collaborators from SUNY Albany built the endcap time-of-flight counters. J. Blandino and J. McElaney of Harvard did the detailed barrel counter design work and supervised the construction, assembly, testing, and installing of the barrel time-of-flight counters in the CLEO II detector. J. Oliver of Harvard designed and built the high voltage supplies and the readout electronics for the entire time-of-flight system.

The Syracuse University collaborators designed and built the muon identification system. L. Buda and J. Ennulat were responsible for the construction, assembly and testing of the 24 barrel + 8 endcap three-layer units at Syracuse University. Z. Sobolewski provided the high voltage supply system and made the necessary modifications to the old CLEO  $dE/dx$  electronic circuits so that the "streamer counters" could operate in proportional mode. He also came to the Cornell laboratory and helped with the installation and testing of the system.

The coordination of the readout electronics of the entire CLEO II detector was carried out mainly by collaboration physicists at Cornell. However, much of the detailed design and construction was performed by J. Dobbins of Cornell. He provided the preamplifiers for the endcap time-of-flight counters, the preamplifiers and readout electronics for the tracking chambers, and much good advice for the calorimeter readout.

We thank Prof. B.D. McDaniel, former director of the Cornell Laboratory of Nuclear Physics, for his strong support for the design, development, and construction of the CLEO II detector. He also participated in the design and construction of the mechanical support of the CsI calorimeter. A major share of the cost of the intermediate drift chamber, (the VD), and the time-of-flight system was provided by the Department of Energy. The National Science Foundation provided the funds for building the rest of the CLEO II detector. We also acknowledge the financial support of the National Science Foundation and the Department of Energy for the institutional members of the CLEO Collaboration.

## References

[1] The  $T$  family of resonances were first observed in proton nucleus collisions at Fermilab; S.W. Herb, et al. Phys.

- Rev. Lett. 39(1977)252. The Fermilab result was confirmed at DESY, where the production cross section for  $e^+e^- \rightarrow T(1S)$  provided arguments for postulating the  $T$  family is a bound  $b\bar{b}$  quark system. Observation of the  $T(1S)$  was reported by Ch. Berger et al., Phys. Lett. 76B(1978)243 and C.W. Darden et al., Phys. Lett. 76B(1978)246. Observation of the  $T(2S)$  was reported by J.K. Bienlein et al., Phys. Lett. 78B(1978)360, and C.W. Darden et al., Phys. Lett. 80B(1979)419.
- [2] Observation of the  $T(1S)$ ,  $T(2S)$ , and  $T(3S)$  were reported by: D. Andrews et al., Phys. Rev. Lett. 44(1980)1108 and T. Bohringer et al., Phys. Rev. Lett. 44(1980)1111. Discovery of the  $T(4S)$  was published by D. Andrews et al., Phys. Rev. Lett. 45(1980)219; and G. Finocchiaro et al., Phys. Rev. Lett. 45(1980)222.
- [3] S. Behrends et al., Phys. Rev. Lett. 50(1983)881.
- [4] G.L. Kane and M.E. Peskin, Nucl. Phys. B195(1982)29; H. Georgi and M. Machacek, Phys. Rev. Lett. 43(1979)1639; E. Derman, Phys. Rev. D19(1979)317; H. Georgi and S.L. Glashow, Nucl. Phys. B167(1980)173; and R.N. Mohapatra, Phys. Lett. 82B(1979)101.
- [5] E. Nordberg and A. Silverman, The CLEO Detector, Laboratory of Nuclear Studies, CBX 79-6 (1979) (unpublished); and D. Andrews et al., Phys. Rev. Lett. 44(1980)1108.
- [6] D. Andrews et al., Nucl. Instr. and Meth. 211(1983)47.
- [7] D.G. Cassel et al., Nucl. Instr. and Meth. A252(1986)325.
- [8] CLEO II Updated Proposal for Improvements to the CLEO Detector for the Study of  $e^+e^-$  Interactions at CESR, CLEO Collaboration, CLNS-85/634, January 1985. (supersedes CLNS 84/609).
- [9] D.M. Coffman et al., IEEE Trans. Nucl. Sci. NS-37(1990)1172.
- [10] The following construction materials are trademarked: Ultem, the General Electric Corporation; Delrin, the Dupont Corporation; Mylar is a thin strong polyester film trademarked by Dupont; Rohacell, a polymethacrylimide rigid foam, Cyro Industries; Lexan, a polycarbonate, General Electric Corporation.
- [11] M. Frautschi et al., Nucl. Instr. and Meth. A307(1991)52.
- [12] J.A. Kadyk, Nucl. Instr. and Meth. A300(1991)436.
- [13] R. Talman, Nucl. Instr. and Meth. 159(1979)189.
- [14] R.T. Giles, F.M. Pipkin and J.P. Wolinski, Nucl. Instr. and Meth. A252(1986)41.
- [15] A. Bean, et al., IEEE Trans. Nucl. Sci. NS-33(1986)411.
- [16] E. Blucher, et al., Nucl. Instr. and Meth. A249(1986)201.
- [17] Z. Bian, J. Dobbins, and N. Mistry, Nucl. Instr. and Meth. A239(1985)518.
- [18] C. Bebek, Nucl. Instr. and Meth. A265(1988)258.
- [19] B.C. Grabmaier, IEEE Trans. Nucl. Sci. NS-31(1984)372.
- [20] E.D. Bloom and C.W. Peck, Ann. Rev. Nucl. Part. Sci. 33(1983)143; D. Antreasyan et al., Phys. Rev. D36(1987)2633; and D.A. Williams et al., Phys. Rev. D38(1988)1365.
- [21] J. Lee-Franzini, Nucl. Instr. and Meth. A263(1988)35; and P.M. Tuts, Nucl. Instr. and Meth. A265(1988)243.
- [22] L3 Collaboration, B. Adeva et al., Nucl. Instr. and Meth. A289(1990)35.

- [23] The gap at  $\theta = 90^\circ$  does point directly at the nominal collision vertex.
- [24] The bulk of the thallium-doped CsI crystals for CLEO-II were manufactured by Horiba, Ltd, Kyoto, Japan, and BDH Chemicals, Ltd., (now Merck Ltd.) Poole, England. About 100 endcap crystals were also supplied by each of Bicon Corp., Newbury, Ohio, and Harshaw/Filtrol Corp., Solon, Ohio.
- [25] The value of  $N$  is in general not an integer: the energy corresponding to the fractional part of  $N$  is taken as that fraction of the next highest crystal's energy. For example, if  $N = 5.5$ , the cluster energy is taken as the sum of the highest five crystals plus half of the sixth. This avoids discrete jumps in shower energies which would occur if  $N$  were required to be integral.
- [26] The CERN detector-modeling software package known as GEANT forms the basis of the CLEO-II Monte Carlo simulation.
- [27] Inclusive X(2P) Production in  $\Upsilon(3S)$  Decay. R. Morrison, et al., Phys. Rev. Lett. 67(1991)1696.
- [28] Angular resolution in the barrel crystals varies with the position within a block; the resolution is much better near a block boundary than near the center because more energy is shared with other crystals. For example, near the center (edge) of a block, the azimuthal resolution is 3.8 mrad (2.1 mrad) at 5 GeV and 14 mrad (5.7 mrad) at 100 MeV. The values quoted in the text and figure represent resolutions averaged over all angles.
- [29] M. Narain et al., Phys. Rev. Lett. 66(1991)3113.
- [30] R. Nernst et al., Phys. Rev. Lett. 54(1985)2195.
- [31] D. Bortoletto et al., this issue, Nucl. Instr. and Meth. A320(1991)114.
- [32] This quantity is called "nuclear interaction length" in the Review of Particle Data of the Particle Data Group.
- [33] E. Iarocci, Nucl. Instr. and Meth. 217(1983)30.
- [34] From Costruzioni Meccaniche Bindi, San Giustino, PG, Italy.
- [35] See Appendix A in ref. [31].
- [36] The signals are the start and stop of the time-of-flight gate, the start and stop of the L0 strobe, the hardware reset, the strobe used to clock the readout bits in the CsI crystals trigger electronics pipeline, and two signals used in calibrations.
- [37] Diagrams for this and other components are available from the LNS Drafting Room, Newman Laboratory, Cornell University, Ithaca, NY 14853, USA. The coarse timing circuit is drawing 6044-33 and the 72 MHz phase-shifter circuit is on drawings 6044-99 (TTL outputs) and 6044-115 (ECL outputs).
- [38] R.E. Meller, IEEE Trans. Nucl. Sci. NS-26(1979)4152. The data shown in fig. 54a is averaged over the seven bunches of positrons in CESR for one particular setting of the fine delay. Other settings of this delay produce distributions that have several such narrow peaks, with means between peaks varying up to 100 ps and each peak corresponding to a particular subset of the seven bunches. Since we know with which bunch an event is associated, we can correct for this effect in software, if necessary.
- [39] C. Bebek, et al., Nucl. Instr. and Meth. A302(1991)261.
- [40] The latches which form the trigger inputs from the tracking chambers are reset by an RC network which is enabled by this asynchronous reset signal. The time constant for this network to generate a reset is approximately 500 ns.
- [41] R. Brun and J. Zoll, CERNQ-100, 1987. In order to minimize time spent formatting, CERN ZEBRA code was not used; rather, code based on ZEBRA format was written for the CLEO-II data structure.
- [42] The circuit design for this fan-out is available, drawing 6052-602. See ref. [37].
- [43] J.P. Alexander et al., Conference record of the 1990 IEEE Nucl. Sci. Symp., Oct. 1990 (CLNS 90-1034) Vol. 1, p. 766.